



NTNU – Trondheim
Norwegian University of
Science and Technology

3D Numerical modeling of flow over an artificial gravel bed

Vincenzo Sessa

Master's Thesis

Submission date: September 2014

Supervisor: Nils Rüther, IVM

Co-supervisor: Carlo Gualtieri, University of Naples Federico II

Norwegian University of Science and Technology
Department of Hydraulic and Environmental Engineering



NTNU – Trondheim
Norwegian University of
Science and Technology

3D Numerical modeling of flow over an artificial gravel bed

Vincenzo Sessa

Civil and Environmental Engineering

Submission date: September 2014

Supervisor: Nils Rüther, IVM

Norwegian University of Science and Technology

Department of Hydraulic and Environmental Engineering

Table of Contents

0	ABSTRACT	7
1	INTRODUCTION	8
1.1	Background.....	8
1.2	Focus and limitations.....	8
1.3	Outline	8
2	NUMERICAL MODELING OF TURBULENT FLOW	9
2.1	Turbulent flow	9
2.2	Navier-Stokes equations	11
2.3	Reynolds-Averaged Navier-Stokes equations	13
2.4	Turbulence models	13
2.5	Gravel bed evolution	14
3	CFD MODEL IN STAR-CCM+	15
3.1	Introduction	15
3.2	Pre-processing	16
3.3	Mesh models.....	17
3.3.1	Surface mesh.....	19
3.3.2	Volume mesh.....	19
3.4	Physics models	19
3.4.1	Multiphase mixture material.....	20
3.4.2	Fundamental equations	20
3.4.3	Momentum equation.....	20
3.4.4	Energy equation.....	21
3.5	Boundary conditions.....	22
3.5.1	Wall laws	22
3.6	Modeling techniques.....	23
3.6.1	Volume of fluid (VOF).....	23
3.6.2	Volume fraction.....	24
3.7	Turbulence models in STAR-CCM+.....	25
3.7.1	Reynolds-Average Navier-Stokes	25
3.7.2	Turbulent-viscosity models	26
3.7.3	Reynolds-stress models	26
3.8	Solver.....	26
3.8.1	Space.....	26
3.8.2	Time.....	27

3.9	Post-processing.....	27
4	PAST EXPERIMENTAL WORKS	28
4.1	Artificial streambed	28
4.1.1	Preparation.....	28
4.1.2	Molding	29
4.1.3	Casting.....	29
4.1.4	Detaching and finishing.....	29
4.1.5	Coloring.....	30
4.2	PIV measurements.....	30
4.3	Experimental setup	30
4.3.1	Experimental procedure.....	31
4.3.2	Treatment of vectors below roughness tops	31
4.4	Discussion.....	32
5	NUMERICAL MODEL SETUP	33
5.1	Pre-processing	33
5.2	Mesh	34
5.2.1	Trimmed Mesher	34
5.2.2	Grid.....	35
5.3	Physics models	38
5.3.1	Eulerian multiphase	38
5.4	Flow conditions	39
5.4.1	Initial conditions	39
5.4.2	Boundary conditions.....	39
5.4.2.1	<i>Velocity Inlet</i>	39
5.4.2.2	<i>Pressure Outlet</i>	40
5.4.2.3	<i>Wall Boundaries</i>	41
5.5	Hydraulic conditions.....	41
5.6	Solvers	42
5.7	Stopping criteria	43
5.8	Post-processing.....	43
6	COMPARISON OF THE RESULTS.....	45
6.1	Preliminary work	45
6.1.1	Area of analysis	45
6.1.2	Location of zero point.....	46
6.1.3	Double averaged velocity profile	46

6.2	Stopping criteria	47
6.2.1	Supercomputer.....	47
6.2.2	Mass flow	47
6.2.3	Residuals.....	48
6.2.4	Reynolds and Froude numbers	49
6.3	Water level.....	50
6.4	Pressure.....	51
6.5	Wall shear stress	54
6.6	Velocity scenes	56
6.6.1	Scalar velocity scenes	56
6.6.2	Vector velocity scenes	57
6.7	Mesh comparison.....	58
6.8	Turbulent models in comparison	60
6.9	Experimental data comparison	61
6.9.1	6 l/s water discharge	61
6.9.2	21 l/s water discharge	62
6.9.3	42 l/s water discharge	62
6.9.4	63 l/s water discharge	63
6.9.5	90 l/s water discharge	64
7	DISCUSSION.....	66
8	CONCLUSION	66
9	BIBLIOGRAPHY	67

FIGURES

Figure 1: Natural turbulence evidence	9
Figure 2: Reynolds experiment	11
Figure 3: Reynolds averaging	12
Figure 4: Process of discretization	16
Figure 5: Different mesh shapes.....	17
Figure 6: Structured grid	18
Figure 7: Unstructured grid.....	18
Figure 8: Mesh process	19
Figure 9: Volume of fluid algorithm	24
Figure 10: Turbulence models.....	25
Figure 11: Grain size	28
Figure 12: Preparation.....	28
Figure 13: Molding.....	29
Figure 14: Detaching.....	29
Figure 15: Casting	29
Figure 16: Result	29
Figure 17: Experimental setup	30
Figure 18: Experimental data	32
Figure 19: Geometry model	33
Figure 20: Mesh accuracy	35
Figure 21: 5 mm longitudinal mesh	36
Figure 22: 5 mm transversal mesh	36
Figure 23: 3 mm longitudinal mesh	37
Figure 24: 3 mm transversal mesh	37
Figure 25: Area of analysis	45
Figure 26: Location of zero point.....	46
Figure 27: Velocity on longitudinal grid.....	46
Figure 28: Vilje supercomputer.....	47
Figure 29: Mass flow balance	47
Figure 30: Residuals plot.....	48
Figure 31: 3D geometry model	50
Figure 32: Volume fraction of water at outlet.....	50
Figure 33: Water level.....	51
Figure 34: Pressure values for 6 l/s	51
Figure 35: Pressure values for 21 l/s	52
Figure 36: Pressure values for 42 l/s	52
Figure 37: Pressure values for 63 l/s	53
Figure 38: Pressure values for 90 l/s	53
Figure 39: Wall shear stress for 6 l/s.....	54
Figure 40: Wall shear stress for 21 l/s.....	54
Figure 41: Wall shear stress for 42 l/s.....	55
Figure 42: Wall shear stress for 63 l/s.....	55
Figure 43: Wall shear stress for 90 l/s.....	55
Figure 44: Longitudinal velocity magnitude	56
Figure 45: Transversal velocity magnitude	56

Figure 46: Velocity on longitudinal grid.....	57
Figure 47: Velocity on transversal grid.....	57
Figure 48: Vector velocity.....	57
Figure 49: Vector velocity on VOF.....	58
Figure 50: Mesh comparison for 42 l/s	58
Figure 51: Mesh comparison for 90 l/s	59
Figure 52: k-ε model (21 l/s).....	60
Figure 53: Spalart-Allmaras model (21 l/s).....	60
Figure 54: Dimensional velocity profile for 6 l/s	61
Figure 55: Non-dimensional velocity profile for 6 l/s.....	61
Figure 56: Dimensional velocity profile for 21 l/s	62
Figure 57: Dimensional velocity profile for 42 l/s	62
Figure 58: Non-dimensional velocity profile for 42 l/s.....	63
Figure 59: Dimensional velocity profile for 63 l/s	63
Figure 60: Non-dimensional velocity profile for 63 l/s.....	64
Figure 61: Dimensional velocity profile for 90 l/s	64
Figure 62: Non-dimensional velocity profile for 90 l/s.....	65

TABLES

Table 1: PIV measurements	31
Table 2: Repair tools	33
Table 3: Mesh procedure.....	34
Table 4: 5 mm mesh size.....	35
Table 5: 3 mm mesh size.....	35
Table 6: Physics models	38
Table 7: Initial conditions	39
Table 8: Functions at inlet.....	40
Table 9: Function at outlet	40
Table 10: Hydraulic conditions	41
Table 11: Solvers.....	42
Table 12: Stopping criteria.....	43
Table 13: Scalar/vector scenes and plot	44
Table 14: Reynolds and Froude numbers.....	49

0 ABSTRACT

The understanding of flow structures over static armor layers is essential for the development of modern sediment transport models, including functions for the influence of particle hiding and exposure. Coherent turbulent flow structures affect the incipient motion of single particles in a way that is still difficult to estimate. Furthermore, they can cause suspension of fine sediments that deposit elsewhere. With increasing computational power it has become more and more popular to use commercial computational fluid dynamic (CFD) codes in the field of hydraulic engineering. These models must be tested and verified on data from physical model studies, before they are used for general-purpose studies. The goal of the present study is therefore, to look into the possibility to use the commercial CFD code STAR-CCM+ to simulate the flow over an artificial gravel bed. The data taken to compare the results with are from a physical model test conducted by Spiller et al. (2013). PIV measurements were taken in a laboratory flume. This flume has been modeled within STAR-CCM+ in order to see whether it can reproduce the general flow characteristics.

The thesis shall cover, but not necessarily be limited to the following main questions:

- Generation of grid in STAR-CCM+;
- Generation of input files for STAR-CCM+;
- Compute the water flow for the physical model test describer in Spiller et al. (2013);
- Comparison of the numerical results to the results of the physical models;
- Preparation of figures which indicate the differences;
- Assessment of uncertainties in STAR-CCM+ by varying algorithms, coefficients and other input data.

The thesis shall present figures of grid, velocities, velocity vectors, TKE, bed shear stress and water levels as well as all other necessary plots to compare with the physical model data. The conclusion shall contain a personal opinion on the applicability of 3D model for assessing complex turbulent flow over rough bed. It should also point out the uncertainties in the model, effect of inaccurate input data and give recommendations for future work using STAR-CCM+.

1 INTRODUCTION

1.1 Background

Open-channel made up of simple geometry and free of obstructions are desirable for efficient water conveyance. Nowadays, roughness elements, such as gravels, are commonly deployed into artificial open-channels to stabilize the channel sectional shapes and to maintain the ecological balance there. Consequently, the hydrodynamic behavior of flows in these channels is significantly affected. The determination of the velocity and turbulence intensity profiles, as well as the hydraulic resistance, is of practical importance in the engineering design of these channels. One purpose of this study is to quantify the gravel roughness effects on flows and mixings using both experimental and numerical methods.

1.2 Focus and limitations

Focus of the work is on velocity profiles and turbulent characteristics in a fully rough, uniform channel flow over an artificial gravel bed. Due to bed topography small scale heterogeneity, the flow is not uniform locally in the near-bed region and a double averaging methodology is applied. The modeling work done in this thesis is based on the available 3D surfaces and refines them into steady flow models in STAR-CCM+. Particular attention has been on grid generation procedures, as this turned out to be a major factor in achieving good results. For the physical setup the thesis is based on solving the RANS equations using a realizable k - ϵ model in STAR-CCM+. As the author had no prior experience with STAR-CCM+ before starting work on this thesis, part of the work has been to get familiarized with the software. In particular a lot of effort has gone in creating a surface mesh in Stereolithography (STL) before importing the geometry in STAR-CCM+. As such, the quality of the surface data was usually not good and some additional work was required before the geometry was usable. Afterwards the critical part of this thesis has been the comparison between the modeling results and the data coming from a physical model test conducted by Spiller et al. (2013)

1.3 Outline

Chapter 2 describes the most relevant basic theory on CFD and Turbulent flow. Chapter 3 describes the CFD package STAR-CCM+ and explains how theory is implemented in the model. Chapter 4 is a brief description of the physical model test by Spiller et al. (2013) and in which way it was carried on. Chapter 5 focuses on the modeling process, on the boundary conditions as well as the hydraulic characteristics of the flow field modeled within STAR-CCM+. The comparison between the achieved results and the experimental data are presented in Chapter 6 in form of plots and figures. The author's conclusion, the uncertainties of the model as well as personal recommendations for future work using STAR-CCM+ can be in Chapter 7.

2 NUMERICAL MODELING OF TURBULENT FLOW

Nowadays most CFD simulations are carried out with traditional RANS (Reynolds-Averaged Navier-Stokes) equations. In RANS, the flow variables are split into one time-averaged (mean) part and one turbulent part. The latter is modeled with a turbulence model such as $k-\epsilon$ or Reynolds Stress Model. For many flows it is not appropriate to use RANS, since the turbulent part can be very large and of the same order as the mean. Examples are unsteady flow in general, wake flows or flows with large separation. For this type of flows, it is more appropriate to use Large Eddy Simulation (LES), which offers a solution of the continuity and Navier-Stokes equation on a “coarse grid” with some modeling while Direct Numerical Simulation (DNS) for simple geometries and low Reynolds numbers, without modeling. In order to extend LES to high Reynolds number flows, new methods have recently been developed. These are called DES (Detached Eddy Simulation), URANS (Unsteady RANS), PANS (Partially Averaged Navier-Stokes) or Hybrid LES-RANS. They are all unsteady methods and they are a mixture of LES and RANS. In LES, DES, URANS and Hybrid LES-RANS the large scale part of the turbulence is solved for by the discretized equations whereas the small-scale turbulence is modeled. The definition of “large-scale” varies in the different methods. Furthermore, the limit between “large-scale” and “small-scale” is often not well defined. Since turbulence is three-dimensional and unsteady, it means that in all the methods the simulations must always be carried out as 3D, unsteady simulations.

2.1 Turbulent flow

Turbulent flows are common in nature and have an important role in several geophysical processes related to a variety of phenomena such as river morphology, landscape modeling, atmospheric dynamics and ocean currents. Turbulence appears every day in almost every day situation, whether it be smoke from a cigarette, water in a river or waterfall, the flow in boat wakes and around aircraft wing tips.



Figure 1: Natural turbulence evidence

The main characteristics of turbulence flow are:

- ✓ Three dimensional vorticity fluctuations: turbulence is rotational and three dimensional and characterized by high levels of fluctuating vorticity. The random vorticity fluctuations that characterizes turbulence could not maintain themselves if the velocity fluctuations were two dimensional. Flows that are substantially two dimensional are not turbulence themselves, even though their characteristics may be influenced strongly by small-scale turbulence, which interacts with the large-scale flow. In summary, turbulent flows always exhibit high levels of fluctuating vorticity;
- ✓ Dissipation: viscous shear stresses perform deformation work which increases the internal energy of the turbulence. Turbulence needs a continuous supply of energy to make up for these viscous losses. If no energy is supplied, turbulence decays rapidly;
- ✓ Continuum: turbulence is a continuum phenomenon governed by the equations of fluid mechanics.

Turbulence flow is characterized by the efficient dispersion and mixing of vorticity, heat and contaminants.

In flows over solid bodies such as airplane wings or turbine blades, or in confined flows through ducts and pipelines, turbulence is responsible for increased drag and heat transfer.

Turbulence is therefore a subject of great engineering interest.

A central role in determining the state of fluid motion is played by the Reynolds number.

In general, a given flow undergoes a succession of instabilities with increasing Reynolds number and, at some point, turbulence appears more or less abruptly. It has long been thought that the origin of turbulence can be understood by sequentially examining the instabilities. This sequence depends on the particular flow and, in many circumstances, is sensitive to a number of details. However, it is very difficult to give a precise definition of turbulence; all one can do is to list some of the characteristics of turbulent flows:

- ✓ Irregularity or randomness: this makes a deterministic approach to turbulence problems impossible;
- ✓ Diffusivity: it causes rapid mixing and increased rates of momentum, heat and mass transfer. The diffusivity of turbulence is the single most important feature as far as applications are concerned;
- ✓ Large Reynolds number: the possibility that turbulence may occur is generally measured by the flow Reynolds number $Re = \frac{\rho LU}{\mu}$

Where ρ is the fluid density and μ is the dynamic viscosity of the fluid.

The parameters L and U are a characteristic length and speed for the flow. The important point to remember is that Re is meant to measure the relative importance of fluid inertia to viscous forces. When viscous forces are negligible, the Reynolds number is large.

A good choice for L and U is usually one that characterizes the region showing the strongest shear flow, that is, where viscous forces would be expected to have the most influence. For sure, a Reynolds number well above 1000 is probably turbulent while a Reynolds number below 100 is not. The actual value of a critical Reynolds number that separates laminar and turbulent flow can vary widely depending on the nature of the surfaces bounding the flow and the magnitude of perturbations in the flow.

The distinction between laminar and turbulent flow is readily apparent in a simple experiment first conducted by the English engineer Osborne Reynolds in 1883.

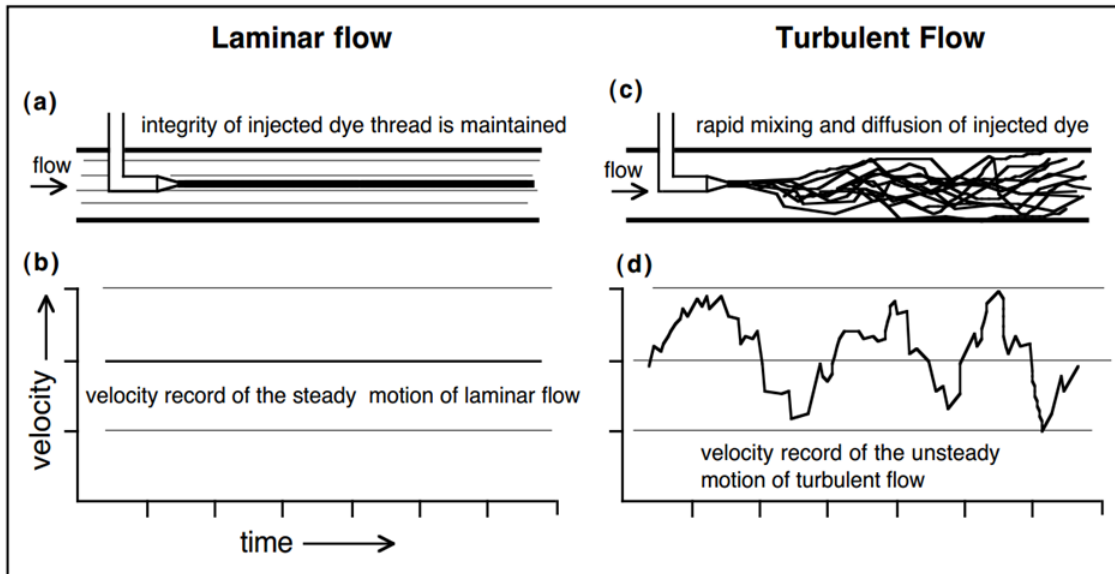


Figure 2: Reynolds experiment

Reynolds injected a thread of dye into a laminar flow passing through a glass tube and noted that the thread remained intact, displaying no tendency to mix with the surrounding fluid. The sustained integrity of the dye thread implied both steady and uniform flow and demonstrates the qualitative validity of the laminar flow model. In contrast, when he injected the same dye into the tube carrying turbulent flow, the dye thread broke up and rapidly diffused throughout the flow, thus demonstrating that turbulent mixing must have transported water particles vertically as well as in the down flow direction. Anyway the main characteristics of turbulence depend on its environment. Because of this, turbulence theory does not attempt to deal with all kinds and types of flows in a general way.

2.2 Navier-Stokes equations

Turbulence is flow dominated by recirculation, eddies and apparent randomness; it is believed that turbulent flows obey the Navier-Stokes equations, they are modeled using one of a number of turbulence models and coupled with a solver that assumes laminar flows outside a turbulent region. The Navier-Stokes equations are derived by applying the basic principles of conservation of mass, momentum and energy on a small volume of water. These equations accurately describe fluid flow for a remarkably large class of problems, by assuming that fluid behaves as a continuum rather than as discrete particles. However, inherent in these equations is the representation of velocity scales and variations that make solving them nearly impossible on present day computers except for the simplest of flow using Direct Numerical Simulation (DNS). The Navier-Stokes equations are also inherently unsteady, which means averaging multiple solutions at a series of time steps is required to produce engineering quantities such as lift and drag from a pressure solution.

For incompressible flow, the Navier-Stokes equations can be written as follows:

$$\frac{\partial u_i}{\partial t} + u_j \frac{\partial u_i}{\partial x_j} = \frac{1}{\rho} \left(-\frac{\partial p}{\partial x_i} + \mu \frac{\partial^2 u_i}{\partial x_j^2} \right) + G$$

On the left side of the equations the two terms are a transient acceleration, and a convective acceleration respectively. The two first terms on the right is the pressure gradient and a

viscous term; the term G represents the other body forces acting on the fluid, for example gravity and buoyancy forces.

The other equation needed to get a closed set of equations is the continuity equation. For an incompressible fluid (Rodi, 1980):

$$\frac{\partial u_i}{\partial x_i} = 0$$

Reynolds averaging is done by splitting the velocity variable into a time-averaged and a fluctuating part.

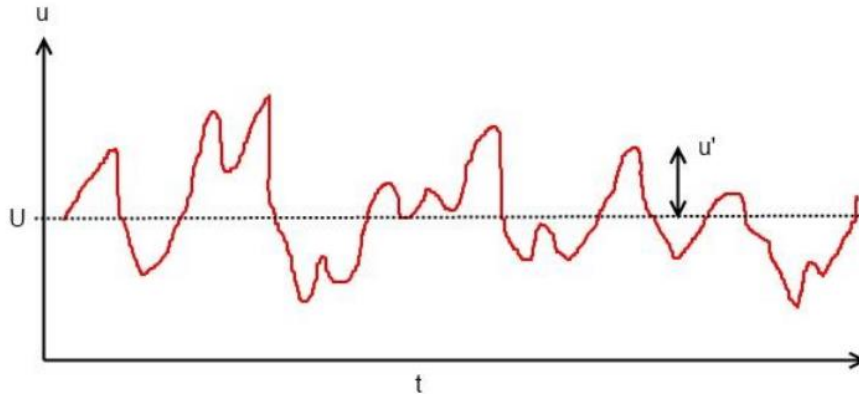


Figure 3: Reynolds averaging

$$\frac{\partial U_i}{\partial t} + \frac{\partial (U_i U_j)}{\partial x_j} = \frac{1}{\rho} \frac{\partial p}{\partial x_i} + \frac{1}{\rho} \frac{\partial \tau_{ij}}{\partial x_j} + G$$

The term τ_{ij} represents the time-averaged fluctuating velocities from the Reynolds averaging. The effect of the term can be seen as a diffusion of the momentum due to turbulence. As it works as an added stress on the fluid, it is often called the turbulent stress, or Reynolds stress. The Reynolds stress is usually modeled by introducing another equation, the Boussinesq approximation:

$$\tau_{ij} = -\rho \nu_t \left(\frac{\partial U_i}{\partial x_j} + \frac{\partial U_j}{\partial x_i} \right) + \frac{2}{3} \delta_{ij} k$$

It is assumed here that the Reynolds stress is proportional to the mean velocity gradients. This introduces the eddy-viscosity ν_t which then have to be modeled by turbulence model.

2.3 Reynolds-Averaged Navier-Stokes equations

Decomposing the Navier-Stokes equations into the RANS equations makes it possible to simulate practical engineering flows. The reduced computational requirements for the RANS equations, while still significant, are orders of magnitude less than the required for the original Navier-Stokes equations. Another advantage of using the RANS equations for steady fluid flow simulation is that the mean flow velocity is calculated as a direct result without the need to average the instantaneous velocity over a series of time steps.

It is a relatively straightforward process to produce an unsteady variant of the RANS equations for transient flows, while still solving for the mean flow velocity separately from the turbulent velocity fluctuations.

However, the RANS equations are primarily used to describe turbulent flows. These equations can be give approximate time-averaged solutions to the Navier-Stokes equations. For a stationary, incompressible Newtonian fluid, these equations can be written in Einstein notation as:

$$\rho \bar{u}_j \frac{\partial \bar{u}_i}{\partial x_j} = \rho \bar{f}_i + \frac{\partial}{\partial x_j} \left[-\bar{p} \delta_{ij} + \mu \left(\frac{\partial \bar{u}_i}{\partial x_j} + \frac{\partial \bar{u}_j}{\partial x_i} \right) - \rho \overline{u'_i u'_j} \right]$$

The left hand side of this equation represents the change in mean momentum of fluid element owing to the unsteadiness in the mean flow and the convection by the mean flow. This change is balanced by the mean body force, the isotropic stress owing to the mean pressure field, the viscous stresses and the apparent stress ($-\rho \overline{u'_i u'_j}$) owing to the fluctuating velocity field, generally referred to as the Reynolds stress. This nonlinear Reynolds stress term requires additional modeling to close the RANS equations for solving, and has led to the creation of many different turbulence models. The time average operator is a Reynolds operator.

2.4 Turbulence models

Reynolds-Averaged Navier-Stokes equations represent transport equations only for the mean flow quantity with all the scales of turbulence being modelled. The standard k- ϵ model is a semi-empirical model, which is valid only for fully turbulent flows. The model is based on model transport equations for the turbulent kinetic energy k, and its dissipation rate ϵ . The turbulent viscosity is computed from these scalars. The k- ϵ formulation is derived using a high Reynolds number hypothesis; also near wall treatment is based on the application of wall functions, rather than solving the governing equations inside the boundary layer. The standard k- ϵ model has proven very successful for numerous engineering applications. The RNG k- ϵ model is derived using a rigorous statistical method called re-normalization group (RNG). It involves a theory for the large scales, in which the effects of the small scales are represented by modified transport coefficients. A basic characteristics of the RNG k- ϵ model is that it involves an analytically derived differential formula for effective viscosity that accounts for low-Reynolds-number effects. This feature combined with an appropriate treatment of the near-wall region makes the RNG k- ϵ model more accurate and reliable than the standard k- ϵ model. The standard k- ω model is based on model transport equations for k and the turbulence frequency ω . The turbulent viscosity is computed from these scalars. The SST (Shear Stress Transport) model combines the k- ϵ and the k- ω models using a blending function. The SST model activates the k- ω model in the near-wall region and the k- ϵ model for the rest of the flow. By this approach, the attractive near-wall performance of the k- ω model is utilized without the potential errors resulting from the free stream sensitivity of that model.

2.5 Gravel bed evolution

The problem of sediment transport has been investigated theoretically in many ways. As pointed out by Fredsoe (1982) and Sumer and Bakioglu (1984), classical stability analysis neither provides a description of the details, such as the ultimate shape of the bed form and flow separation and reattachment over developed bed forms, nor predicts the distribution of pressure and friction over the bed, which determine the mean friction factor and the interaction between the flow and the sediment. Indeed, prediction of the evolution of bed forms following their initiation by instability mechanisms requires a more detailed treatment of the flow, particularly that near the bed.

Several contributions have been so far devoted to the study of the spatial properties of water-worked gravel bed surfaces measured both in the laboratory and in the field. In addition to conventional statistical parameters (i.e. standard deviation, skewness and kurtosis) of the bed elevation spatial distribution, second-order and high-order structure functions have been proved particularly helpful for exploring the statistical properties and potential multiscaling behavior of bed elevations fields (Aberle and Nikora 2006). In a recent study, the multiscaling statistical structure of the temporal evolution of bed elevation fluctuations at several locations on the evolving gravel bed under steady conditions has also been analyzed and the presence of a multiscaling behavior has been reported (Singh et al. 2008).

In a gravel bed channel, a wider grain size distribution may produce more variable bed forms particularly when grains of different size tend to sort and produce bed forms of different size. On the other hand, two fluvial beds with similar grain size distribution, subjected to different discharge rates, will produce larger and more variable bed forms at higher discharge as compared to lower discharge.

As a result of a wide range of scales of bed forms produced by the combination of grain size and flow conditions, the turbulence field will be different, perhaps more variable in the presence of many scales and sizes of bed forms.

Over a rough boundary, such as in a gravel bed channel, friction created by individual gravel bed particles or cluster of particles retards the flow velocity but the effect diminishes with increasing height above the bed. This surface roughness creates near-bed turbulence which is responsible for entrainment of particles predominately linked to sweeps, bursts and larger coherent structures. In spite of the important role that these macro turbulent structures could play in the dynamics of rivers, there is no model that relates the interaction of turbulent flow structures to bed topography and sediment transport.

This is partly due to the unavailability of long reliable records of turbulent data sampled at high resolution and partly due to the presence of complex bed topography varying spatially and temporally in a gravel bed channel.

The present study however concentrates on the turbulent flow field over an artificial fixed gravel bed with a closer look to how the micro topography of the bed exerts a significant effect on the generation of turbulent flow structures.

3 CFD MODEL IN STAR-CCM+

STAR CCM+ provides the world's most comprehensive engineering physics simulation inside a single integrated package. Much more than just a CFD solver, STAR CCM+ is an entire engineering process for solving problems involving flow, heat transfer and stress. It provides a suite of integrated components that combine to produce a powerful package that can address a wide variety of modeling needs. STAR CCM+ is based on object-oriented programming technology. It is designed to handle large models quickly and efficiently using a unique client-server architecture that seamlessly meshes and simultaneously solves and post-processes over multiple computing resources without requiring additional effort from the user. STAR CCM+ recently became the first commercial CFD package to mesh and solve a problem with over one billion cells. STAR CCM+'s single integrated process provides the fastest most automatic route from complex CAD to CFD mesh. Advanced automatic meshing technology generates either polyhedral or predominantly hexahedral control volumes at the touch of a button, offering a combination of speed, control and accuracy. For problems involving multiple frames of reference, fluid structure interaction and conjugate heat transfer, STAR CCM+ can automatically create conformal meshes across multiple physical domains. An important part of mesh generation for accurate CFD simulation is the near-wall region, or extrusion layer mesh. STAR CCM+ automatically produces a high quality layer mesh on all walls in the domain. In addition, it is possible to control the position, size, growth rate and number of cell layers in the extrusion-layer mesh. (User guide STAR CCM+ 8.06.005-R8)

3.1 Introduction

Computational Fluid Dynamics, usually abbreviated as CFD, is a branch of Fluid Mechanics that uses numerical methods and algorithms to solve and analyze problems that involve fluid flow. CFD breaks down a fluid domain into discrete cells (a mesh) and then solves the RANS and conservation laws in each cell. The accuracy of a typical CFD simulation is primarily determined by the mesh resolution and the turbulence model. In its early days CFD was often controversial, as it involved additional approximation to the governing equations and raised additional issues. Nowadays CFD is an established discipline alongside theoretical and experimental methods. This position is in large part due to the exponential growth of computer power which has allowed tackling larger and more complex problems. The central process in CFD is the process of discretization, i.e. the process of taking differential equations with an infinite number of degrees of freedom and reducing it to a system of finite degrees of freedom. Hence, instead of determining the solution everywhere and for all times, will be satisfied with its calculation at a finite number of locations and at specified time intervals. The partial differential equations are then reduced to a system of algebraic equations that can be solved on a computer.

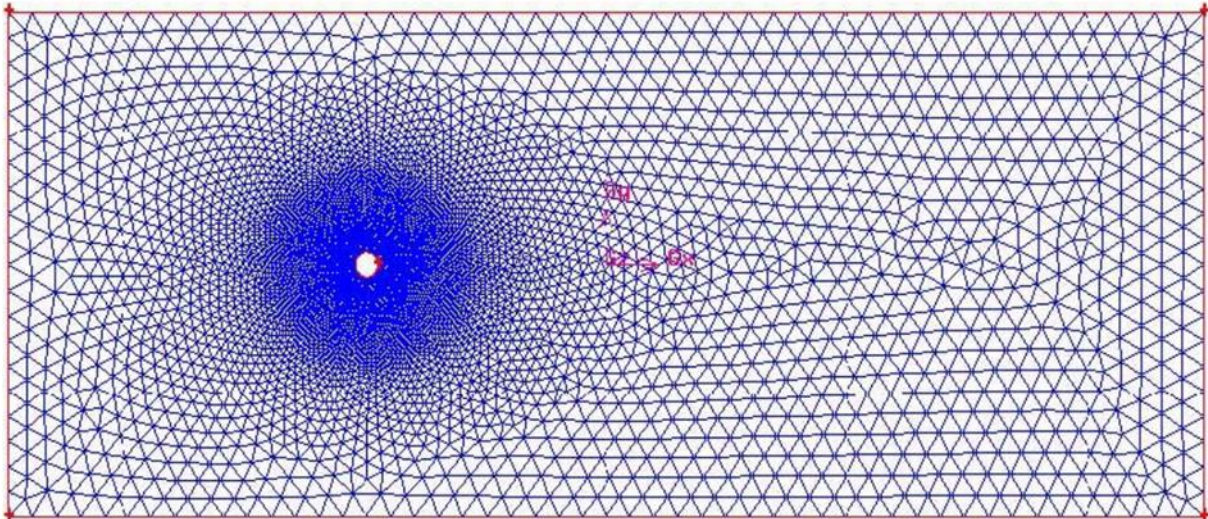


Figure 4: Process of discretization

The nature and characteristics of the errors must be controlled in order to ensure that:

- ✓ The correct equations are solved (consistency property);
- ✓ The error can be decreased as the number of degrees of freedom is increased (stability and convergence);

Once these two criteria are established, the power of computing machines can be leveraged to solve the problem in a numerically reliable fashion. Various discretization schemes have been developed to cope with a variety of issues. The most notable for our purposes are:

- Finite difference methods;
- Finite volume methods;
- Finite element methods;
- Spectral methods.

3.2 Pre-processing

Simulation is a broad subject area that is currently used to analyze a design products and processes. Within simulations is possible to investigate different aspects like structural, as well as thermal and fluid flow, however the basis for all simulation software and studies is the mesh, also called the “grid”. So before starting any simulation, to get any result the first step followed is creating a mesh or a CFD CAD model. The meshing is an extremely critical part of CFD process and without understanding it we cannot proceed to solve or even expect any relevant results. Also the accuracy of the CFD simulation results is directly linked to meshing: the better the mesh in quality, the more accurate results can be expected. Almost 50% of the CFD simulation time of any CFD engineer is involved into meshing or mesh generation and hence it is a critical part of the CFD simulation process that needs detailed understanding of the meshing/grid generation steps. Pre-processing means, before moving ahead to the solver, the needing to process CAD model in order to fit into the solver or provide the solver with the correct information. Within pre-processing the geometry is created as well as the clean-up performing so that unwanted parts if any are deleted or modified. Further is possible to generate the mesh and specify the boundary conditions. Basically a mesh is required because by physics or mathematical theory the variables are solving like flow and heat transfer and any other variable at these cell centers or nodes. Also the theoretical method that are used for any CFD study like the fine difference method, finite element method and the finite volume method actually solve the variable at these discrete cells/node.

There are different types of grid/cell shapes e.g. triangles, quadrilateral, tetrahedral, hexahedral: a grid or mesh is a collection of all these elements.

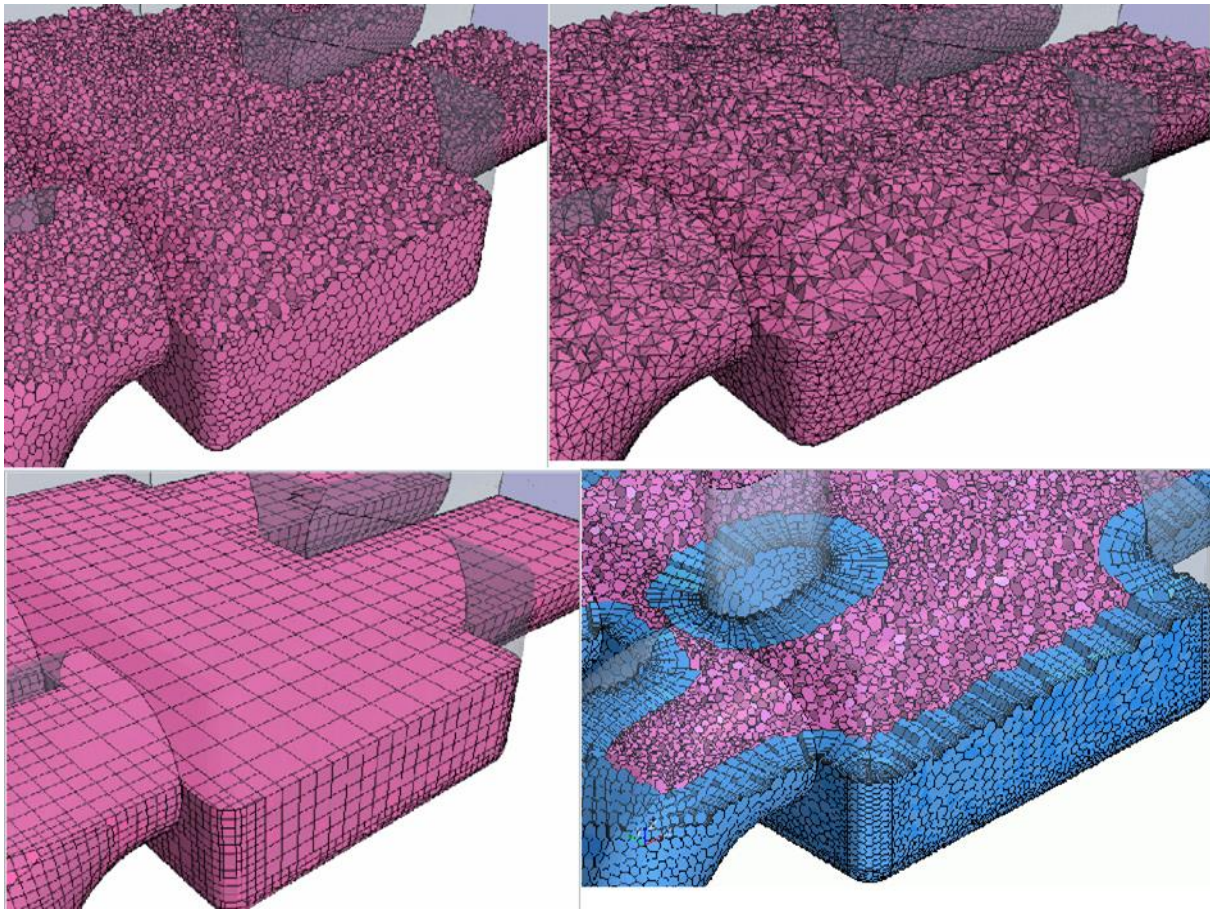


Figure 5: Different mesh shapes

3.3 Mesh models

The typical types of grid/mesh used for commercial software for academic or industrial applications are:

1. Cartesian;
2. Structured;
3. Unstructured;
4. Hybrid;

The mesh generally may not always consist of a single type of elements: sometimes is necessary to use different meshing techniques to shape the model in order to capture the shape of a particular CAD model. The mesh elements therefore at the same time may consist of Cartesian, structured, unstructured and hybrid mesh.

Structured grid: a single block is used to cover the entire geometry, also used for single shapes, where a single block is sufficient for covering the CAD model.

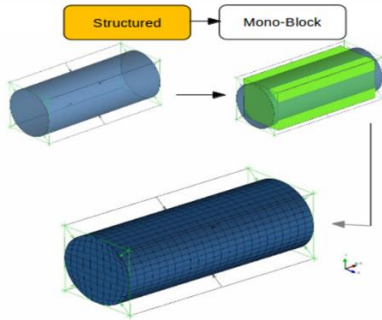


Figure 6: Structured grid

In a structured mesh, elements are aligned in a specific manner or they follow a structured pattern. Conversely, if the elements are arranged in a random fashion they are called unstructured mesh.

Unstructured grid: it is the entire discrete cells generating within the CFD are randomly spaced and do not follow any single pattern.

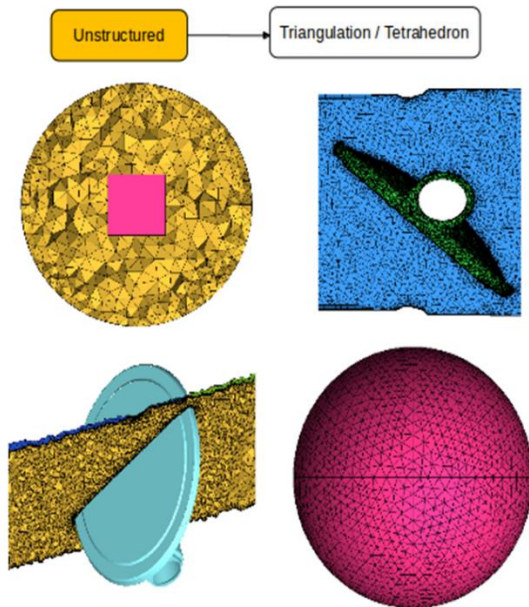


Figure 7: Unstructured grid

However the way the grid is constructed is always important for the accuracy and convergence of the solution, especially when modeling complex geometries as well as the shape of the cells in the grid. Olsen (2011b) lists three cell characteristics that are important:

- Non-orthogonality: this means the magnitude of the angle of the grid line intersection. This should be as close to orthogonal as possible.
- Aspect ratio: the ratio between the cells length in x, y and z direction. The anisotropy of cells should not be too large.
- Expansion ratio: the size difference between neighboring cells, the expansion ratio should not be too large.

It is very important to establish a proper grid resolution before attempting to solve any CFD problem; fortunately most of these meshing techniques are common to various CAE tools.

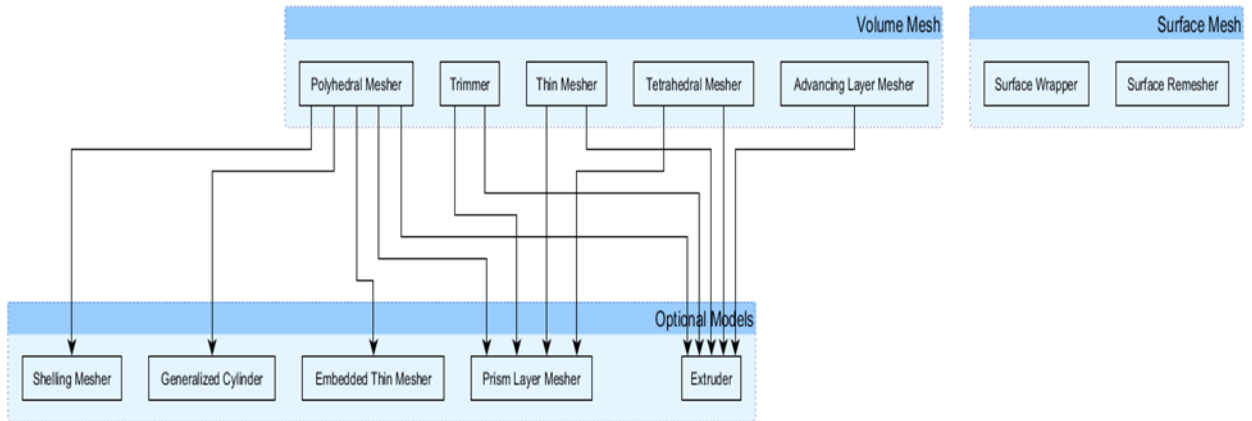


Figure 8: Mesh process

3.3.1 Surface mesh

Surface wrapper: wraps the initial surface to provide a closed and manifold surface mesh from a complex geometry. For poor quality or complex CAD, this procedure ensures that the geometry is closed and of sufficient quality for generating surface and volume meshes. The surface wrapper comes with a tool for leak detection and is usually used in conjunction with the surface remesher.

Surface remesher: re-meshes the initial surface to provide a quality discretized mesh that is suitable for CFD. It is used to re-triangulate the surface based on a target edge length supplied and can also omit specific surfaces or boundaries preserving the original triangulation from the imported mesh.

3.3.2 Volume mesh

Trimmed: generates a volume mesh by cutting a hexahedral template mesh with the geometry surface. It is recommended when an underlying custom mesh needs to be used or if the surface quality is not good enough for a polyhedral mesh. Besides, it is useful in modeling external aerodynamic flows due to its ability to refine cell in a wake region, unsteady and turbulent fluid caused by boundary layer separation.

Polyhedral mesher: generates a volume mesh that is composed of polyhedral shaped cells. It is numerically more stable, less diffusive and more accurate than an equivalent tetrahedral mesh. Moreover, also contains approximately five times fewer cells that a tetrahedral mesh for a given starting surface.

Tetrahedral mesher: generates a volume mesh that is composed of tetrahedral shaped cells. According to CD-Adapco, tetrahedral meshes are only recommended when comparisons have to be made with legacy tetrahedral models.

Advancing layer mesher: creates a volume mesh composed of prismatic cell layers next to wall boundaries and a polyhedral mesh elsewhere. The mesher creates a surface mesh on the wall and projects it to create the prismatic cell layers. The prismatic cell layers help capture the boundary layer, turbulence effects and heat transfer near wall boundaries.

Thin mesher: generates a prismatic layered volume mesh for thin geometries, where good quality cells are required to capture the solid material thickness adequately.

3.4 Physics models

STAR CCM+ includes both implicit and explicit unsteady models. For modeling turbulence it includes several RANS models, including the standard and realizable $k-\epsilon$ models, as well as Reynolds's Stress and LES/DES capabilities. Fluids can be modeled as ideal gas, real gas or

incompressible. Multiphase model capabilities include VOF and Eulerian multiphase (CD-Adapco, 2011). For modeling free surface flows a multiphase-model can be combined with VOF algorithms.

3.4.1 *Multiphase mixture material*

Most simulations will involve modeling a substance such as air, water, aluminum or mixtures of gases and fluids. The material model is responsible for managing the material, i.e. substance or substances, being simulated in the continuum. The material, in turn, is responsible for managing the various thermodynamic and transport properties relevant to that material and to the physical processes being modeled in the continuum. There are three general types of material models available in STAR-CCM+: single-component, multi-component and multiphase mixture. The multiphase mixture material model is for simulating two or more immiscible phases, where each phase is composed of a pure gas or liquid substance, such as air or water. When several of those phases exist in equilibrium together, the thermodynamic condition of equilibrium is described in terms of a system property g , or Gibbs functions:

$$g = h - Ts$$

Which is minimized at thermodynamic equilibrium.

3.4.2 *Fundamental equations*

All of fluid dynamics is based on three physical principles:

- Mass is conserved (i.e. mass can be neither created nor destroyed);
- Newton`s second law: $F = ma$;
- Energy is conserved: it can only change from one form to another.

These physical principles are developed into the fundamental governing equations of fluid dynamics: the continuity, momentum and energy equations. These equations are also known as transport equations or conservation equations. Continuity equation is already presented in chapter 2.2 introducing the RANS equations that obviously come from it.

Applying the first physical principle to a finite control volume fixed in space, at a point on the control surface, the flow velocity is V and the vector elemental surface area is dS . Also dV is an elemental volume inside the control volume.

3.4.3 *Momentum equation*

Newton`s second law can be written in a more general form as

$$\mathbf{F} = \frac{d}{dt} (m\mathbf{V})$$

Which reduces to $F = ma$ for a body of constant mass. In the equation, mV is the momentum of a body mass m . On the left side, the force exerted on the fluid as it flows through the control volume comes from two sources:

1. Body forces: gravity, electromagnetic forces or any other forces which act at distance on the fluid inside V .
2. Surface forces: pressure and shear stress acting on the control surface S .

On the right hand side, the time rate of change of momentum of the fluid as it sweeps through the fixed control volume is the sum of two terms:

1. Net flow of momentum out of control volume across surface S ;
2. Time rate of change of momentum due to unsteady fluctuations of flow properties inside V .

Hence, Newton`s second law applied to a fluid flow is:

$$-\iint_S p \, d\mathbf{S} + \iiint_V \rho \mathbf{f} \, dV + \mathbf{F}_{\text{viscous}} = \frac{\partial}{\partial t} \iiint_V \rho \mathbf{V} \, dV + \iint_S (\rho \mathbf{V} \cdot d\mathbf{S}) \mathbf{V}$$

This can be rewritten as partial differential equations that relate flow-field properties at any point in the flow:

$$\begin{aligned} \frac{\partial(\rho u)}{\partial t} + \nabla \cdot (\rho u \mathbf{V}) &= -\frac{\partial p}{\partial x} + \rho f_x + (\mathcal{F}_x)_{\text{viscous}} \\ \frac{\partial(\rho v)}{\partial t} + \nabla \cdot (\rho v \mathbf{V}) &= -\frac{\partial p}{\partial y} + \rho f_y + (\mathcal{F}_y)_{\text{viscous}} \\ \frac{\partial(\rho w)}{\partial t} + \nabla \cdot (\rho w \mathbf{V}) &= -\frac{\partial p}{\partial z} + \rho f_z + (\mathcal{F}_z)_{\text{viscous}} \end{aligned}$$

Where the subscripts x, y and z on f and F denote the x, y and z components of the body and viscous forces, respectively.

3.4.4 Energy equation

For a study of incompressible flow, the continuity and momentum equations are sufficient tools to do the job. However, for a compressible flow, there is the needing of an additional fundamental equation to complete the system. This fundamental relation is the energy equation. The physical principle on which the energy equation lies is the first law of thermodynamics: “Energy can be neither created nor destroyed; it can only change in form”, which can be stated as:

$$\delta q + \delta w = de$$

Where δq and δw represent an incremental amount of heat and work respectively, which are forms of energy, that when added to the system, change the amount of internal energy de in the system. This physical principle, through a control volume, can be directly translated into:

$$\begin{aligned} \iiint_V \dot{q} \rho \, dV + \dot{Q}'_{\text{viscous}} - \iint_S p \mathbf{V} \cdot d\mathbf{S} + \iiint_V \rho (\mathbf{f} \cdot \mathbf{V}) \, dV + \dot{W}'_{\text{viscous}} \\ = \frac{\partial}{\partial t} \iiint_V \rho \left(e + \frac{V^2}{2} \right) \, dV + \iint_S \rho \left(e + \frac{V^2}{2} \right) \mathbf{V} \cdot d\mathbf{S} \end{aligned}$$

And in the form of partial differential equations as

$$\begin{aligned} \frac{\partial}{\partial t} \left[\rho \left(e + \frac{V^2}{2} \right) \right] + \nabla \cdot \left[\rho \left(e + \frac{V^2}{2} \right) \mathbf{V} \right] \\ = \rho \dot{q} - \nabla \cdot (p \mathbf{V}) + \rho (\mathbf{f} \cdot \mathbf{V}) + \dot{Q}'_{\text{viscous}} + \dot{W}'_{\text{viscous}} \end{aligned}$$

Where $\dot{Q}'_{\text{viscous}}$ and $\dot{W}'_{\text{viscous}}$ represent the proper forms of the viscous terms.

These equations are fundamental to all of aerodynamics making a total of five equations with five accompanying independent variables, namely pressure, three components of velocity and temperature. Also, a thermodynamic equation of state can be added to the set to relate density to the pressure, temperature and composition. Exact analytical solutions of the complete Navier-Stokes equations exist for only a few very specialized cases. Fortunately, many

problems of engineering interest are adequately described by simplified forms of the full equations, which can often be solved easily.

3.5 Boundary conditions

Boundaries are the surfaces that surround the solution domain. Setting some boundary conditions is necessary to get a closed set of equations that can be solved from the discretized Navier-Stokes equations. The types of boundaries usually used for a free-surface calculation is:

- Inflow boundaries;
- Outflow boundaries;
- Wall boundaries.

STAR CCM+ incorporates several types of boundaries including:

- ✓ Velocity Inlet: inflow is defined as a velocity vector field;
- ✓ Mass-Flow Inlet: the inflow is defined as mass per unit time;
- ✓ Stagnation Inlet: inflow is defined by a known stagnation pressure;
- ✓ Split flow Outlet: the fraction of fluid exiting through the outlet is defined;
- ✓ Pressure Outlet: the static pressure is defined at the boundary.

3.5.1 Wall laws

STAR-CCM+ employs three different models for near-wall treatment, the high-, low- and all- y^+ models. The high- y^+ model assumes that the cell closest to the wall is within the logarithmic region of the boundary layer while the low- y^+ model assumes that the grid is so fine that the viscous sub-layer is properly resolved. The all- y^+ model is a hybrid that uses low y^+ for fine meshes and high- y^+ for courser meshes. It is also formulated to produce more reasonable results for intermediate meshes.

3.6 Modeling techniques

There have been many finite difference techniques devised for the solution of fluid dynamic problems. Nearly all of these techniques can be classified as falling into one of two basic categories, depending on whether they are written primarily in terms of Lagrangian or Eulerian coordinates. Within each of these categories it is further possible to distinguish between those techniques applicable to high speed flows and those applicable to low speed.

- Lagrangian methods
 - I. The grid moves and follows the shape of the interface;
 - II. Interface is specifically delineated and precisely followed;
 - III. Suited for viscous, laminar flows;
 - IV. Problems of mesh distortion, resulting in instability and internal inaccuracy;
- Eulerian methods
 - I. Fluid travels between cells of the fixed mesh and there is no problem with mesh distortion;
 - II. Adaptive grid techniques;
 - III. Fixed grid techniques, e.g. volume of fluid (VOF) method.

The Lagrangian specification of the flow field is a way of looking at fluid motion where the observer follows an individual fluid parcel as it moves through space and time. Plotting the position of an individual parcel through time gives the path line of the parcel. This can be visualized as sitting in a boat and drifting down a river. The Eulerian specification of the flow field is a way of looking at fluid motion that focuses on specific locations in the space through which the fluid flows as time passes. This can be visualized by sitting on the bank of a river and watching the water pass the fixed location. The Lagrangian and Eulerian specification of the flow field are sometimes loosely denoted as the Lagrangian and Eulerian frame of reference. However, in general both the Lagrangian and Eulerian specification of the flow field can be applied in any observer's frame of reference, and in any coordinate system used within the chosen frame of reference.

3.6.1 Volume of fluid (VOF)

The most common method used in CFD programs based on the finite volume method is the volume of fluid method (VOF). The volume of fluid method in STAR-CCM+ is used to govern the air and water free surface evolution (Hirt and Nichols, 1981 and Muzafferija and Peric, 1999). The use of the VOF method for typical sloshing problem implies the study of two fluids that must completely fill the tank domain. In this method, a passive scalar called volume fraction is assigned at each discretization cell, indicating the fraction of each phase in this particular cell. The scalar evolves in time with an additional transport equation in conjunction with the mass and momentum conservation laws. The VOF method is a widely used technique that has been applied to sloshing by many authors, like Kleesman et al. (2005).

Typical problems:

- Jet breakup;
- Motion of large bubbles in a liquid;
- Motion of liquid after a dam break;
- Steady or transient tracking of any liquid-gas interface.

It assumes that each control volume contains just one phase (or the interface between phases). It solves one set of momentum equations for all fluids:

$$\frac{\partial}{\partial t}(\rho u_j) + \frac{\partial}{\partial x_i}(\rho u_i u_j) = -\frac{\partial P}{\partial x_j} + \frac{\partial}{\partial x_i} \mu \left(\frac{\partial u_i}{\partial x_j} + \frac{\partial u_j}{\partial x_i} \right) + \rho g_j + F_j$$

Surface tension and wall adhesion are modeled with an additional source term in momentum equation. For turbulent flows, a single set of turbulence transport equations are solved while a volume fraction conservation equation for the secondary phase.

3.6.2 Volume fraction

It defines a step function ϵ equal to unity at any point occupied by fluid and zero elsewhere such that:

$$\epsilon_k(\text{cell}) = \frac{\iiint_{\text{cell}} \epsilon_k(x, y, z) dx dy dz}{\iiint_{\text{cell}} dx dy dz}$$

For volume fraction of fluid, three conditions are possible:

$\epsilon_k = 0$ if cell is empty;

$\epsilon_k = 1$ if cell is full;

$0 < \epsilon_k < 1$ if cell contains the interface between the fluids;

Tracking of interface between phases is accomplished by solution of a volume fraction continuity equation for each phase:

$$\frac{\partial \epsilon_k}{\partial t} + u_j \frac{\partial \epsilon_k}{\partial x_i} = S_{\epsilon_k}$$

Mass transfer between phases can be modeled by using a user-defined subroutine to specify a non-zero value for S_{ϵ_k} . Multiple interfaces can be simulated while is not possible to resolve details of the interface smaller than the mesh size.

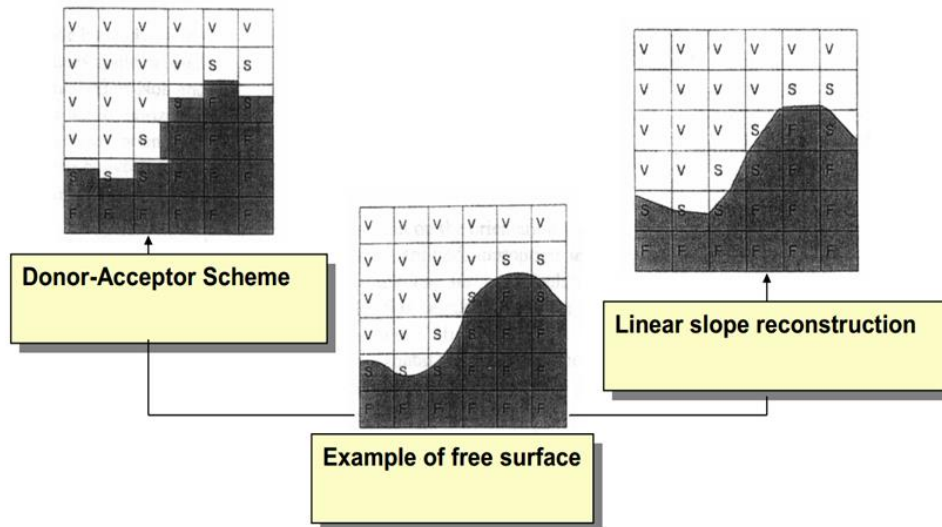


Figure 9: Volume of fluid algorithm

3.7 Turbulence models in STAR-CCM+

Turbulent flows are irregular in nature. This makes a deterministic approach to turbulence problems impossible and therefore statistical methods are used for treating turbulent flows. There are several leading computational approaches to turbulent flows and all of them fall under one of these approaches:

- Simulations, where equations are solved for a time dependent velocity field that, to some extent, represents the velocity field $U(x,t)$, for one realization of the turbulent flow.
- Turbulence models, where equations are solved for some mean quantities $\langle U \rangle$, $\langle u_i u_j \rangle$ and ϵ .

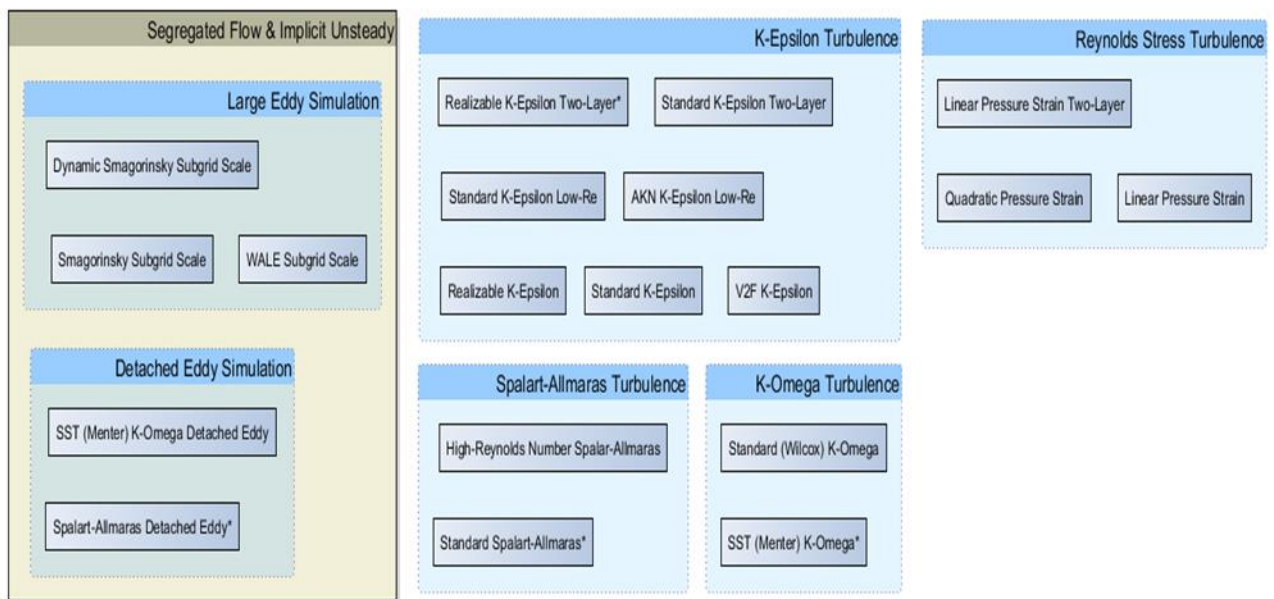


Figure 10: Turbulence models

In STAR-CCM+ the available approaches to modeling turbulence are:

- Models that give closure of the Reynolds-Averaged Navier-Stokes (RANS) equations;
- Large eddy simulation (LES);
- Detached eddy simulation (DES);

Over the years, many models have been proposed and many are currently in use. As no single turbulence model is the best for every flow simulation, it is important to follow some criteria to assess different models, such as:

1. Level of description;
2. Completeness;
3. Cost and ease of use;
4. Range of applicability;
5. Accuracy.

3.7.1 Reynolds-Average Navier-Stokes

The unsteady RANS equations are applicable to transient situations where the unsteadiness is either imposed, such as by a time-varying boundary condition, or is inherent, such as the vortex shedding in a massively separated flow. In the latter case, transient simulations often yield better results than attempting use a steady-state approach. However, successful unsteady RANS simulations require that the time scales of turbulence be disparate from the mean-flow

unsteadiness. Furthermore, the limitations of the turbulence model may preclude good unsteady results.

3.7.2 Turbulent-viscosity models

These models use the concept of a turbulent viscosity μ_t to model the Reynolds stress tensor as a function of mean flow quantities. Classes of turbulence models available in STAR-CCM+ include Spalart-Allmaras, K-Epsilon and K-Omega models.

It is the most widely used complete turbulence model and it is incorporated in most commercial CFD codes. Proposed by Shih et al. in 1994, the Realizable K-Epsilon model instead, differs from the Standard version in that it contains a new formulation for the turbulent viscosity and it has a new transport equation for the dissipation rate ε which is derived from an exact equation for the transport of the mean-square vorticity fluctuations. The term realizable means that the model satisfies certain mathematical constraints on the Reynolds stresses. The Realizable Two-Layer K-Epsilon model combines the Realizable K-Epsilon model with the two-layer approach. The coefficients in the model are identical but the model gains the added flexibility of an all y^+ wall treatment.

3.7.3 Reynolds-stress models

In Reynolds-stress models, model transport equations are solved for the individual Reynolds stress and for the dissipation rate ε . This model carries significant computations overhead as seven additional equations must be solved in three dimensions (as opposed to the two equations of a K-Epsilon model). There is also likely to be a penalty in the total number of iterations required to obtain a converged solution. This model accounts for the effects of streamline curvature, swirl, rotation and rapid changes in strain rate in a more physical manner than that by one-equation or two-equation models. So it is used for computing cyclone flows, swirling flows in combustors, rotating flow passages and the stress-induced secondary flows in ducts.

3.8 Solver

In the solver the meshed CAD model is imported and it's possible to solve the CFD problem specifying additional models like the physics, numerical computation methods etc. In contrast to meshing models where the number of options is limited, the number of choices and combinations within the physic models is almost unbounded.

3.8.1 Space

The primary function of the Space models is to provide methods for computing and accessing mesh metrics. There are four models available in STAR-CCM+, namely:

1. The Axisymmetric Model;
2. The Shell Three-Dimensional Model;
3. The Two-Dimensional Model;
4. The Three-Dimensional Model.

The two-dimensional model is designed to work on two-dimensional meshes. It is comparable to the axisymmetric model in that it represents a 2D slice of a 3D model. This model allows for rapid simulation presuming that variations of conditions in one of the directions are much less important than those in the others. The three-dimensional model is designed to work on three-dimensional meshes in cases where all spatial directions are relevant.

3.8.2 Time

Time models in STAR-CMM+ provide solvers that control the iteration and/or unsteady time stepping.

The models available are:

1. Steady;
2. Implicit Unsteady;
3. Explicit Unsteady;
4. Harmonic Balance.

The steady model is used for all steady-state calculations; this means that only spatial derivatives are discretized. In steady state calculations we wish to integrate from some arbitrary state to the asymptotic solution in any manner which will get us there in the least amount of computational work. When considering how to discretize the time derivatives, there is the need to recognize a major difference between space and time coordinates.

Most real fluid flow problems are (at least to some extent) elliptic in nature, any forcing introduced has an effect in all directions. However, time dependence is purely parabolic; any forcing affects only the future, never the past. To reflect this, solution methods tend to advance in time in a marching manner, i.e. updating the solution at each time-step. Considering a generic time-dependent problem:

$$\frac{\partial \phi}{\partial t} = f(t, \phi(t)),$$

Integrating with respect to time, over one time step, gives

$$\phi^{(n+1)} = \phi^{(n)} + \int_t^{t+\Delta t} f(t, \phi(t)) dt.$$

Where the superscript (n) denotes a quantity evaluated at time t, and (n+1) at time t+Δt. If the integral is approximated using the value of the integrand at the final time, t+Δt, then we have:

$$\phi^{(n+1)} = \phi^{(n)} f(t + \Delta t, \phi^{(n+1)}) \Delta t$$

which is a fully implicit method. It cannot be solved in a simple point wise fashion, since values of $\phi^{(n+1)}$ appear on both the left and right hand sides. In a general case it will thus often require an iterative solution procedure to obtain $\phi^{(n+1)}$.

3.9 Post-processing

Extracting results out of the CFD model that has been solved, it is called as post-processing. Here the results are analyzed using various color, contour plots, lines, contour data, graphs etc. It's possible to extract data like heat transfer coefficient, drag, lift in the analysis of gradient design and generate good analysis report.

4 PAST EXPERIMENTAL WORKS

During winter 2011/2012, the NTNU Department of Marine Technology as well as Sintef MARINTEK offered their facilities to perform stereoscopic PIV measurements. The study presented a set of experimental data obtained by these PIV measurements over an artificial copy of a gravel bed.

4.1 Artificial streambed

To produce a surface structure as close to a real gravel bed as possible, an armor layer developed in a laboratory flume at the Leichtweiß-Institute for Hydraulic Engineering in Braunschweig (Germany) was molded. The original armor layer was produced in a 30 cm wide, straight laboratory flume with an effective sediment length of 5.35 m. It developed under a constant discharge of 28.9 l/s with a mean bed slope of 5.3 ‰. A photographic line-by-number-analysis of the original armor layer provides a grain-size distribution with a geometric mean diameter of 13.50 mm.

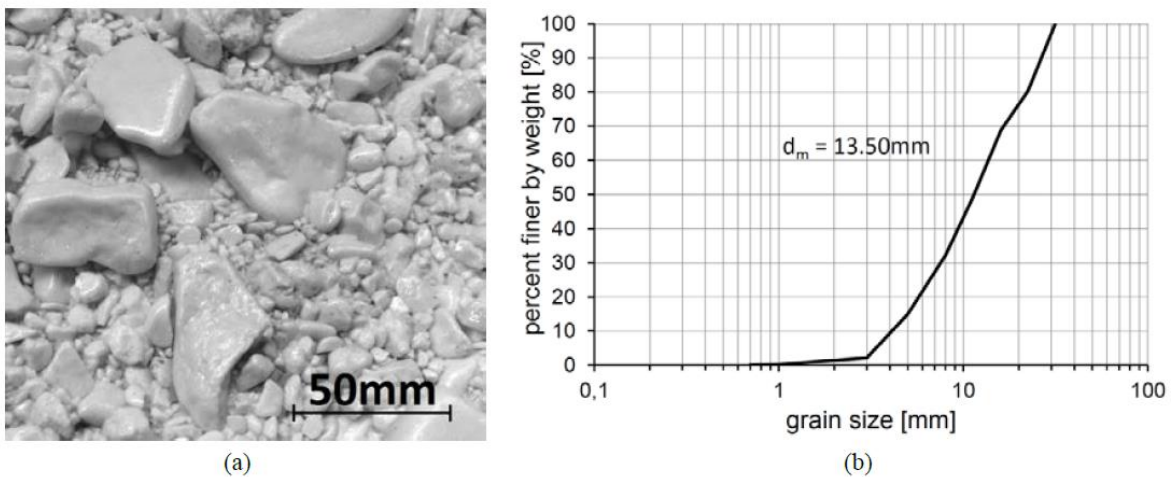


Figure 11: Grain size

4.1.1 Preparation

A wooden frame was set in position upon the armor layer before pouring the molding mass. The open room between frame and bed had to be closed as possible to assure no material was wasted



Figure 12: Preparation

4.1.2 Molding

To produce a negative imprint of the original surface structure, a liquid two-component silicone rubber was poured over the desired surface. The resulting, flexible silicone form gave the opportunity to produce riverbed duplicates with a rigid casting material.

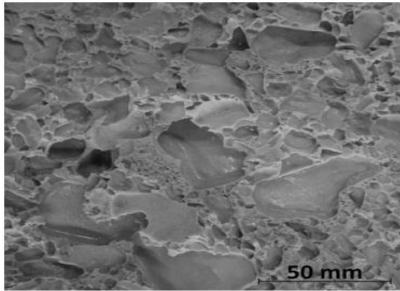


Figure 13: Molding

4.1.3 Casting

A two-component polyurethane pouring resin (PUR) was mixed and poured into the form. The form was kept steady and not moved while, during the curing process, the material warmed up. Since all produced copies come from the same form and consist of the same material, those had to be similar to each other.



Figure 15: Casting

4.1.4 Detaching and finishing

The streambed was detached from the silicone form and the whole piece was turned upside down to bring the flexible silicone side on top.



Figure 14: Detaching

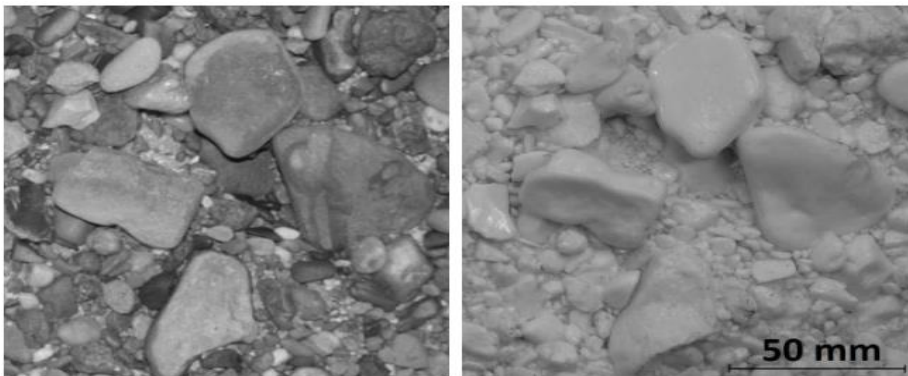


Figure 16: Result

4.1.5 Coloring

The reason to color the here described artificial riverbeds was the use of a PIV (Particle Image Velocimetry) system for the further research. This velocity measurements technique involves a flow field illumination using a laser beam, spread into a laser sheet and one or more cameras to record the reflections of the laser light scattered from small artificial tracer particles in the water. To avoid unwanted laser reflections from the streambed surface, it is expedient to color it in a dark tone. The unwanted reflections light (orange) can then be separated from the desired tracer particle reflections (green), using a filter of the PIV cameras. Three different techniques to darken the artificial riverbeds were tested:

1. A thin layer of black;
2. Liquid black resin dye;
3. A dark purple streambed which was ideal for the PIV experiments.

4.2 PIV measurements

The stereoscopic Particle Image Velocimetry system consists of two CCD cameras, positioned on either side of the flume. In 15 Hz system, each camera takes 15 double frame pictures per second so that the final amount of pictures to process is 60 images per second. For illumination, a Quantel BigSky twin 220 Nd:YAG laser with a pulse power of 220 mJ is positioned outside the flume at the downstream end, facing a glass window. The light sheet optics spread the laser beam into a vertical, 2-3 mm wide sheet along the central streamline. Since several experimental runs of different discharges between $Q=6$ l/s and $Q=90$ l/s were recorded and compared, the mean velocity for each run was different. To maintain an average displacement of about four to six pixels, the pulse distance of the double frame recordings was adjusted for each run. It varied from 13000 μ s for the 6 l/s run to 1500 μ s for the 90 l/s run.

4.3 Experimental setup

The experiments were carried out in a non-tilting straight hydraulic flume with a total length of 6.63 m. The central acrylic test section measured 2.50 m in length and 60.9 cm in width. The artificial streambed was installed within the test section. It covered the full width of the flume over a length of 1.60 m in stream wise direction.

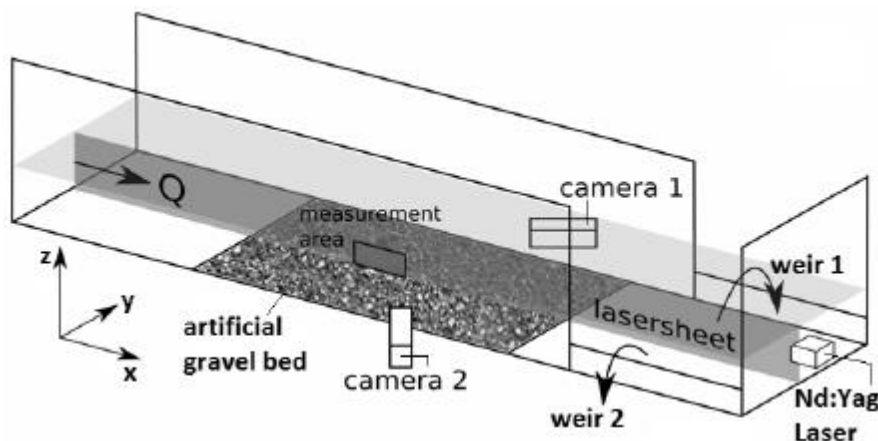


Figure 17: Experimental setup

The downstream part of the flume can be described as rather unique. Instead of a common weir at right angles with the flow direction, two separate weirs, one on each side of the flume,

are overflowed to discharge the water. The weirs were fixed at a constant height of 20 cm. A vertical laser sheet can be generated along the central streamline without penetrating the water surface by any kind of solid objects.

4.3.1 *Experimental procedure*

The experiment was divided into a number of 18 runs. Setting the pump frequency to 5 Hz, a water discharge of 6 l/s evolved. From there, the pump frequency was increased by 1 Hz for each run so that a higher discharge developed in the system. After setting up each run, at least ten minutes passed before the measurements were taken so that the new flow situation could develop and steady conditions in the whole system were reached. After that, some test pictures were taken to determine the optimal pulse distance for the PIV measurement. If necessary, the amount of tracer material was adjusted as well. Each run was measured over a total time of 40 seconds, resulting in 2400 single images and therefore 600 vector fields for further analysis. Table 1 shows all 18 runs, each with its discharge, flow depth and chosen pulse distance for the PIV measurement.

Table 1: PIV measurements

Q [l/s]	d [mm]	Pulse distance [μm]
6	134	13000
8	137	10000
10	139	8000
13	141	6800
16	146	5800
18	149	5000
21	151	4500
25	155	4200
29	160	3500
36	165	2500
42	171	2200
49	179	2200
56	183	2000
63	191	1900
71	195	1800
77	201	1700
84	204	1600
90	207	1500

4.3.2 *Treatment of vectors below roughness tops*

The vector field obtained from the PIV measurements includes some cells at the bed where all velocity components u , v and w show a value of 0 m/s. Those are actually not part of the field of view because they are blocked by exposed particles. However, other areas with the same elevation might include valid vectors. Those cells are located between the roughness tops and troughs of the rough channel surface. Assuming one wants to perform a spatial average in a horizontal direction (x) and simply averages over all cells of the same elevation, the result would highly underestimate the correct value since several, not-valid vectors were taken into account and contribute $u, v, w = 0$ to the average. To address each horizontal line of cells in the same manner, Nikora, McEwan et al. (2007) overcame this problem by introducing a “roughness geometry function” Φ_s which describes the ratio of “volume occupied by fluid within an averaging domain” V_f and the “total volume of the averaging domain” V_o . In this

case, the averaging domain includes all cells of the same elevation so that $\Phi_s(z)$ is a function depending on the elevation z , starting at $\Phi_s = 0$ below the roughness troughs because the artificial streambed is non-porous and reaching $\Phi_s = 1$ above the roughness tops. The location of the roughness tops is usually determined to be at $\Phi_s = 0.99$ (Aberle, Koll et al. 2008). In this case, $V_f(z)$ was estimated to be the amount of vectors with u , v , and $w \neq 0$ in each horizontal line, while $V_f(z)$ represents the total number of vectors in this line. Figure ... shows the double averaged (Nikora, McEwan et al. 2007) streamwise velocity profiles $[\bar{u}]$ for each run. The mean velocity for each run increases with the discharge. Figure 18 also includes the roughness geometry function in the bottom right corner. The dashed line marks the elevation of the roughness tops, estimated to be at $\Phi_s = 0.99$.

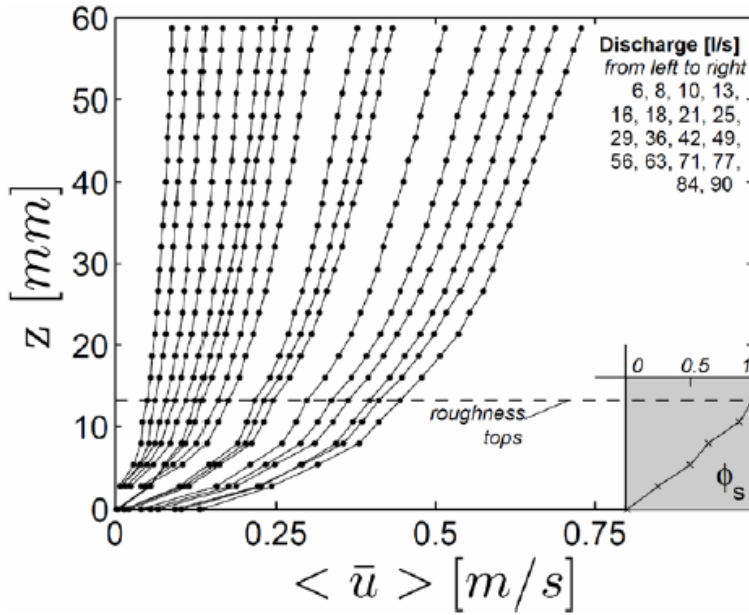


Figure 18: Experimental data

4.4 Discussion

Artificial gravel beds proved to be highly advantageous when it comes to both: image quality of PIV measurements and providing similar prerequisite conditions for a series of experiments, while providing a surface structure that is as close to a real gravel bed as it can be. However, the effect of streambed porosity, even if it can be expected to be very low in a fully developed armor layer, is lost due to the solid structure of the molded streambed. The measurement results show velocity and form induced stress distributions that correspond to other literature. The distribution of form induced stresses, presented in form of quadrant maps show clear patterns, independent of the discharge, that evolve in all 18 experimental runs.

5 NUMERICAL MODEL SETUP

Modeling is the process by which is possible to construct a simplified mathematical reality from a more complex physical reality. Using STAR-CCM+ it has been possible to re-create the geometry of the artificial gravel bed as well as the boundary conditions set in the physical model test conducted by Spiller et al. (2013)

5.1 Pre-processing

For many simulations in STAR-CCM+, the first step involves preparing the geometry of the case under investigation. Among all the import formats supported by STAR-CCM+, a Stereolithography (STL) format was used. Originally the geometry was built by more than 5 million of points, so the first step was to import this cloud of points in Rhinoceros 5 Software and then connect each point in group of three creating a surface mesh built by almost 2 million of triangular, the so called STL format. As described in the introduction, the quality of the surface data were usually not good and some additional work was required before the geometry was usable. First, the STL file was imported in STAR-CCM+ setting the vertex merge tolerance at 1.0E-5m and then the Surface Preparation tool was launched. This tool provides diagnostic checks for assessing the validity of surfaces, and a range of tools by which surfaces can be repaired. The repair tools provide the following capabilities listed in

Table 2: Repair tools

Repair mode	Capabilities
Repair surface mesh	<ul style="list-style-type: none"> • Diagnose and locate surface issues • Delete and create faces and edges • Collapse and smooth vertices • Fill and patch holes • Split and swap edges • Zip edges • Remesh faces locally, with or without feature retention • Project and transform vertices • Merge duplicate faces and close vertices • Automatic repair to fix issues relating to poor quality, close proximity, and pierced faces.

Afterwards, the described geometry was duplicated in three parts, perfectly joint, in order to have a bed surface measuring 2.50 m in length and 60.9 cm in width, according to the Experimental procedure by Spiller et al. (2013)

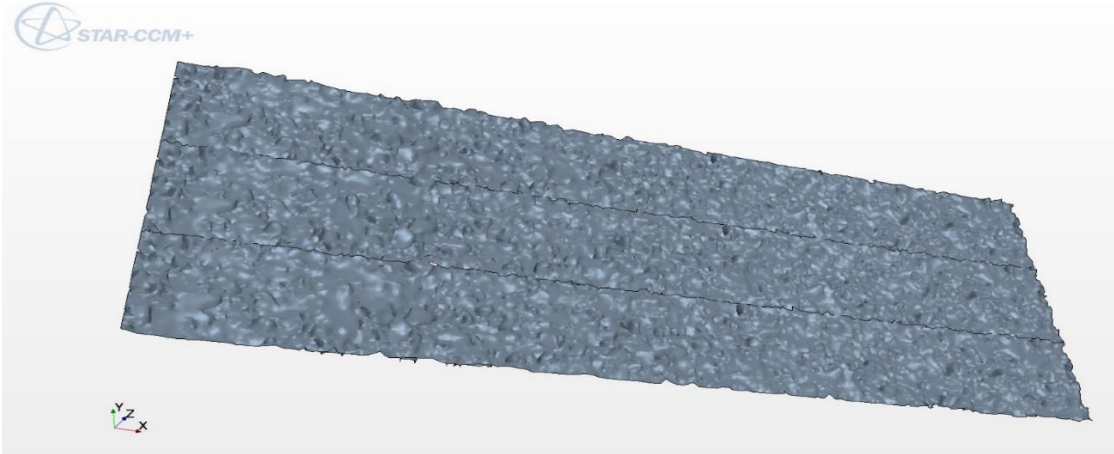


Figure 19: Geometry model

5.2 Mesh

In order to have a volume in which the flow develops, a block around the bed surface was created and split by patch in bottom, top, inlet, outlet and sides, before generating the mesh. The following step was to create a mesh continuum and select its meshing models as listed in

Table 3: Mesh procedure

Meshers	Meshing models	Capabilities
Surface meshers	<i>Surface Wrapper</i>	Wraps the initial surface to provide a closed and manifold surface mesh from complex geometry
	<i>Surface Remesher</i>	Remeshes the initial surface to provide a quality discretized mesh that is suitable for CFD
Volume meshers	<i>Trimmed Mesher</i>	Generates a volume mesh by cutting a hexahedral template mesh with the geometry surface
	<i>Prism layer Mesher</i>	Adds prismatic cell layers next to wall boundaries

To generate a volume mesh in STAR-CCM+, the surface mesh has to be closed, manifold and free of pierced faces (intersections). The mesh should also have good triangulation quality.

The result of a surface wrapping operation is a closed surface that may require further remeshing to improve mesh quality.

The surface remesher is used to retriangulate a closed starting surface to obtain a high-quality surface mesh. It is used to improve surface meshes from the surface wrapper or to improve the quality of imported tessellated geometry.

5.2.1 Trimmed Mesher

Among the different volume meshers tested, Trimmed mesher was chosen due to the following reasons:

1. It provides a robust and efficient method of producing a high-quality grid;
2. It combines a number of highly desirable meshing attributes in a single meshing scheme;
3. Since the simple shape on which the grid is generated, the process of convergence, so the number of iterations, is faster in comparison with other different mesh models.

By default, the trimmer meshing model utilizes a template mesh that contains refinement based on the local surface mesh size and local refinement controls.

Growth parameters can be used to control the transitioning of the mesh cell sizes from small to large both at the surface and far field.

A maximum and/or minimum cell size can be supplied as well to control the upper and lower cell size bounds.

The template can be aligned in any direction in a user specified cartesian coordinate system. In Figure 20 the resulting mesh next to the bed channel is shown.

It is composed predominantly of hexaedral cells with trimmed cells next to the surface.

Trimmed cells are polyhedral cells but can usually be recognized as hexahedral cells with one or more corners and/or edges that are cut off.

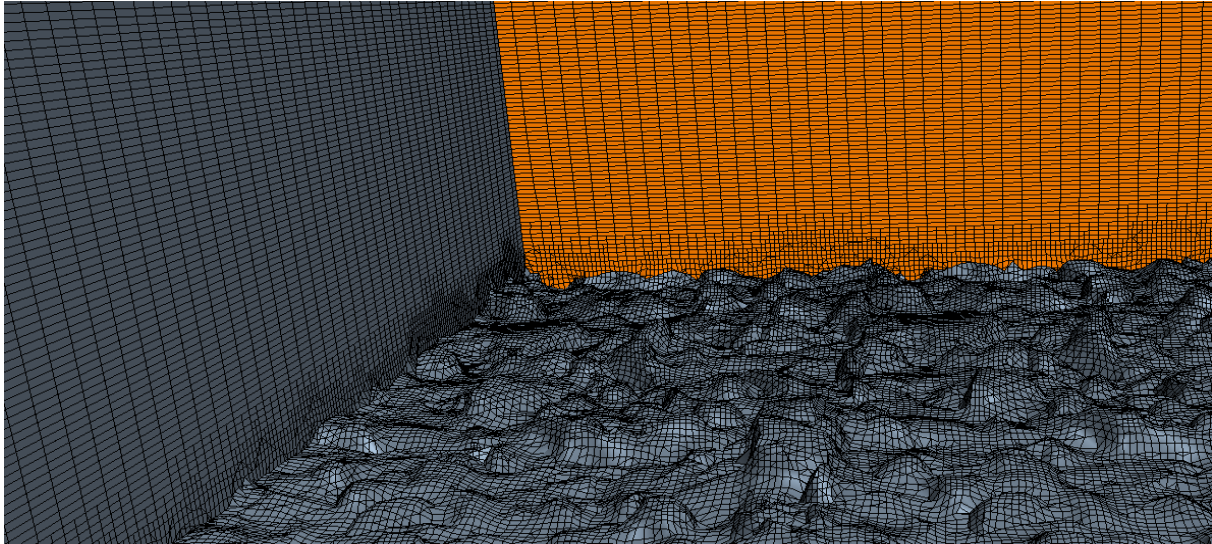


Figure 20: Mesh accuracy

5.2.2 Grid

Since the velocity profile from experimental data of Spiller et al. (2013) reported velocity values along cross section each 3 mm from bottom until 60 mm, for this simulation 3 mm was used in the area of analysis. In order to validate the model as well as to have more data to be compared and catch the differences using one mesh instead of another, a mesh size of 5 mm was used as well with the same boundary conditions.

Table 4 and Table 5 sum up the grid properties for the STAR-CCM+ model used, both for the first and second size.

Table 4: 5 mm mesh size

COARSE MESH			
Cell count	1.099.102		
Face count	3.241.699		
Base size	20.0 mm		
Prism Layer Thickness	Relative size	5.0 mm	25% Base size
Surface Growth Rate	1.3		
Surface size	Relative minimum size	20 mm	
	Relative Target size	20 mm	
Volumetric control	Trimmer Anisotropic size	x	12 mm
		y	12 mm
		z	5 mm

Table 5: 3 mm mesh size

FINE MESH			
Cell count	2.254.221		
Face count	6.601.113		
Base size	20.0 mm		
Prism Layer Thickness	Relative size	5.0 mm	25% Base size
Surface Growth Rate	1.3		
Surface size	Relative minimum size	20 mm	
	Relative Target size	20 mm	
Volumetric control	Trimmer Anisotropic size	x	10 mm
		y	10 mm
		z	3 mm

Base size refers to a characteristic size used in mesh generation. The volumetric control allows to specify the mesh density in a specific zone for both surface and volume meshes, creating in this way, two different grids for active and inactive area. In order to have a refinement into the volume it's supposed water develops, a volume shape has been created. The block shape used is a rectangular volume that is aligned with either the global or a local xyz axis. The grid dimensions are specified in Table 4 for first mesh and in Table 5 for the second one. Choosing the trimmer anisotropic cell sizes, it has been possible to specify a different cell size in each coordinate direction, in particular: 60% of base size along x and y direction while 25% of base size along z direction for coarse mesh; 50% of base size along x and y direction and 15% in z direction for the fine mesh. A non-uniform mesh in the vertical and horizontal direction proved to be sufficient to modeling the system. The meshing size is comparatively small near the boundaries, sides and bed, so a good estimate of the gradients is obtained. The choice of 3 mm is justified by the fact that the difference between the values found is less than 2%.

In Figure 21 and Figure 22 the longitudinal and transversal grid along the channel for the coarse mesh.

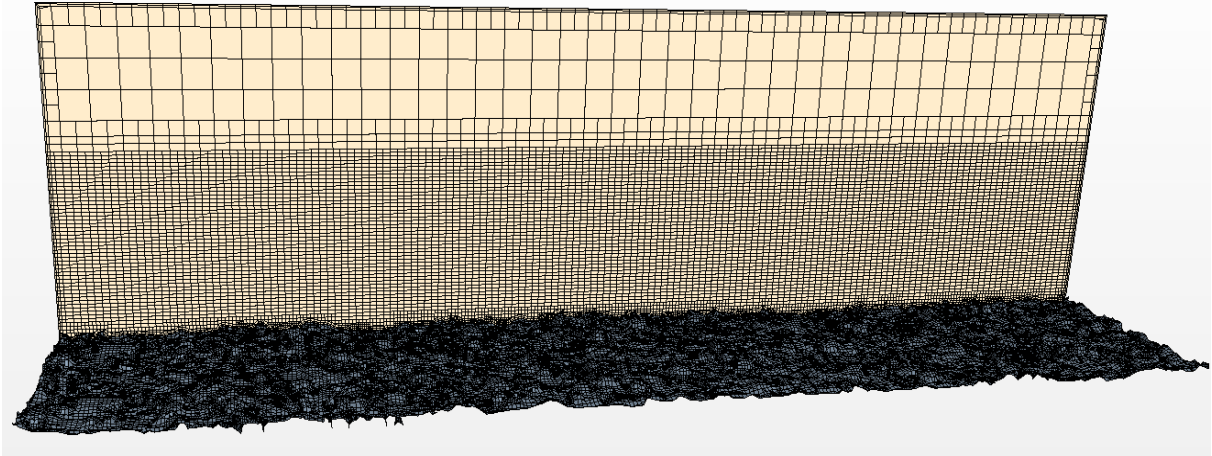


Figure 21: 5 mm longitudinal mesh

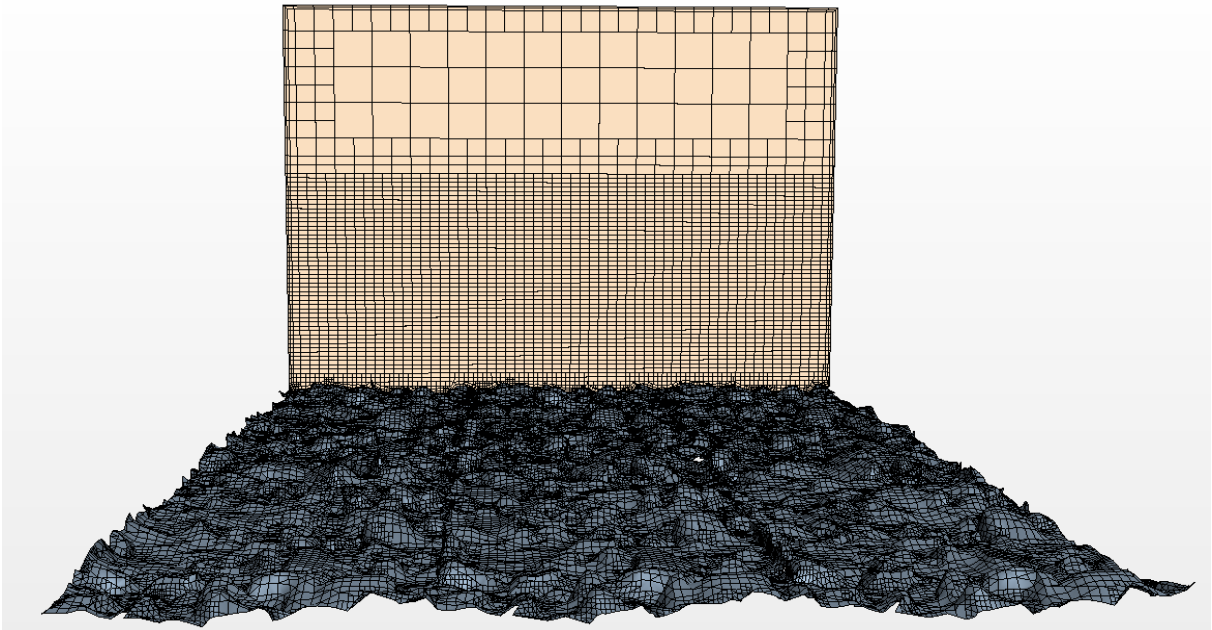


Figure 22: 5 mm transversal mesh

In Figure 23 and 24 the longitudinal and transversal grids along the channel for the fine mesh.

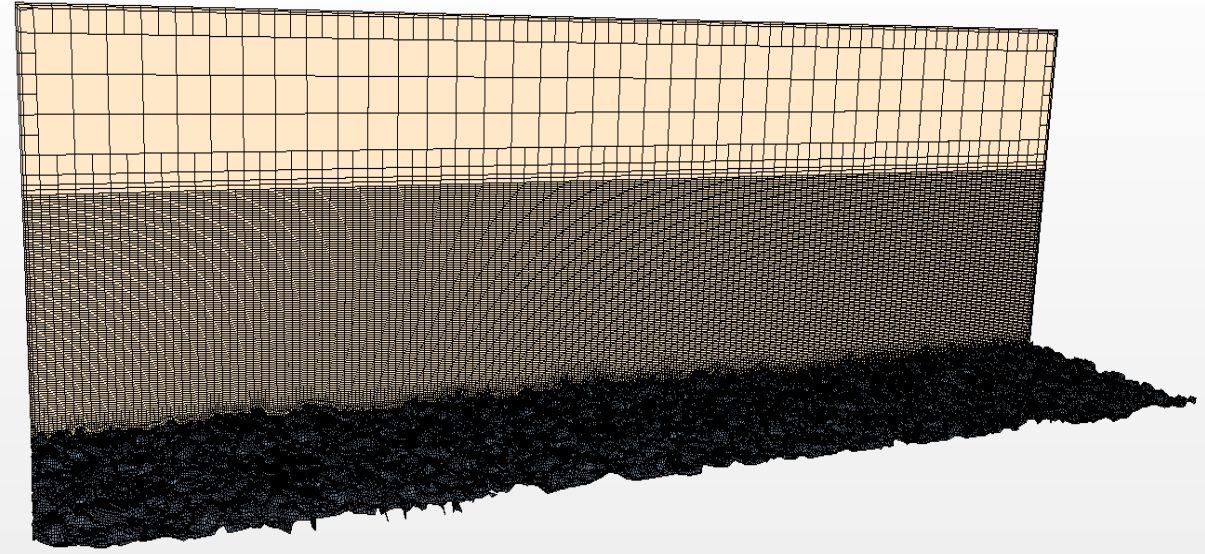


Figure 23: 3 mm longitudinal mesh

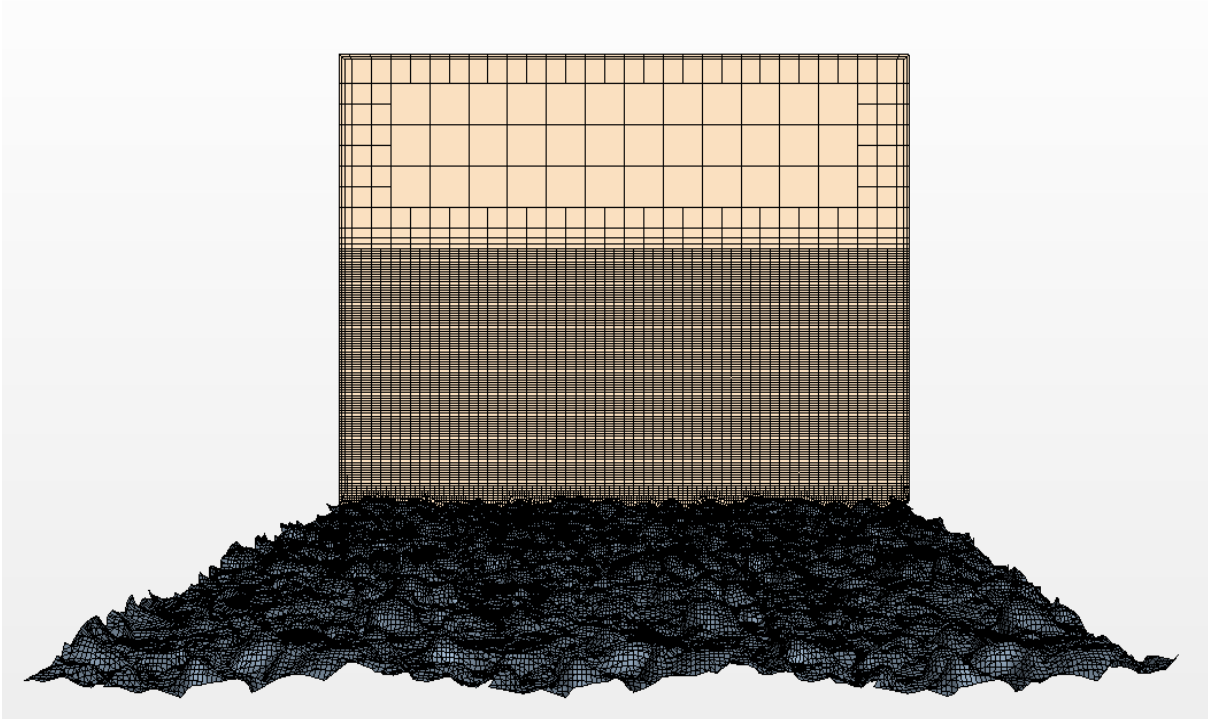


Figure 24: 3 mm transversal mesh

5.3 Physics models

STAR-CCM+ model solves RANS equations using the finite volume method, Table 6 sums up the physics models selected.

Table 6: Physics models

PHYSICS MODEL		DETAILS	
Space	Three dimensional	(x; y; z) coordinate system	
Time	Implicit unsteady time		
Gravity	g	9.81 m/s ²	
Multiphase Flow	Eulerian multiphase	Air	Ideal gas
		Water	Constant density
	Multiphase equation of state		
	Multiphase mixture		
Turbulence model	Reynolds-Averaged Navier-Stokes equations	Realizable k-epsilon two layer	2-nd order
	Spalart-Allmaras Turbulence	Standard Spalart-Allmaras	Convection 2 nd -order
Segregated flow	Segregated fluid isothermal	300.0 K	
Water surface treatment	Adaptive grid	VOF	
Wall laws	Two layer All-y ⁺		

As widely discussed, the Reynolds-Averaged Navier-Stokes equations in combination with the k-ε model has been solved since the wall effects are not so important.

The standard k-ε model has been chosen because it is widely used turbulence model that have shown good results in many cases for natural rivers and open channels, e.g. Fisher-Antz et al. (2008), Rütther et al. (2010). A second order upwind discretization has been set because it is known to give more accurate results than the first order scheme as in Rütther et al. (2010)

In order to compare simulation results using different turbulent models, the Spalart-Allmaras Turbulence model has been used. This model solves a single transport equation that determines the turbulent viscosity. This situation is in contrast to many of the early one-equation models that solve an equation for the transport of turbulent kinetic energy and required an algebraic prescription of a length scale. Between the three variants of the model available in STAR-CCM+, the Standard Spalart-Allmaras has been used.

5.3.1 Eulerian multiphase

As mentioned in section 3.6 an Eulerian Method has been used in order to consider multiple fluids coexisting in the flow domain: in this case air and water. In particular the Eulerian multiphase considers air and water as two phases not chemically related.

Phase means “thermodynamically state” of the matter solid, liquid or gas: multiphase flows are different from multi-component flows in which different species are mixed at molecular

level. In this study, air and water develop creating a separated flow which means there is a distinct line of contact (interface) between the two components.

Basically they can travel from one location to another in the same phase and remain in the same medium. For this reason the “Volume of Fluid” has been used as a modeling approach. As said in section 3.6.1, a single set of governing equation is solved for both phases using combined mixture properties.

The mixture properties are obtained by using the volume fraction of each phase. Regarding wall laws, as explained in section 3.5.1 the All- y^+ model has been used: it is hybrid that uses low- y^+ for fine meshes and high- y^+ for courser meshes. It is also formulated to produce more reasonable results for intermediate meshes.

5.4 Flow conditions

In order to complete the mathematical model created, conditions on the solution domain boundaries were specified. Conditions related to start time are called Initial conditions while Boundary conditions if related to space.

5.4.1 Initial conditions

Specifying initial conditions that are close to the expected solution can reduce the number of iterations required to reach a solution. The initial conditions may also be set similar to the inlet conditions of the fluid domain. Initial conditions are specified at a continuum level; if no initial conditions are specified, STAR-CCM+ will use default values to initialize the solution. The initial conditions specified are: velocity, pressure, turbulence and volume fraction.

Table 7: Initial conditions

Initial conditions		
VELOCITY	CONSTANT	(0.0, 0.0, 0.0) m/s
PRESSURE	CONSTANT	0.0 Pa
TURBULENCE INTENSITY	CONSTANT	0.01
TURBULENT VELOCITY SCALE	CONSTANT	1.0 m/s
TURBULENT VISCOSITY RATIO	CONSTANT	10.0
VOLUME FRACTION	WATER AIR	Outlet water fraction* Constant (0.0)

*function created by user in STAR-CCM+ code:

“Outlet water fraction”: ($\$Position [2] <= \$DownstreamStage? 1:0$) which means the volume fraction is 100% water below the Downstream Stage.

5.4.2 Boundary conditions

Almost every computational fluid dynamics problem is defined under the limits of boundary conditions. Boundary conditions tell STAR-CCM+ solvers how the flow within the region interacts with its environment. Within this modeling process the Inlet, Outlet and Wall Boundary conditions have been specified.

5.4.2.1 Velocity Inlet

There are three types of inlet boundaries available in STAR-CCM+ which differ depending on the properties used to define the inlet flow:

- Velocity;

- Mass flow rate;
- Stagnation inlet.

In this study, the velocity inlet has been used, in particular three field functions have been set. Field functions provide a mechanism by which fields (scalar or vector data that are evaluated at cells, vertices or boundary faces) can be viewed and defined in STAR-CCM+. Field functions can only be accessed on a part if the data used to define the field function exists on that part. The following table lists the field functions used at boundary inlet.

Table 8: Functions at inlet

Boundary conditions at inlet		
Velocity Magnitude	<i>Field Function</i>	Inlet Velocity*
Volume fraction	<i>Water</i>	Inlet Water Fraction**
	<i>Air</i>	Inlet Air Fraction***
Turbulence Intensity	<i>Constant</i>	0.01
Turbulent Viscosity Ratio	<i>Constant</i>	10.0

*, **, *** functions created by user in STAR-CCM+ code:

*Inlet Velocity: ($\$Position[2] \leq \$UpstreamStage?0.75:0$); below the upstream stage, velocity magnitude is 0.75 m/s.

**Inlet Water Fraction: ($\$Position[2] \leq \$UpstreamStage?1:0$); below the upstream stage, volume fraction is 100% water.

***Inlet Air Fraction: ($\$Position[2] > \$UpstreamStage?1:0$); above Upstream stage, volume fraction is 100% air.

5.4.2.2 Pressure Outlet

There are two types of outlet boundary available in STAR-CCM+, which differ depending on the desired flow properties at the outlet:

- Flow split;
- Pressure.

A pressure outlet boundary is a flow outlet boundary at which the pressure is somehow specified. Table 9 lists the field functions used at boundary outlet.

Table 9: Function at outlet

Boundary conditions at outlet		
Pressure	<i>Field Function</i>	Outlet Pressure*
Volume Fraction	<i>Water</i>	Outlet Water Fraction
	<i>Air</i>	Constant (0.0)
Turbulence Intensity	<i>Constant</i>	0.01
Turbulent Viscosity Ratio	<i>Constant</i>	10.0

*function created by user in STAR-CCM+ code:

($\$Position[2] \leq \$DownstreamStage?(\$DownstreamStage - \$Position[2]) * \$Densitywater * 9.81:0$) which means that below Downstream stage, the pressure is equal to Water Density per Gravity per the difference between Downstream stage and the position of the particle taken into account.

5.4.2.3 *Wall Boundaries*

A wall treatment in STAR-CCM+ is the set of near-wall modeling assumptions for each turbulence model. This term is different from the term wall functions, which refers to only one type of wall treatment. Three types of wall treatment are provided; as said in section 3.5.1 the all- y^+ wall treatment has been used. A wall function instead is the set of mathematical relations that are used to obtain the boundary conditions for the continuum equations whereby:

- A consistent set of assumptions is made regarding the distributions of velocity, turbulence, and other scalar quantities;
- It is assumed that the turbulence model is valid only outside the viscous-dominated region of the boundary layer, and the viscous-affected region of the boundary layer is not resolved;
- It is assumed that the centroid of the near-wall cell lies within the logarithmic region of the boundary layer.

The main advantage of using wall functions is the significant savings in terms of near-wall mesh resolution. In this study, the sides as well as the bottom are been treated as wall regions; for both, the Blend wall function is set with these characteristics:

- $E = 9.0$ (log law offset);
- $K = 0.42$ (Von Karmann constant);

This boundary condition appears only in turbulent flow on walls that do not have a slip condition on them. It is added to the values node when the all- y^+ wall treatment is selected.

5.5 Hydraulic conditions

As said in section 4.3.1 the experiment carried out by Spiller et al. (2013) was divided into a number of 18 runs, setting the pump frequency to 5 Hz, a water discharge of 6 l/s evolved. Table 10 shows all 18 runs, each with its discharge and flow depth. In order to compare the results of this CFD simulation as well as for a good validation of the model used, five different situations have been considered as shown in Table 10.

Table 10: Hydraulic conditions

RUN	WATER DISCHARGE	WATER DEPTH
N°	Q (l/s)	d (mm)
1	6	134
2	21	151
3	42	171
4	63	191
5	90	207

First, two user field functions, called “Upstream stage” and “Downstream stage”, have been set at the water depth value corresponding to the considered discharge. That means the flow breaks out with a flat water surface, then evolves in according to the flow and boundary conditions. Should be clear that at the beginning, the “Downstream stage” dominates the flow evolution. Afterwards a new user field function, named “Inlet Velocity” have been added in this code:

$(\$Position[2] \leq \$UpstreamStage ? 0.42 : 0)$ which means for example, as said in section 5.4.2.1, that below the “Upstream stage” the velocity is 0.42 m/s for 42 l/s water discharge

while ($U_{Position[2]} \leq U_{UpstreamStage} \cdot 0.75$) means the velocity is 0.75 m/s for 90 l/s water discharge.

Considering the water depth (“Upstream stage”) and the inlet region area, a water discharge of 42 l/s in the third case and 90 l/s in the last one, evolve into the system reproducing the experimental flow conditions perfectly.

5.6 Solvers

In STAR-CCM+, solvers control the solution and are activated once per iteration (or once per time-step for explicit unsteady simulations). Typically, a model elects the solvers that are required; different models can use the same solver and sometimes models need more than one solver. Some models control other models and some only perform tasks when the solution is initialized. For this reason, not all models elect solvers. Models can also elect solvers that perform subsidiary tasks in addition to the solver that the model elected to control it. In Table 11 are listed the solvers used within this CFD simulation.

Table 11: Solvers

SOLVERS		
Implicit Unsteady	Time-step	0.0010 sec
	Temporal discretization	1 st-order
Partitioning	Partitioning method	Per region
Wall distance	Verbosity	0
	Parallel memory optimization scaling factor	1.0
Segregated flow:	Continuity initialization iterations	3
Velocity and Pressure (Under-Relaxation Factor: 0.8)	Continuity initialization tolerance	1.0E-6
Segregated VOF	Under-Relaxation Factor	0.9
Segregated Energy	Fluid Under-Relaxation Factor	0.9
	Solid Under-Relaxation Factor	0.99
k-ε turbulence (AMG linear solver)	Under-Relaxation Factor	0.8
k-ε turbulent viscosity	Under-Relaxation Factor	1.0
	Maximum Ratio	100000.0

The Implicit Unsteady solver becomes active when the Implicit Unsteady model is active. Its primary function is to control the update at each physical time for the calculation; it also controls the time-step size. The partitioning solver is responsible for controlling domain decomposition (or partitioning) for parallel simulations. Before any physics solvers are invoked on a given global iteration or time-step, the partitioning solver is first invoked to ensure that the domain decomposition is up-to-date. The wall distance solver controls the wall distance computation for all continua in which wall distance is calculated. The segregated flow solver controls the solution update for the segregated flow model according to the simple algorithm. It controls two additional solvers:

- Velocity solver;
- Pressure solver.

The segregated VOF solver controls the solution update for the phase volume fractions. More specifically, it solves the discretized volume-fraction conservative equation for each phase present in the flow. The Energy solver controls the solution update for the segregated fluid Energy model while the k-ε turbulence solver controls the solution of the k-ε model in all the

continua for which the model is activated. Lastly, the k-ε turbulent viscosity solver controls the update of the turbulent viscosity.

5.7 Stopping criteria

Stopping criteria allow to specify how long the solution runs for and under what conditions it stops iterating and/or marching in time. Each specified stopping criterion is evaluated at the completion of every simulation step and a logical rule is used to determine if the interaction of all of the criteria stops the solver. Table 12 lists the stopping criteria used.

Table 12: Stopping criteria

STOPPING CRITERIA
Maximum inner iteration
Maximum physical time
Maximum steps
Stop file

The maximum inner iteration stopping criterion is based on the number of inner iteration that the solver executes for transient analysis.

The node of this criterion has its own properties and appears when the implicit unsteady model is chosen. Further, if the implicit unsteady solver is used, this criterion can control the number of inner iterations to be run at each physical time-step.

The maximum physical time stopping criterion is linked to the time-step property of the implicit unsteady node in the solvers node.

If the time-step is set to 1 second, and the maximum physical time to 10 seconds, then the simulation runs for 10 time-steps.

In this simulation the maximum physical time is set to 1440.0 seconds while the maximum steps at 100.000 because it has been preferred to monitor the running day by day and stop it in different situations.

The mass flow convergence has been considered as the main stopping criterion over the different criteria set.

5.8 Post-processing

Once the simulation was done as well as all the stopping criteria satisfied, the first step was to verify the model. In order to do this a mass flow plot was created setting the inlet face and outlet face as the two regions between which the mass flow continuity was checked.

A mass flow monitoring on top region was carried out as well, to take into account any water leaks.

Even for validation, the residuals plot was considered ensuring all the parameters falling down a chosen value with a steady trend. In order to compare the simulation results with the experimental data, the zero point was located near the bottom considering the roughness tops matching at 13.3 mm. Afterwards, in the same area of PIV measurements, a longitudinal grid was located highlighting the velocity profile along it.

That results were averaged along flow direction, analyzed and matched with the experimental data of Spiller et al. (2013) through a dimensional and non-dimensional velocity plot.

A pressure plot along flow direction from the water surface until the bottom was pointed out and compared with the theoretical one:

$$P = \rho gh$$

The following table lists the scalar and vector scenes as well as all the plots created during post-processing.

Table 13: Scalar/vector scenes and plot

SCENES	PLOTS
Zero point location	Residuals plot
PIV area	Mass flow balance
Longitudinal and transversal grid along the channel	Longitudinal and transversal velocity profile
Longitudinal and transversal grid within PIV area	Dimensional velocity matching
Longitudinal velocity profile (magnitude)	Non dimensional velocity matching
Transversal velocity profile (magnitude)	Pressure matching
Longitudinal vector velocity profile	Line-probe velocity profile
Longitudinal velocity profile within PIV area	
Transversal velocity profile within PIV area	
Water level	
Volume fraction of water on outlet and inlet	
Volume of fluid (VOF)	
VOF velocity	

6 COMPARISON OF THE RESULTS

In this chapter the main results of the simulations are shown. First of all, the PIV area of measurements was located inside the geometry and considered for the analysis. In this area, a grid was set along flow direction and considered as the cross-section for velocity profile. The velocity profile of all the discharges simulated with 3 mm or/and 5 mm mesh size was compared to the experimental data. The 21 l/s discharge was simulated considering first the Reynolds-Averaged Navier-Stokes equations and then the Spalart-Allmaras as Turbulence model. Once the velocity matching offered good results, further analysis on static pressure and wall shear stress were carried out.

6.1 Preliminary work

6.1.1 Area of analysis

Since in the experiment of Spiller et al. (2013) the field of view measures 282 mm in x-direction, meaning along the central streamline and 61 mm in the vertically oriented z-direction, a grid of 20x20 points along x-direction was set. This longitudinal grid with dimension 300x60 mm was located between 0.9 and 1.2 values along x-direction and right in the middle of the channel (30 cm from left/right side).

Figure 25 the area of PIV measurements chosen in the experiment of Spiller et al. (2013) and the related area inside the geometry created within STAR-CCM+.

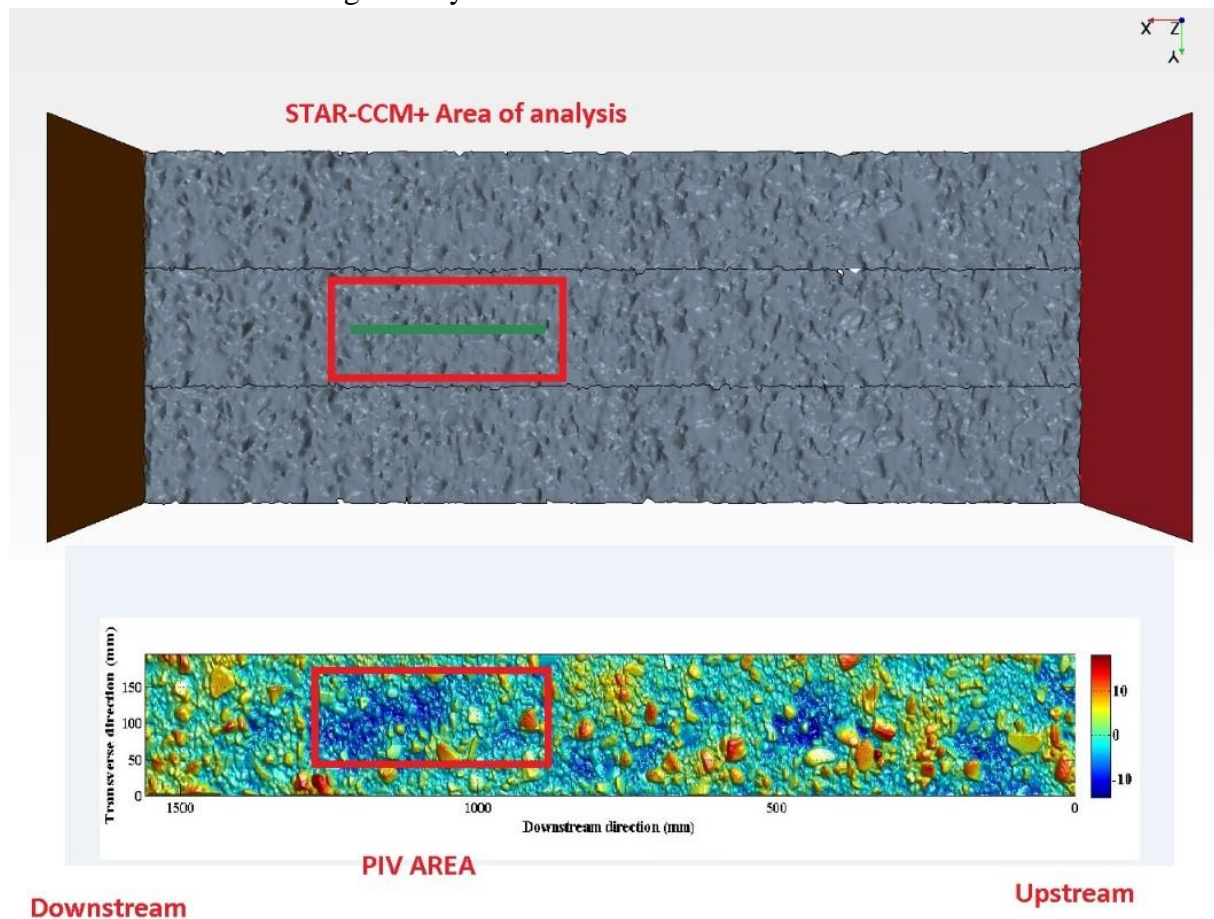


Figure 25: Area of analysis

6.1.2 Location of zero point

Once the PIV area was located inside the geometry, the next step was to set the zero point along z-direction in order to properly match the velocity profile coming from the simulation with the experiment one. The elevation of roughness tops was considered the main parameter for a perfect matching. Looking at the following image, as in the model as in the experiment, the roughness tops are matched at 13.3 mm from bottom.

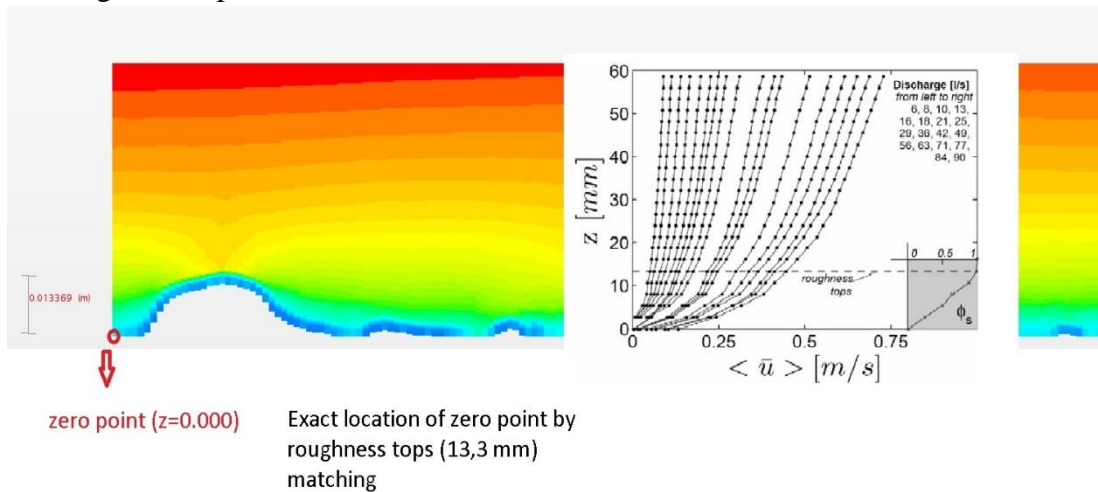


Figure 26: Location of zero point

6.1.3 Double averaged velocity profile

The results of the experiment by Spiller et al. (2013) are shown in form of double averaged streamwise velocity profile $\langle \bar{u} \rangle$ for each run. As mentioned in section 5.5, five discharges were chosen and averaged first on time \bar{u} and then on space $\langle u \rangle$, in particular, on a longitudinal grid of 20x20 points along flow direction. Considering the elevation of the grid (60 mm), the simulations give back 20 velocity values every 3 mm, properly averaged, resulting a double averaged velocity profile as detailed as the experiment done. In Figure 27 the velocity profile on grid for the particular case of 42 l/s water discharge.

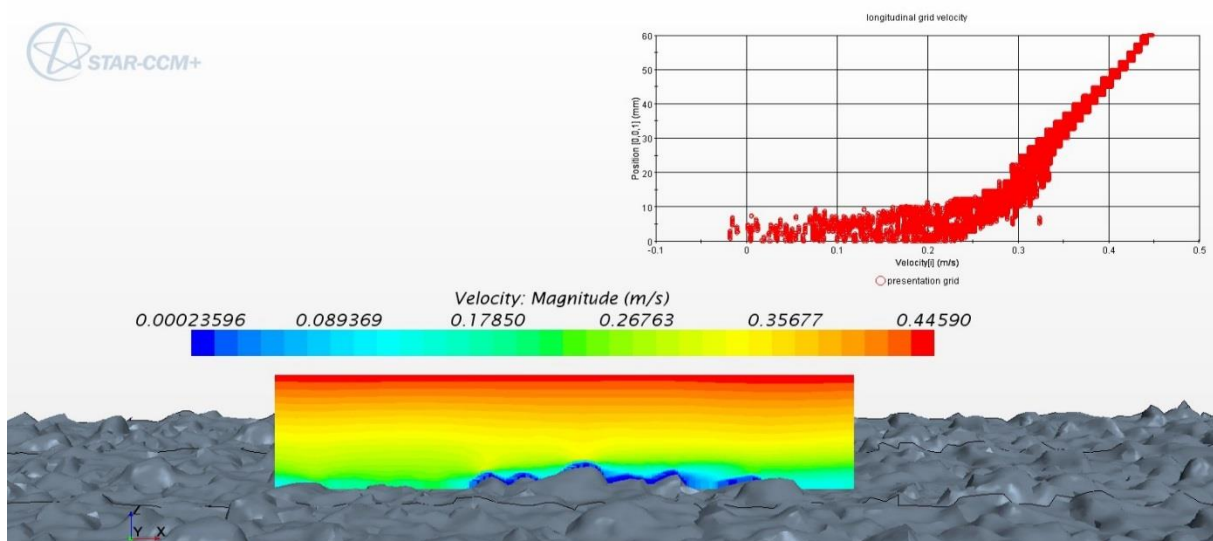


Figure 27: Velocity on longitudinal grid

6.2 Stopping criteria

6.2.1 Supercomputer

Since the simulations are demanding in computer power, the hardware available becomes important. In the first part of this project, a system offered by the Department of Hydraulic and Environmental Engineering of NTNU was used mainly to get familiar with STAR-CCM+ code. Afterwards, considering the mesh size and the number of cells constituting the model, a supercomputer named “Vilje” was used for all the simulations.

The Norwegian University of Science and Technology in Trondheim operates the “Vilje-supercomputer”, owned by NTNU and the Norwegian Meteorological Institute. “Vilje” is operating at 275 teraflops and is ranked 8th among supercomputers in Europe.



Thanks to its high performances, it has been possible to run several simulations in the same time and getting the results in few days.

Figure 28: Vilje supercomputer

6.2.2 Mass flow

Working on a supercomputer throughout an interface, it was necessary to set an autosave mode in order to have the simulation back once it was done. In this case, besides a logical rule or number of iterations, as a stopping criteria, the mass flow balance and the residuals trend was taken into account. In Figure 29 the typical trend of mass flow between inlet and outlet is shown for the particular case of 90 l/s water discharge.

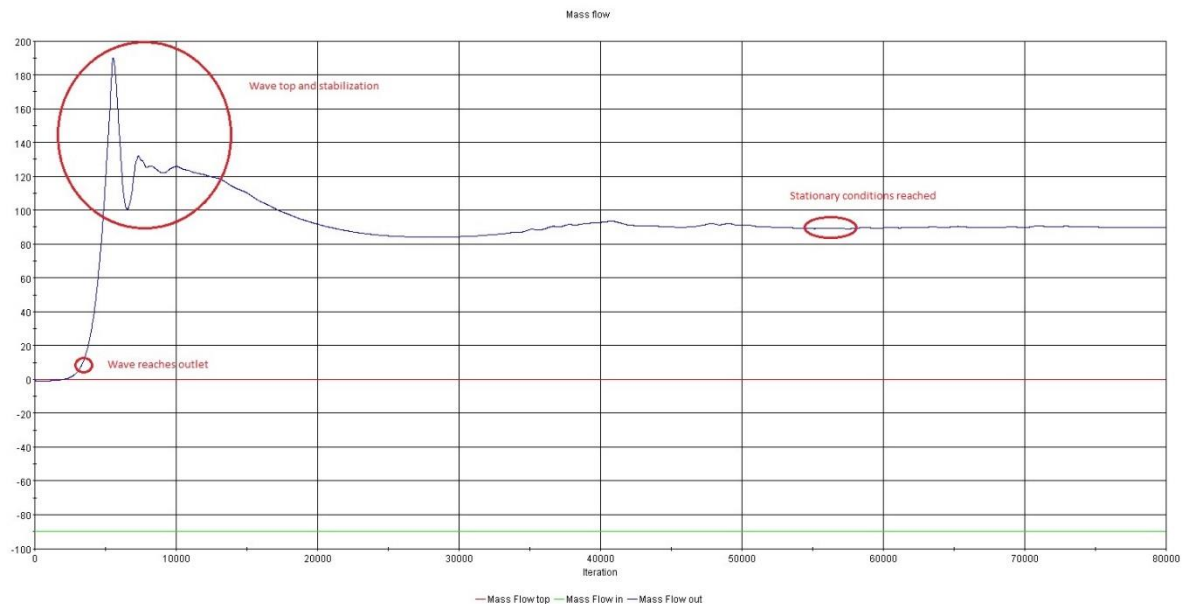


Figure 29: Mass flow balance

The initial negative outflow is caused by the pressure boundary condition at the outlet. It is possible to distinguish when the wave reaches the outlet, the wave top with stabilization zone and finally when the stationary conditions are reached. The difference between mass flow in and mass flow out less than 2% has been considered as the final stopping criterion.

6.2.3 Residuals

In order to definitely stop the simulation, the residuals trend has been analyzed assuring all the parameters falling down a chosen value with a constant trend for more than 20.000 iterations. In Figure 30 the residuals plot relating to 42 l/s water discharge is shown: in this case all the parameters show a constant trend below the value 1.

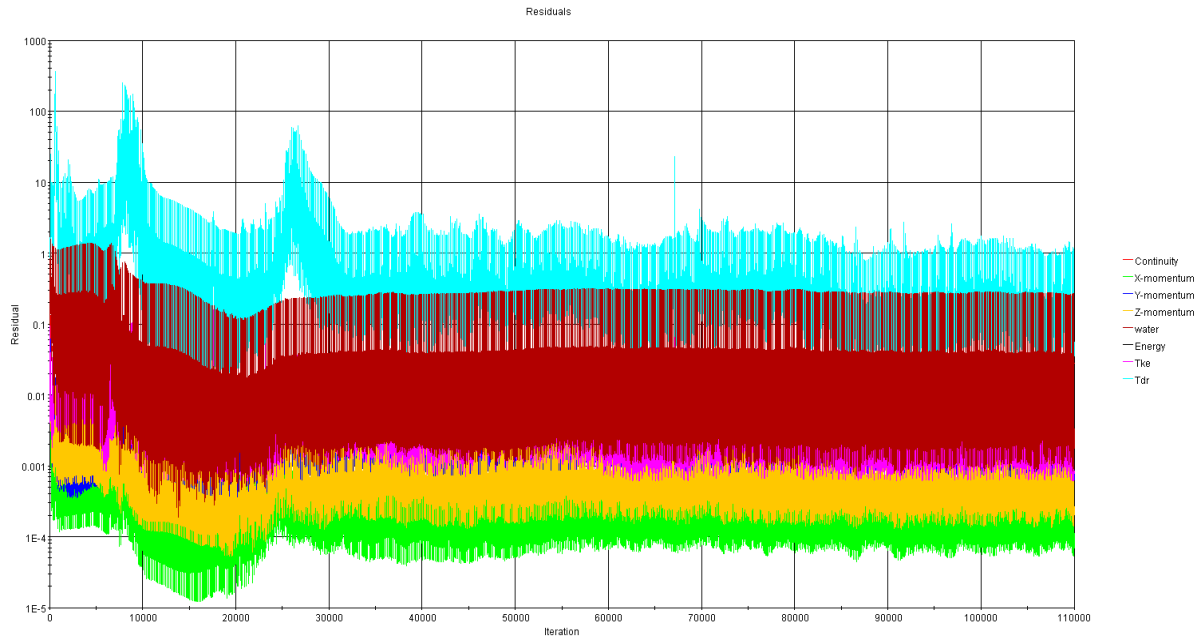


Figure 30: Residuals plot

6.2.4 Reynolds and Froude numbers

As widely explained, the instability of flow may be expressed in terms of Reynolds number (Re) here again: $Re = \frac{\rho LU}{\mu}$; where: ρ is the fluid density (997,561 kg/m³), μ is the dynamic viscosity (8,88*10⁻⁴ Pa*s), L and U are characteristic length and speed for the flow. The Froude number is a dimensionless parameter used in connection with open channel flow. For flow in a rectangular channel, the Froude number is defined as : $Fr = \frac{v}{\sqrt{g*y}}$ where: y is the flow depth above the channel bottom, g is the gravity acceleration (9,81 m/s²), v the average flow velocity. For:

Fr < 1 flow is subcritical;

Fr = 1 flow is critical;

Fr > 1 flow is supercritical;

This gives a set of criteria for determining whether a given flow is subcritical, critical, or supercritical. Table 14 shows both these number for each discharge simulated.

Table 14: Reynolds and Froude numbers

Discharge	y (m)	U/v (m/s)	Re	Fr
6 l/s	0,134	0,07	10537	0,061
21 l/s	0,151	0,24	40711	0,197
42 l/s	0,171	0,43	82602	0,332
63 l/s	0,191	0,54	115865	0,395
90 l/s	0,207	0,75	174405	0,53

As already said in paragraph 2.2, a Reynolds number well above 1000 is probably turbulent while considering Froude number, each case can be considered as a subcritical flow.

6.3 Water level

In the experiment of Spiller et al. (2013), the downstream part of the flume was rather unique. Instead of a common weir at right angles with the flow direction, two separate weirs, one on each side of the flume, were overflowed to discharge the water. The weirs were fixed at a constant height of 20 cm. As a result of that particular geometry, the water level was quite constant during the PIV measurements. In order to re-create the same Hydrology conditions in the model, as said, an outlet pressure function was set to keep the water surface as stable as possible. The following figure shows the 3D volume of fluid developing into the model.

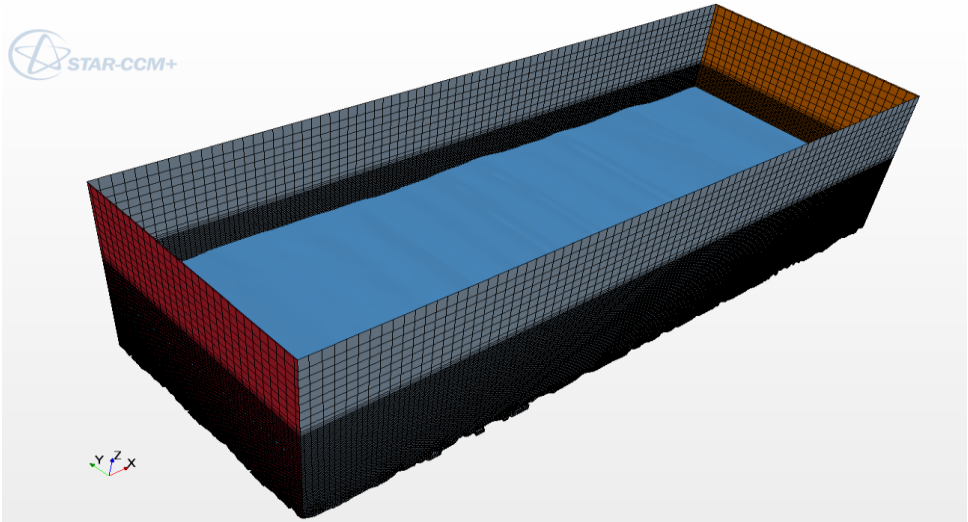


Figure 31: 3D geometry model

To check the stability of water level, different scalar were created as follow. Figure 32 shows the volume fraction of water on outlet in the particular case of 42 l/s water discharge.

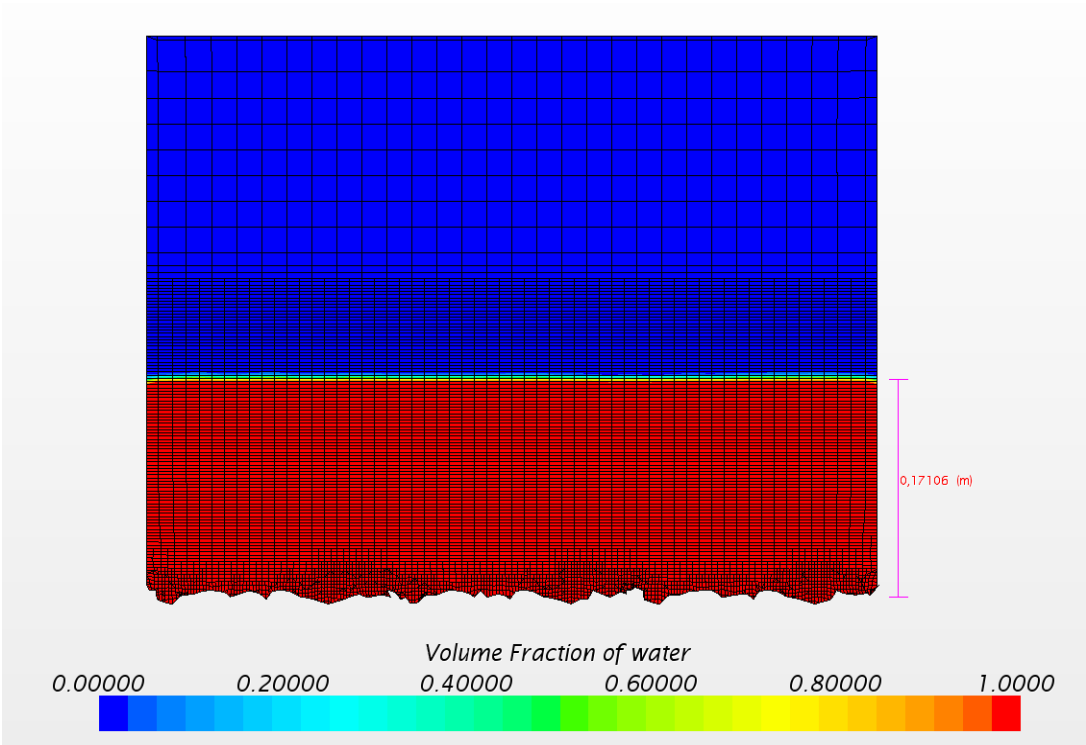


Figure 32: Volume fraction of water at outlet

It's possible to look at the elevation of water surface, completely acceptable considering that, for 42 l/s water discharge, the inflow water depth was 171 mm. Figure 33 shows the water level position along the whole channel: for 42 l/s discharge, the water level fluctuations are less than 2 cm.

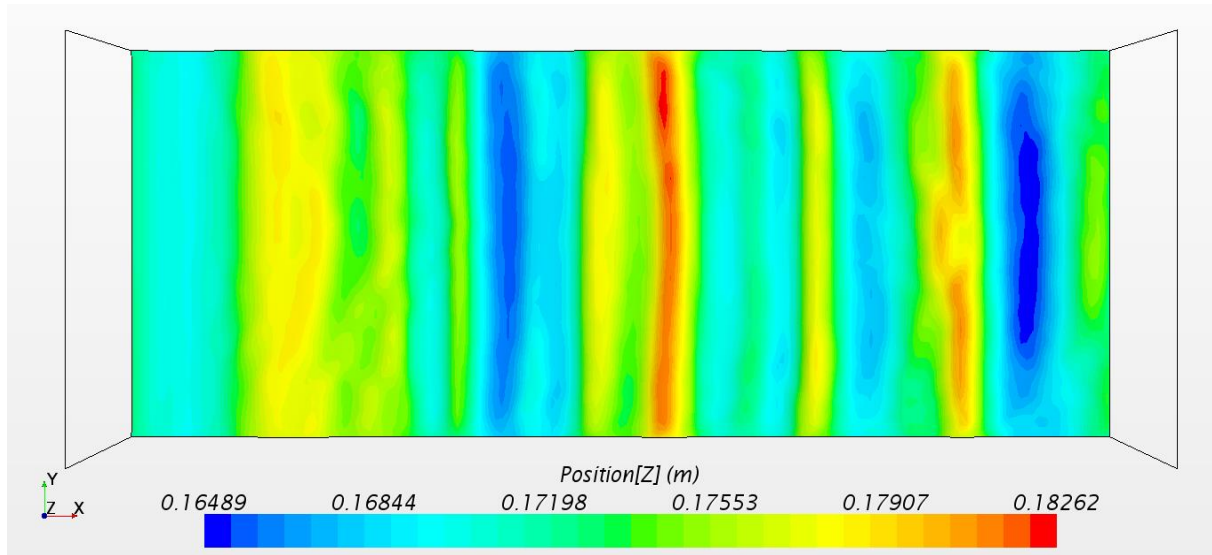


Figure 33: Water level

6.4 Pressure

As mentioned in section 5.8, the pressure was analyzed along the channel creating a matching plot with the theoretical pressure: $P = \rho gh$. The following figures present the pressure plot for five discharges simulated. The values were taken on a line-probe right in the middle of the channel. Looking at these figures, a perfect matching is obtained and this can be considered as a further confirmation about the validity of the model.

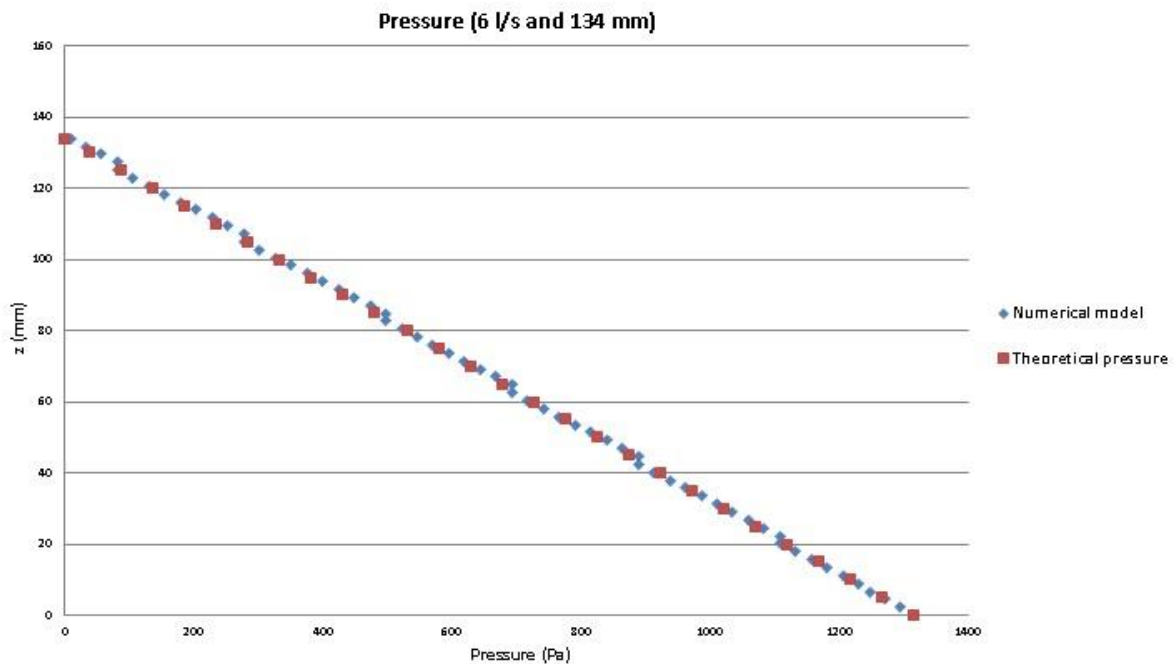


Figure 34: Pressure values for 6 l/s

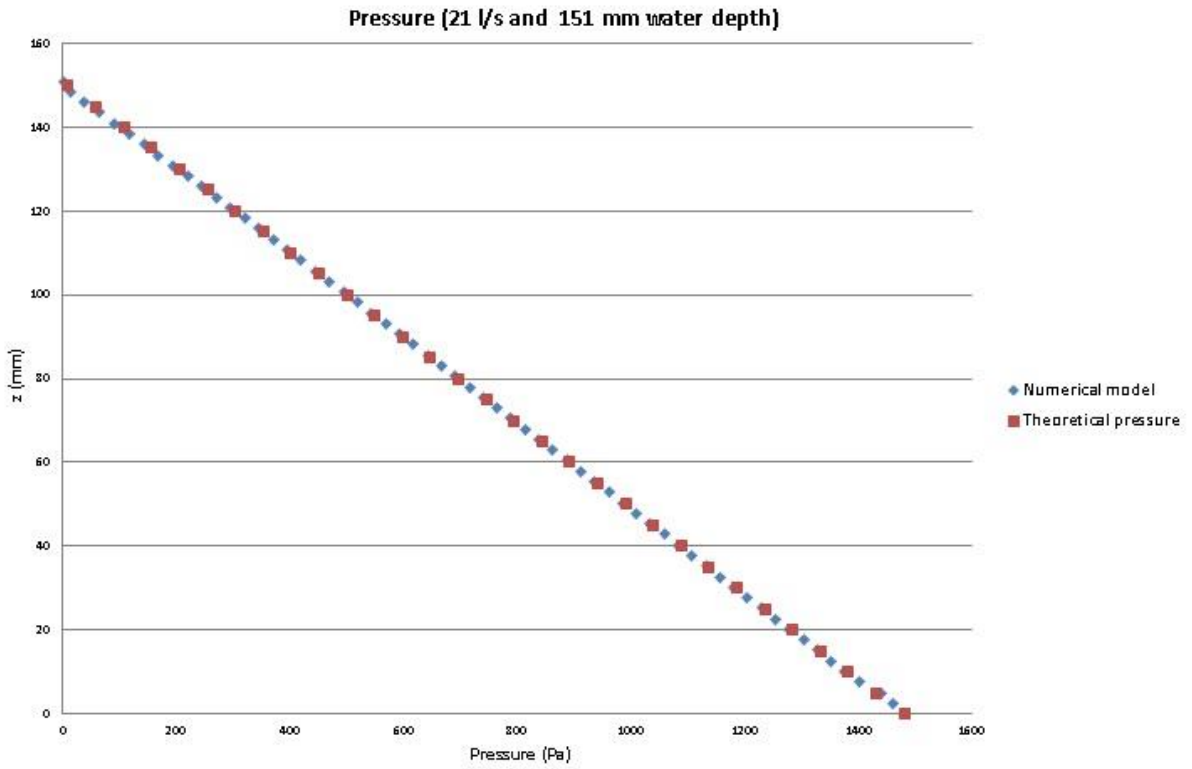


Figure 35: Pressure values for 21 l/s

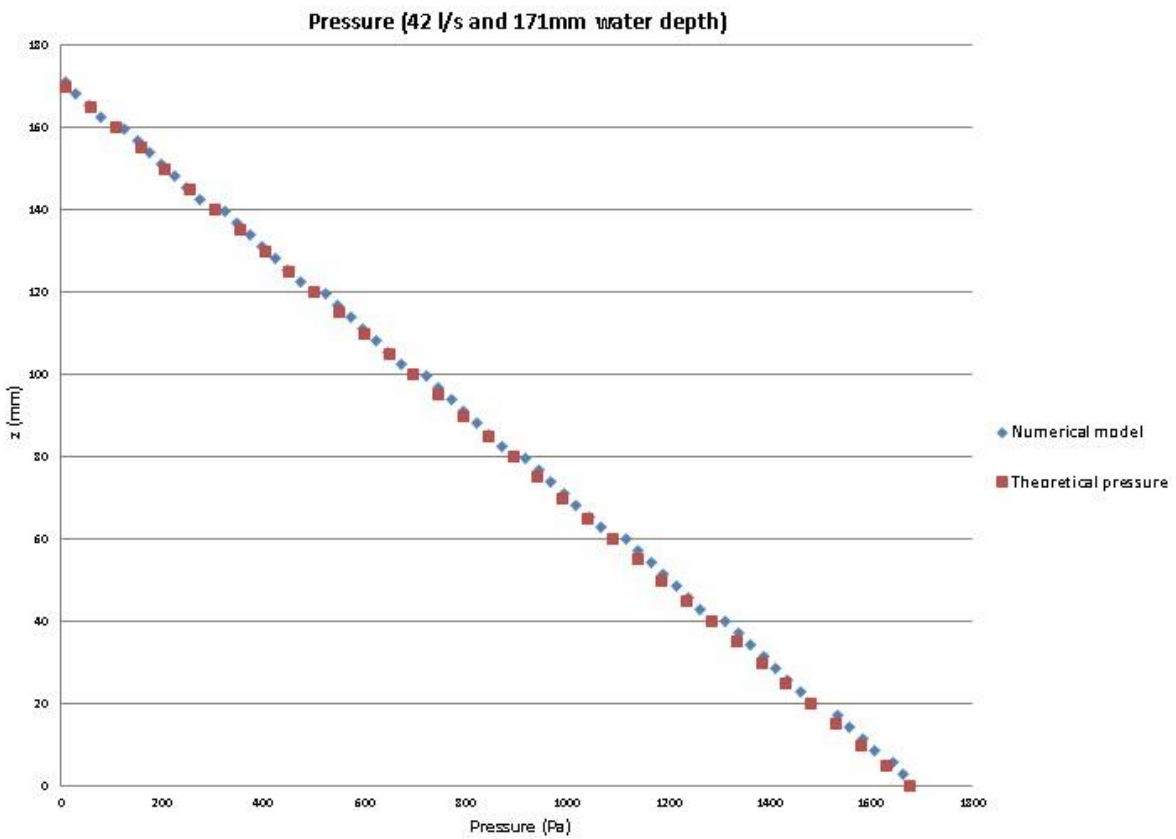


Figure 36: Pressure values for 42 l/s

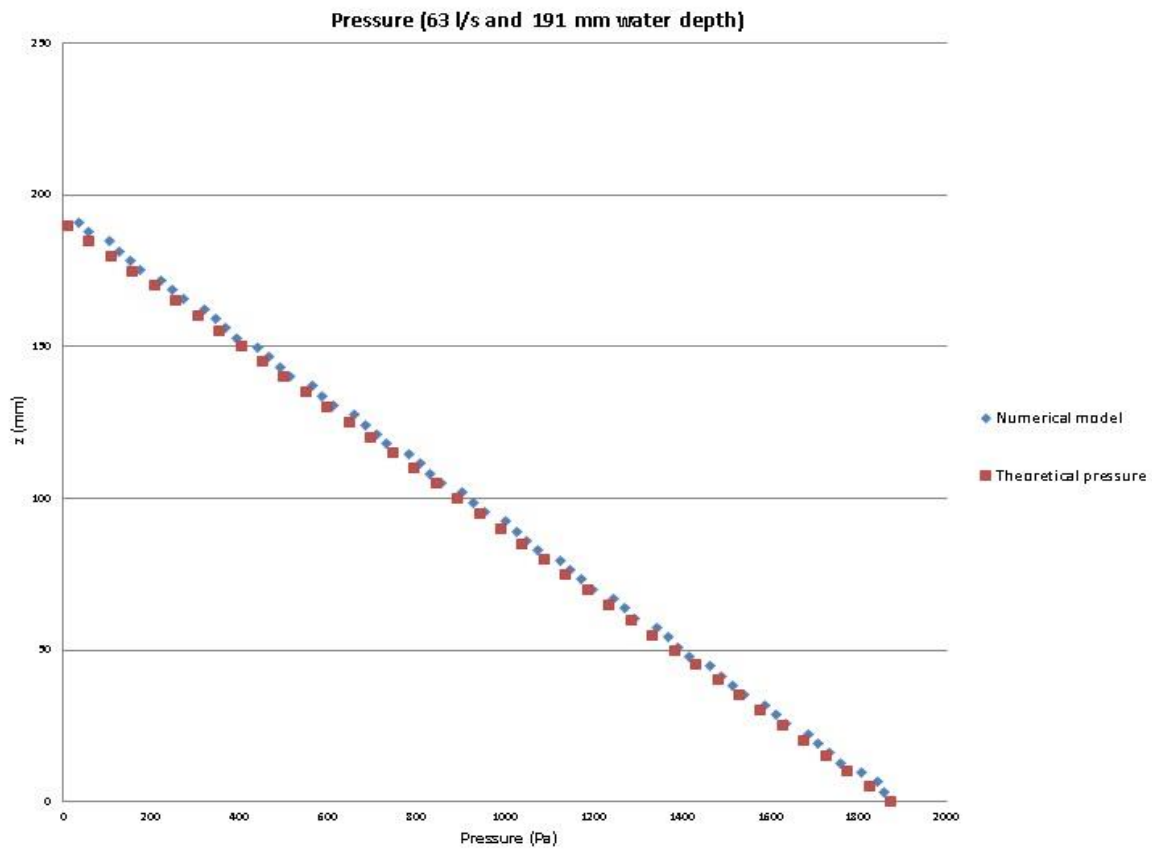


Figure 37: Pressure values for 63 l/s

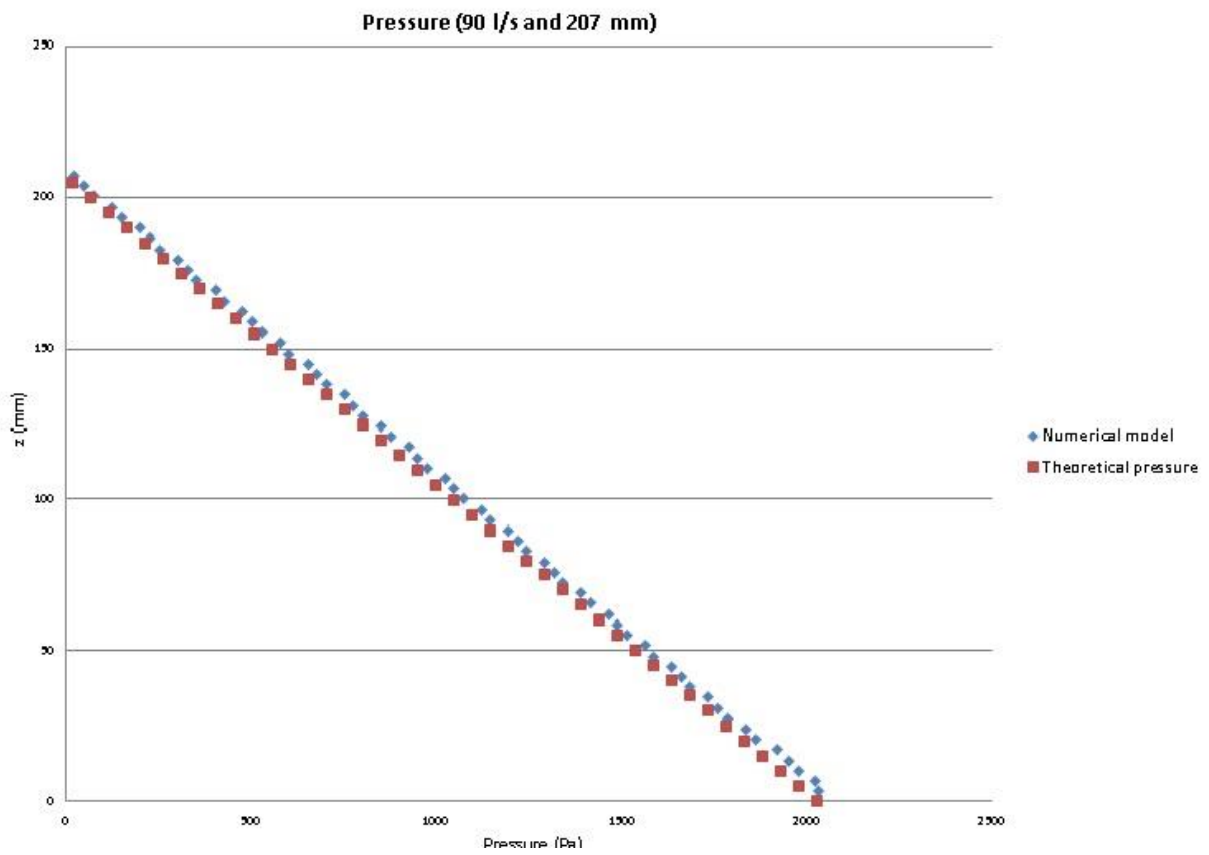


Figure 38: Pressure values for 90 l/s

6.5 Wall shear stress

Roughness effects as well as wall shear stress (skin friction) and near-wall turbulence, result from surface imperfections too small for the mesh to resolve, but which still affect the flow. The wall shear stress τ_w , is given by:

$$\tau = \mu \left(\frac{\partial u}{\partial z} \right)$$

Where μ is the dynamic viscosity, u is the flow velocity parallel to the wall and z is the distance to the wall. The SI unit of wall shear stress is an essential flow parameter to evaluate the corrosion rate and as it is expected, it increases with flow velocity or, which is the same, with the Reynolds number. In the following images, wall shear stress near the bottom is shown for the five cases analyzed. The same color bar and scalar field were used for all the discharges in order to show how shear stress magnitude increases passing from 6 l/s until 90 l/s water discharge.

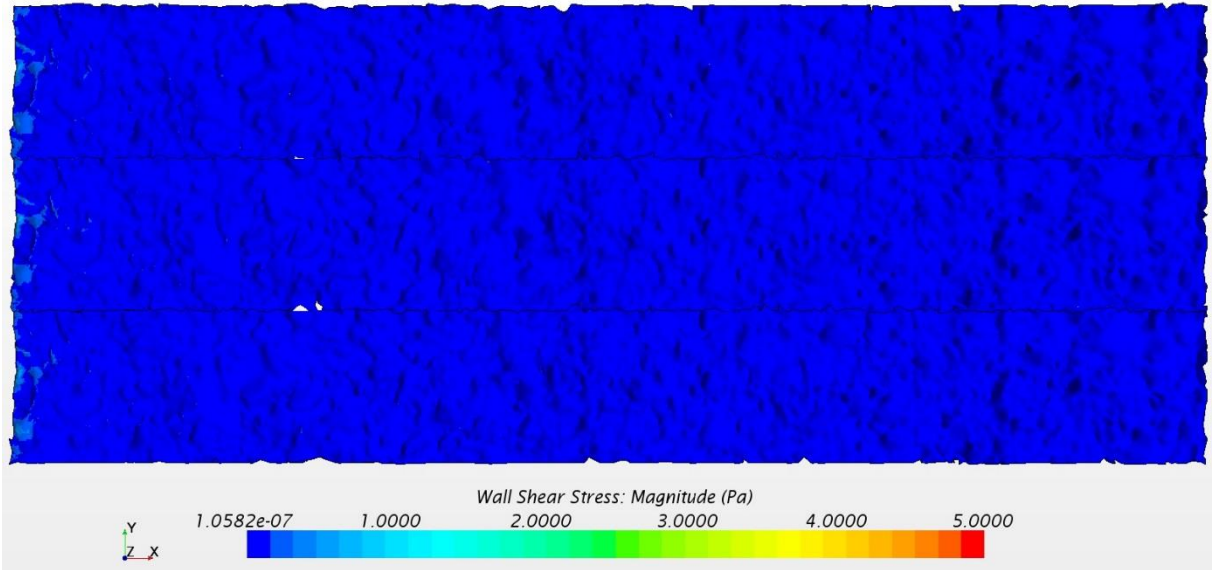


Figure 39: Wall shear stress for 6 l/s

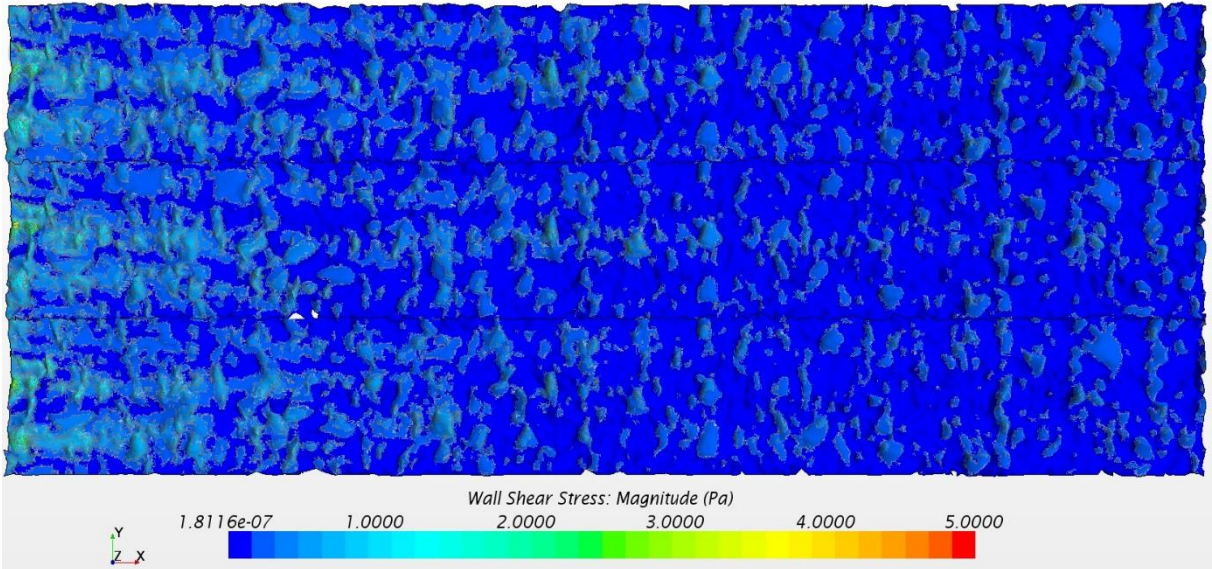


Figure 40: Wall shear stress for 21 l/s

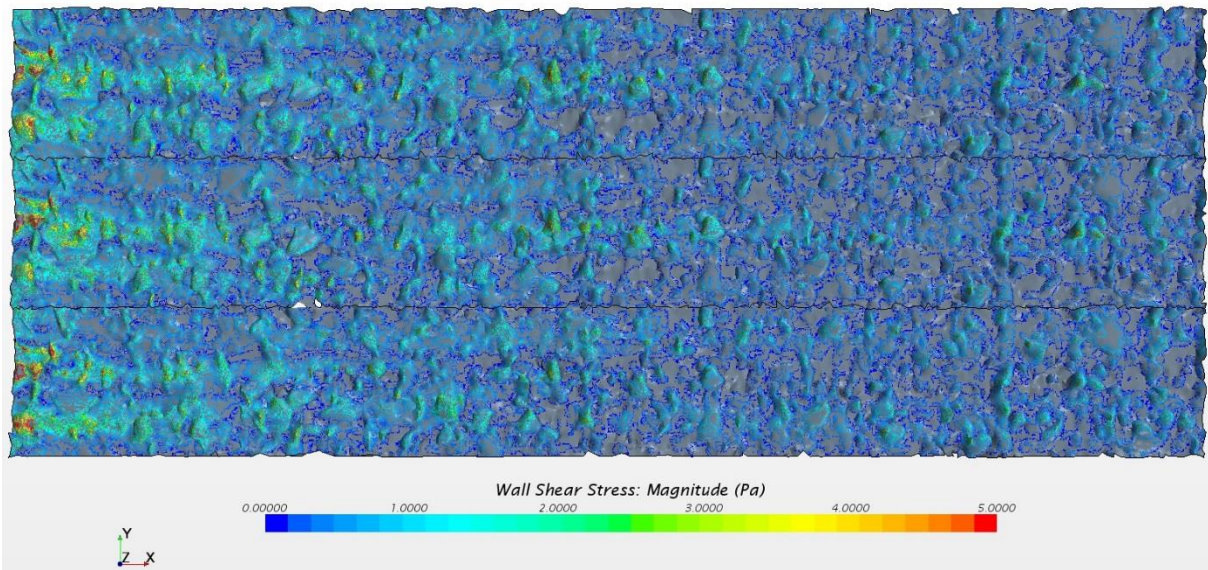


Figure 41: Wall shear stress for 42 l/s

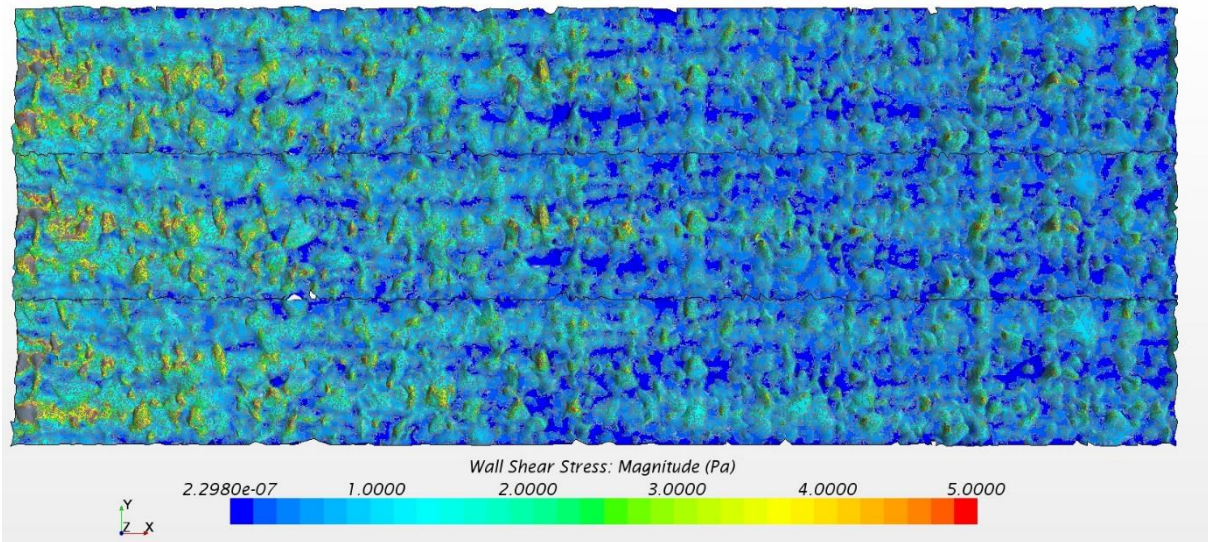


Figure 42: Wall shear stress for 63 l/s

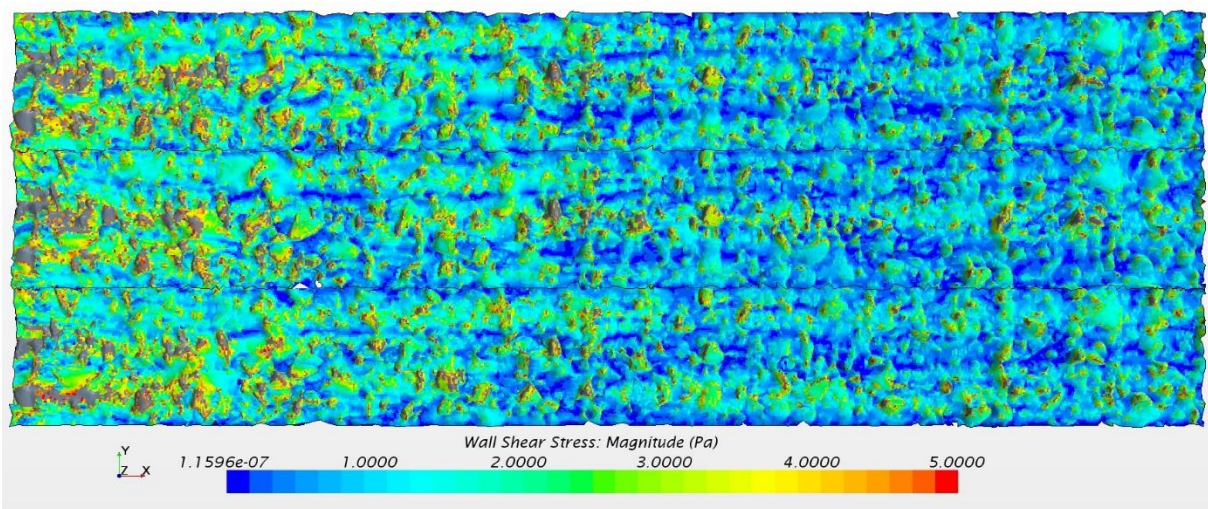


Figure 43: Wall shear stress for 90 l/s

6.6 Velocity scenes

Among five discharges simulated, one was chosen to show some particular velocity scenes to better understand the evolution of the flow inside the model.

6.6.1 Scalar velocity scenes

For a 3D vision, in Figure 44 velocity magnitude on a section plan as long as the channel, located at 30 cm from left/right side and flow direction from left to right; in Figure 45 velocity magnitude along a section plan as wide as the channel, located at 0.9 m from inlet.

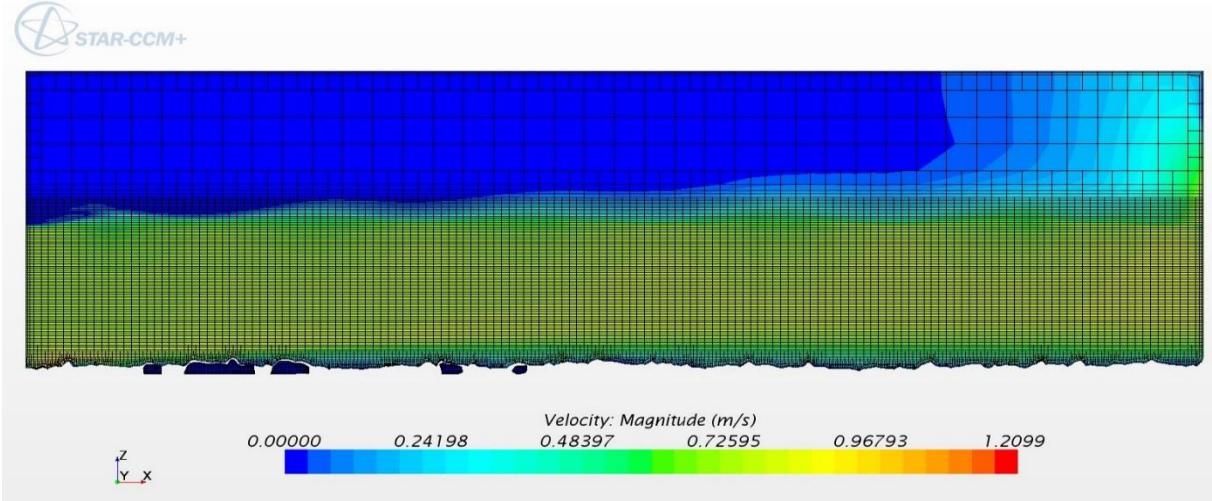


Figure 44: Longitudinal velocity magnitude

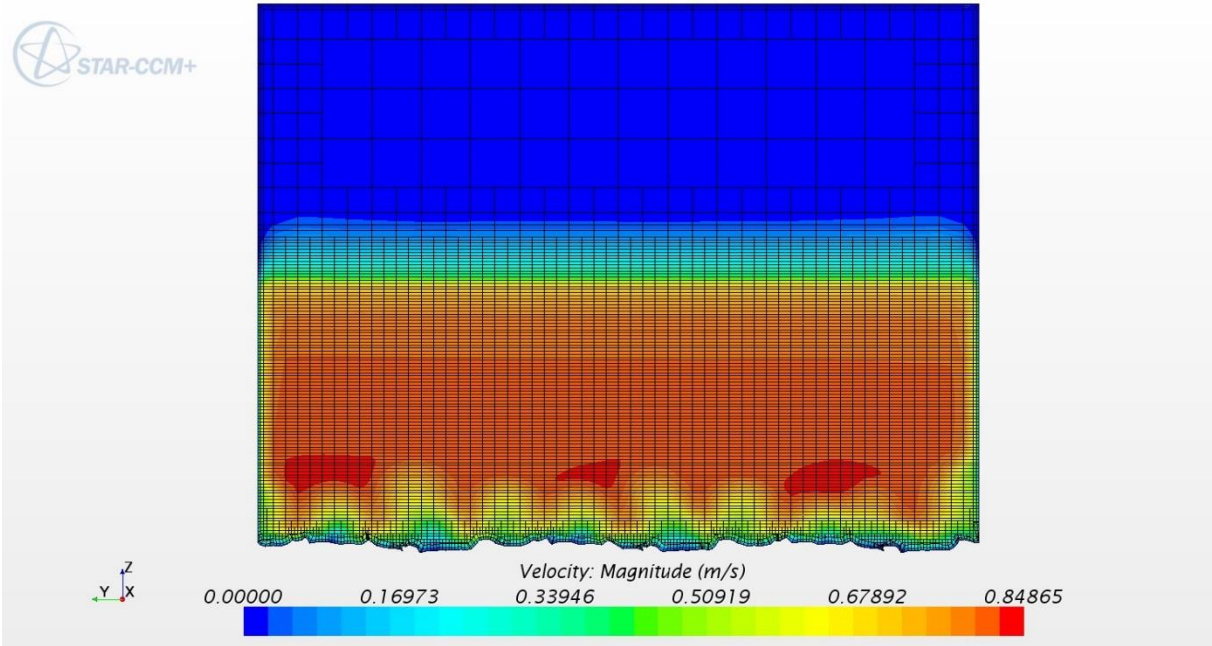


Figure 45: Transversal velocity magnitude

For better understand the results of the simulations, same velocity scenes were pointing out in the area of analysis, as shown in the following figures.

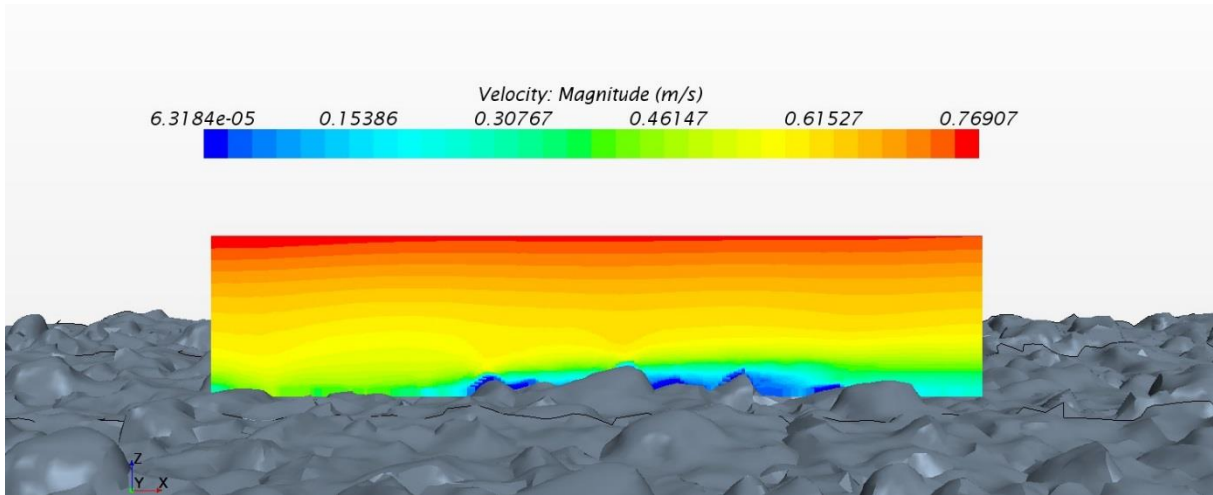


Figure 46: Velocity on longitudinal grid

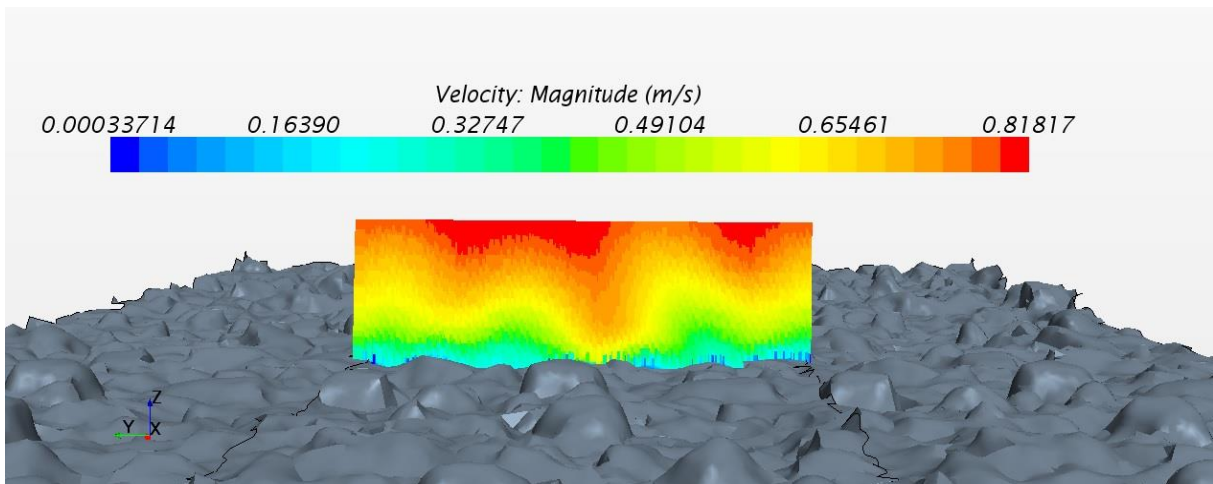


Figure 47: Velocity on transversal grid

6.6.2 Vector velocity scenes

Vector velocity scenes have been useful to analyze the flow direction, in particular on outlet, to properly set the pressure functions. In Figure 48 vector velocity along flow direction.

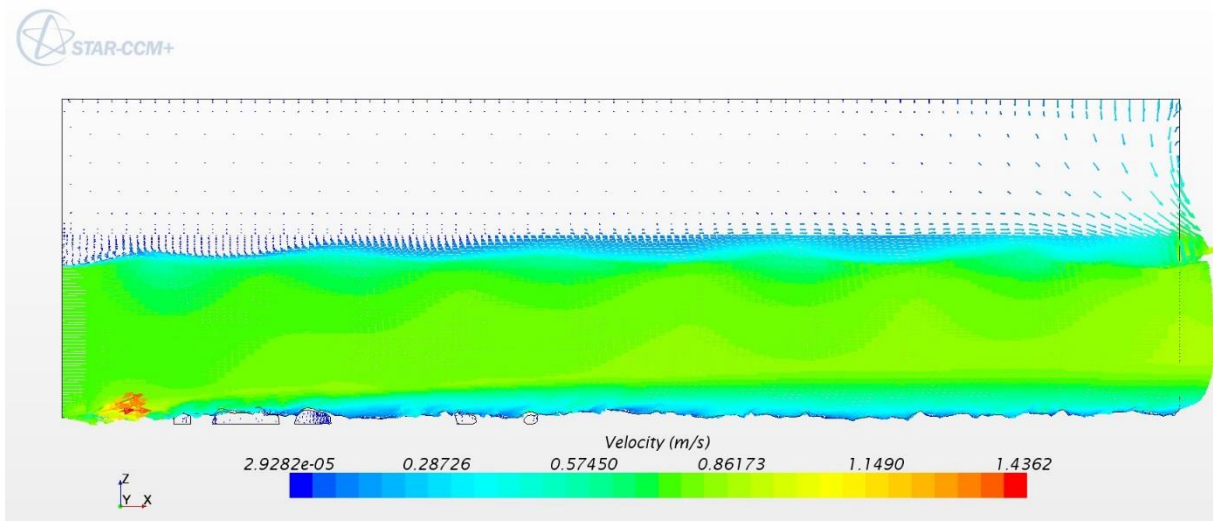


Figure 48: Vector velocity

Vector velocity is shown on water surface in Figure 49.

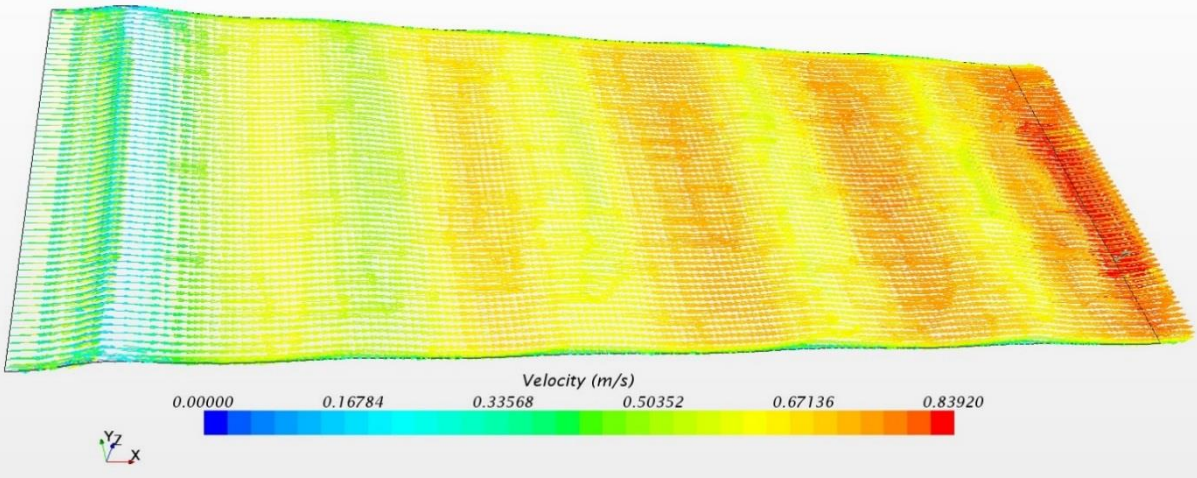


Figure 49: Vector velocity on VOF

Looking at the figures above, water level is quite stable along the channel. Further, the separation line between air and water is clearly visible in Figure 49. Both images highlight an averaged velocity value around 0.75 m/s or less for 90 l/s water discharge, with low values near the inlet and high values at outlet.

6.7 Mesh comparison

As said, two different mesh sizes were used during this study (3 mm and 5 mm) as well as the first one represents the best solution considering how detailed are the results coming from the experiment by Spiller et al. (2013) In Figure 50 is presented a comparison between the two mesh sizes used for velocity profile relating to 42 l/s in 60 mm from bottom, while in Figure 50 relating to 90 l/s.

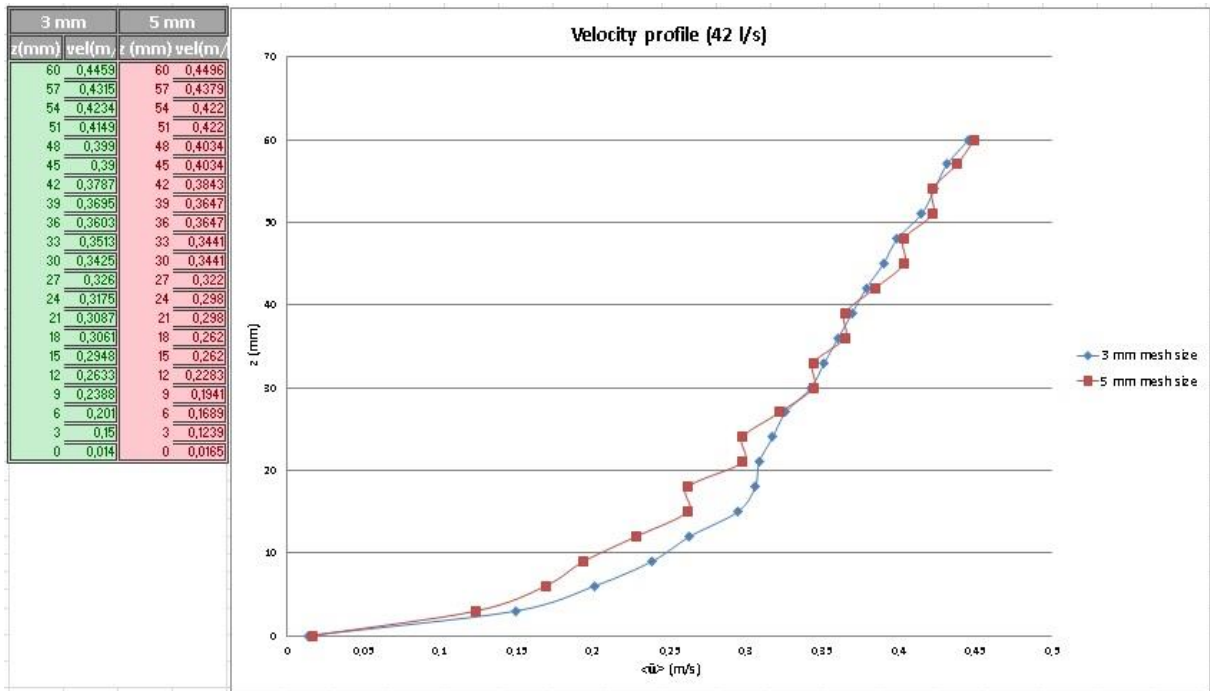


Figure 50: Mesh comparison for 42 l/s

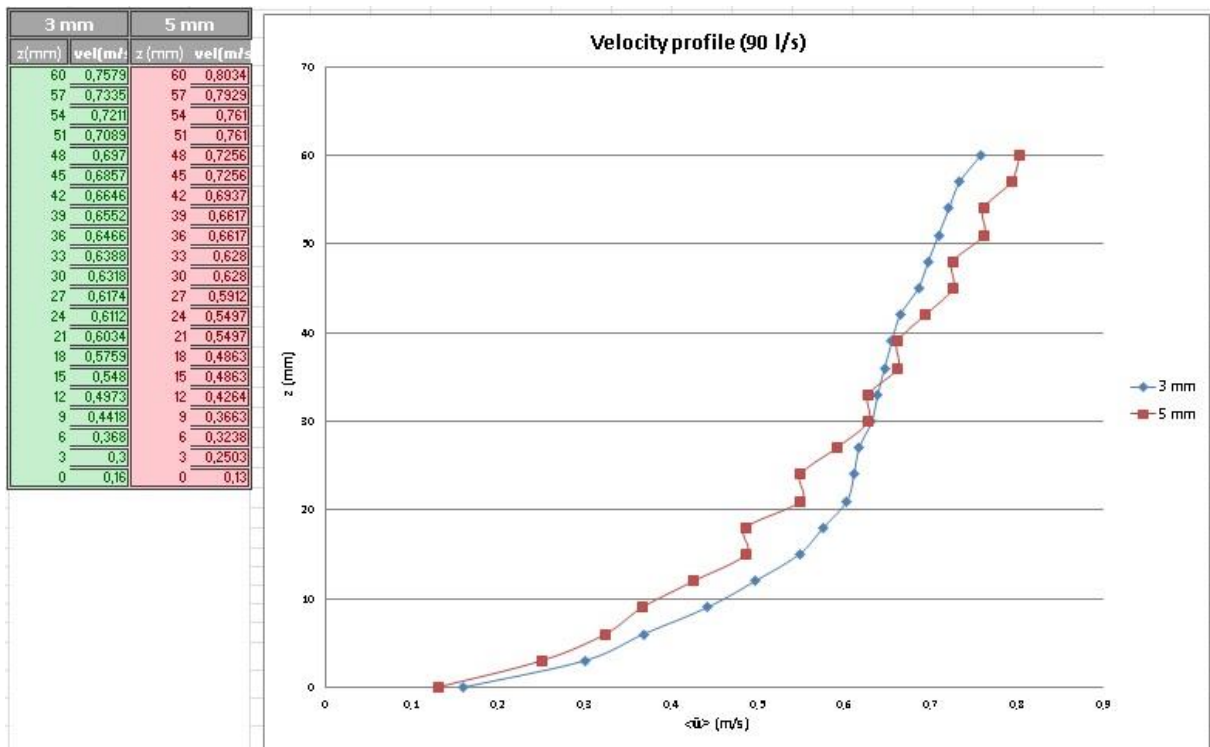


Figure 51: Mesh comparison for 90 l/s

Looking at the figures above, it's easy to understand why the 3 mm mesh size is the best solution in spite the two curves are quite close. The coarse mesh presents a particular trend because of the size itself: considering a cell of 5 mm, each 3 mm there are two same values since they are taken in the same cell. Further, the 3 mm mesh size is much closer to a realistic velocity profile for free surface flow.

6.8 Turbulent models in comparison

Two different turbulent models were used for 21 l/s water discharge and 151 water depth. As said in section 5.3, besides RANS equation and k-ε turbulence model, the Spalart-Allmaras turbulence model was chosen mainly to understand which one could be more appropriate for this particular study. So, in order to evaluate the accuracy of these two models, a velocity matching profile between STAR-CCM+ model and experimental data by Spiller et al. (2013) is offered in the following pictures for 21 l/s water discharge.

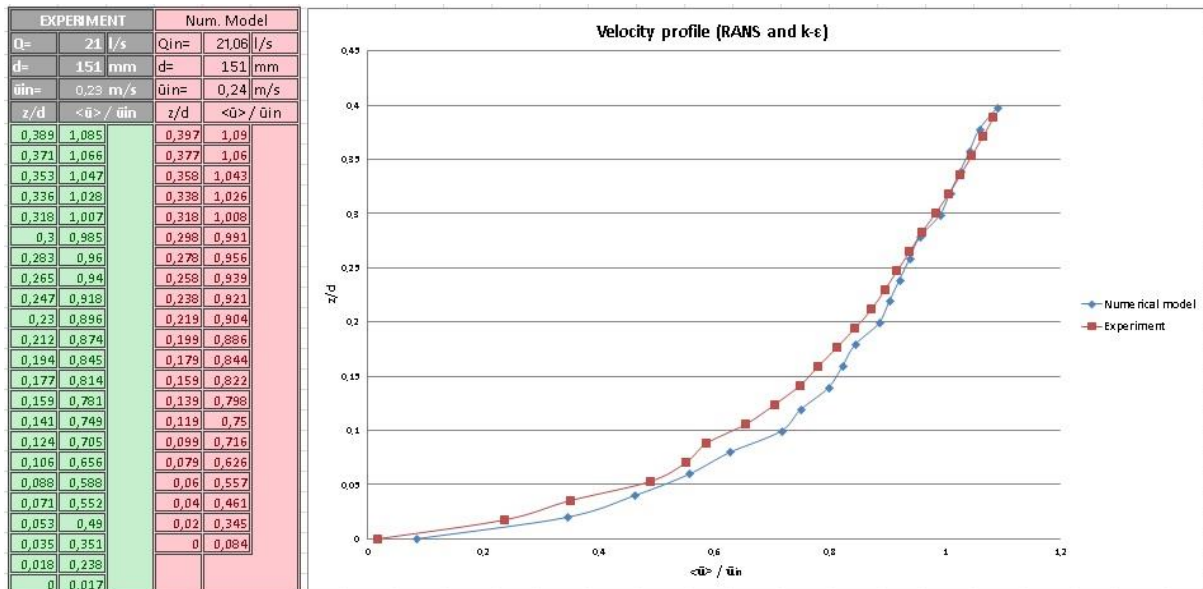


Figure 52: k-ε model (21 Vs)

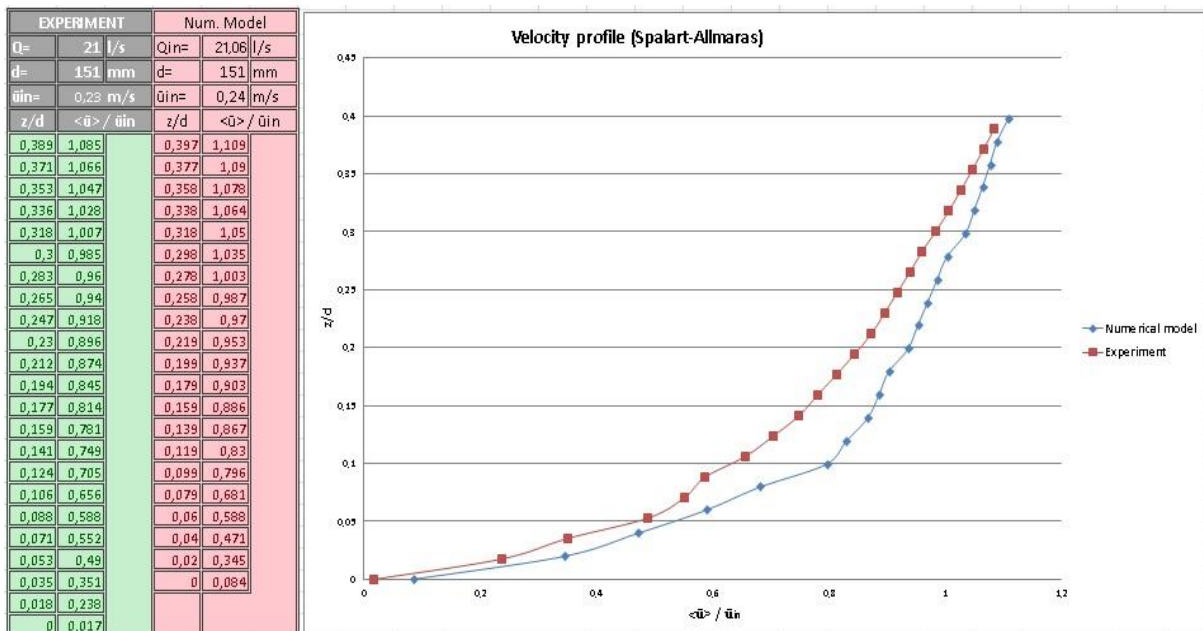


Figure 53: Spalart-Allmaras model (21 Vs)

The results are shown in non-dimensional plot: the ratio between double averaged velocity and inlet velocity on x-axis while the ratio between z-position (until 60 mm) and water depth on y-axis. Looking at the results, the first model is very accurate above 0.15, below, quite close, as it was expected; the second model instead, seems to be not able to properly match the experimental data in the area of analysis.

6.9 Experimental data comparison

In this paragraph all the results in terms of velocity profile are presented for the discharges simulated. In order to evaluate the accuracy of the model, a matching plot with experimental data, dimensional and non-dimensional, is realized for each discharge. The experimental data come from the plot presented in Table 1 of section 4.3.1.

6.9.1 6 l/s water discharge

In Figure 54 first discharge simulated, 6 l/s water discharge and 134 mm water depth, in dimensional plot, Figure 55 shows non-dimensional velocity profile considering inlet velocity and water depth.

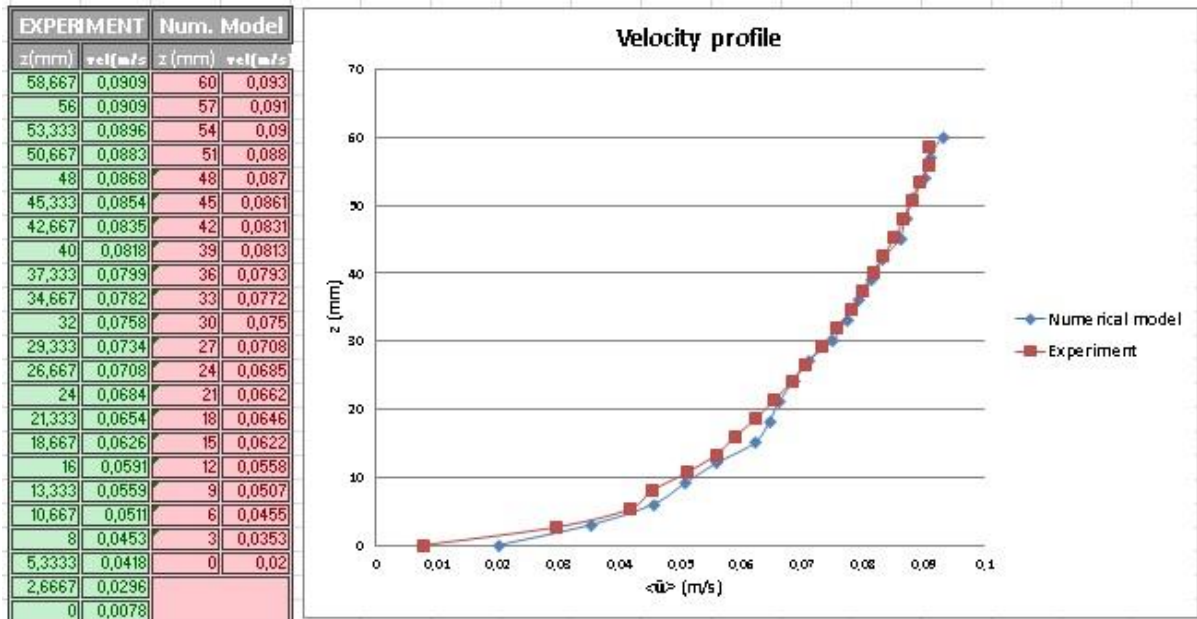


Figure 54: Dimensional velocity profile for 6 l/s

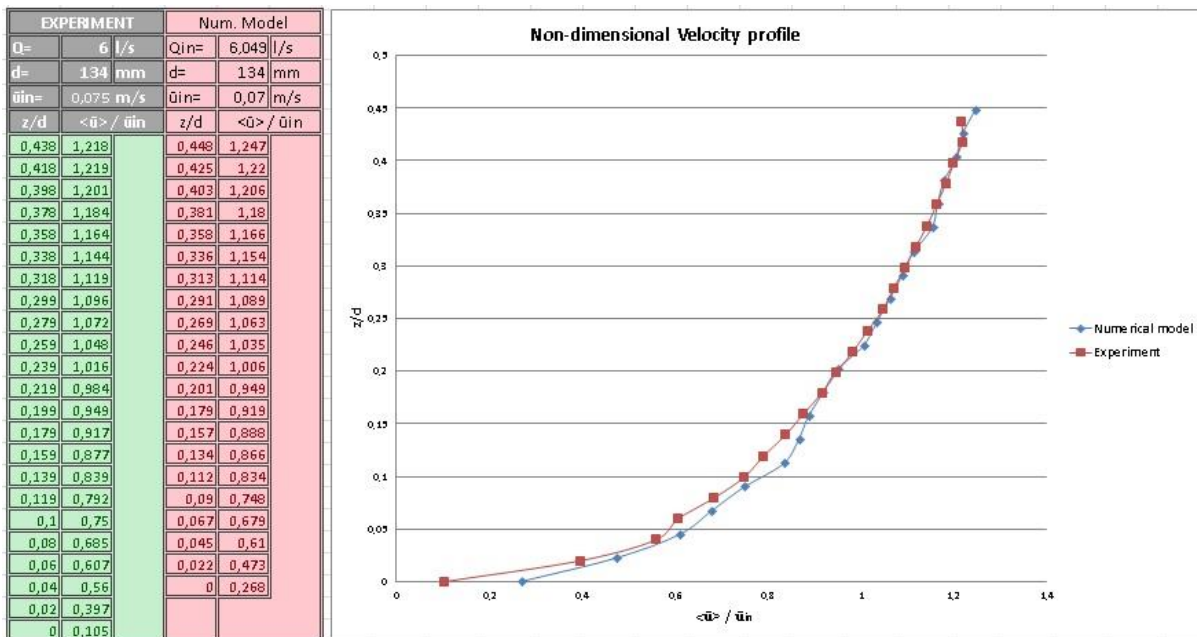


Figure 55: Non-dimensional velocity profile for 6 l/s

Focusing on matching, a particular characteristic comes out here, as well as in other discharges: a perfect matching above 20 mm, more or less for all the simulations, and some velocity differences below. As it was expected, the model loses some details in relation to

mesh size. In this study, choosing 3 mm base size, the model lost the perfect roundness of those elements on the bottom. Bigger is the base size, smoother is the bottom. The effects are clearly visible until the roughness tops elevation.

6.9.2 21 l/s water discharge

Non-dimensional velocity profile for 21 l/s water discharge is already shown in paragraph 6.8 presenting the differences between the two turbulent models used. In Figure 56 velocity matching in dimensional plot.

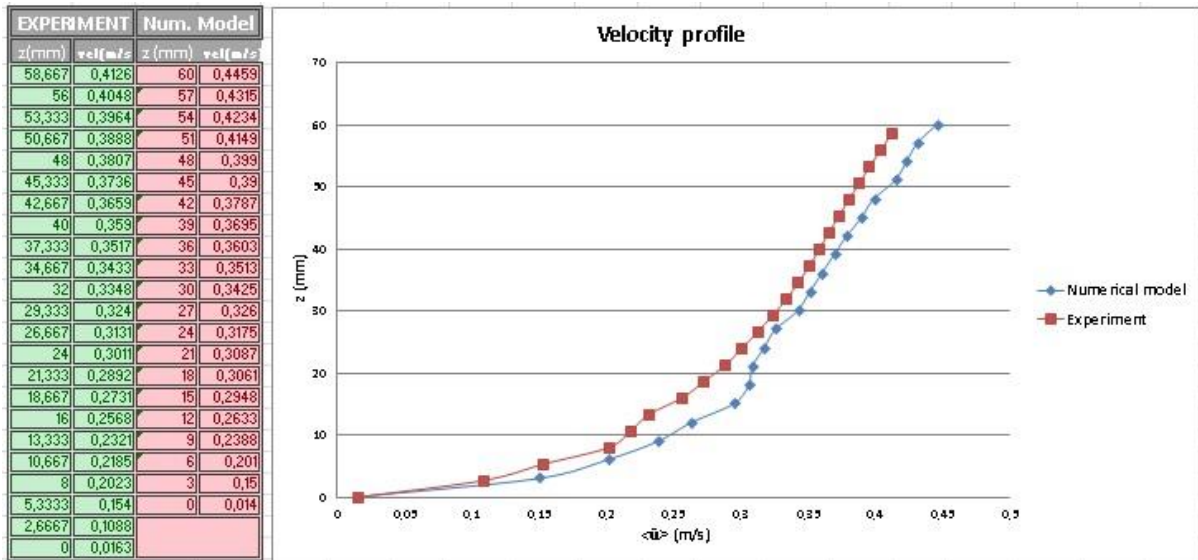


Figure 56: Dimensional velocity profile for 21 l/s

6.9.3 42 l/s water discharge

So that, third simulation was set at 42 l/s water discharge and 171 mm water depth: dimensional and non-dimensional plot in the following images.

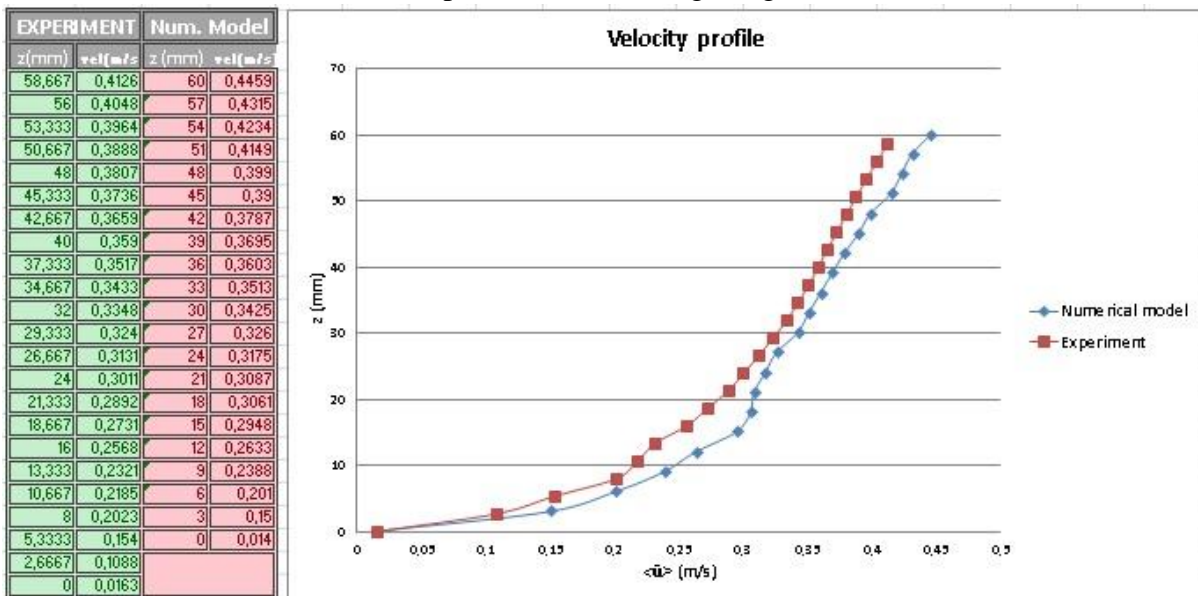


Figure 57: Dimensional velocity profile for 42 l/s

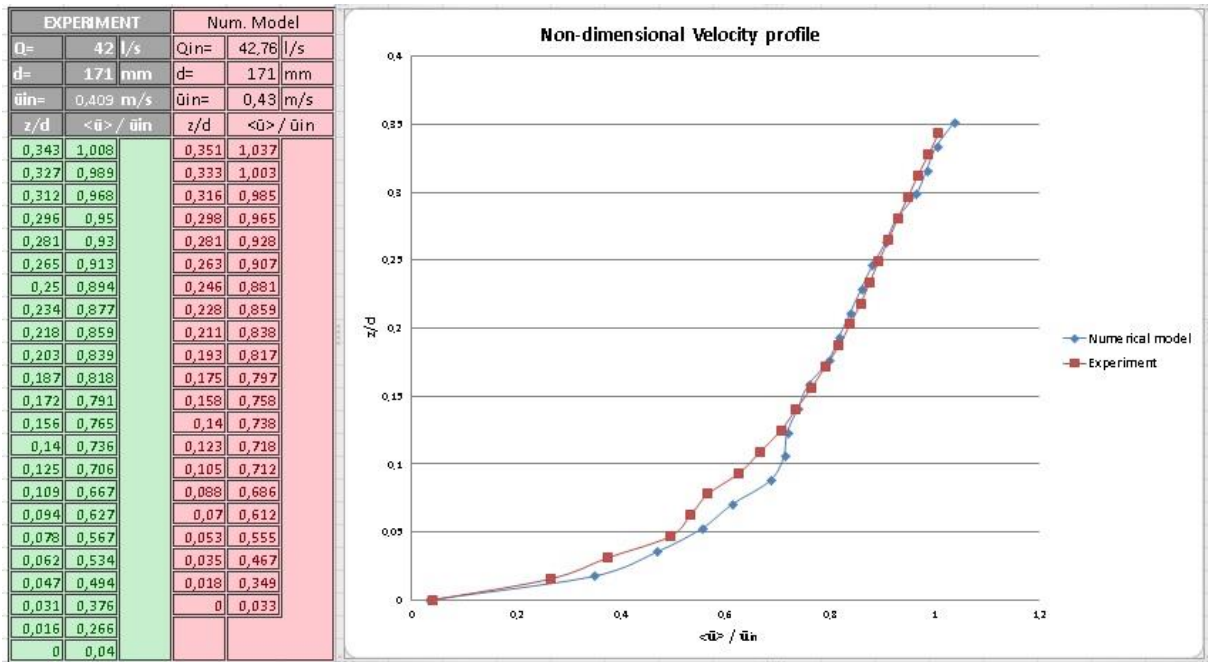


Figure 58: Non-dimensional velocity profile for 42 l/s

Same considerations for this discharge as well as for 21 l/s: perfect matching above 20 mm, some velocity deviations below.

6.9.4 63 l/s water discharge

Fourth simulation was set at 63 l/s water discharge and 191 mm water depth; dimensional and non-dimensional velocity profile in the following images.

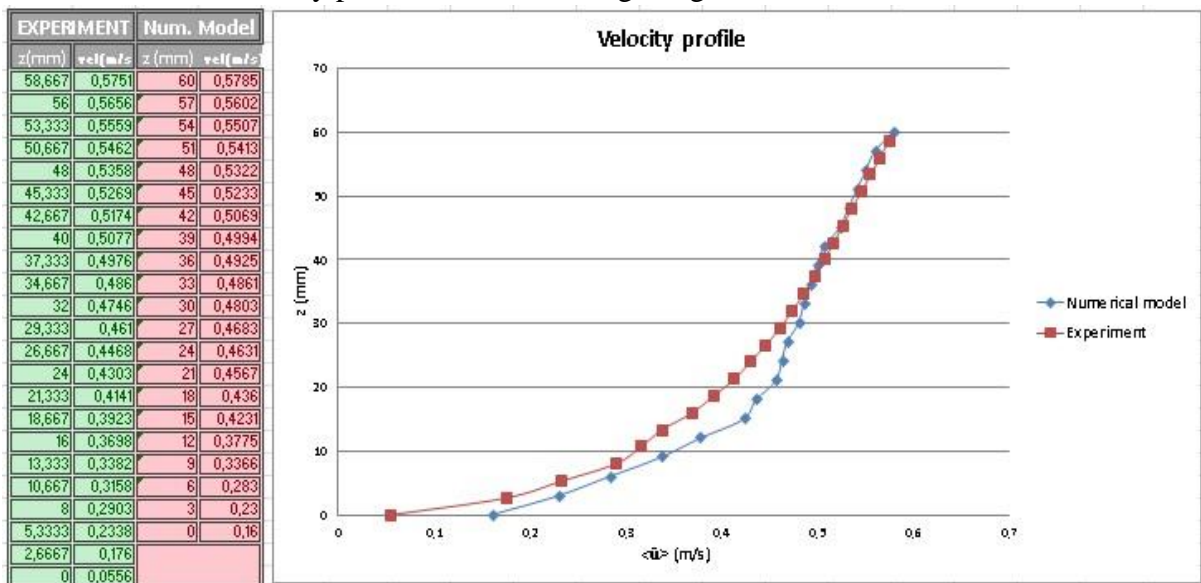


Figure 59: Dimensional velocity profile for 63 l/s

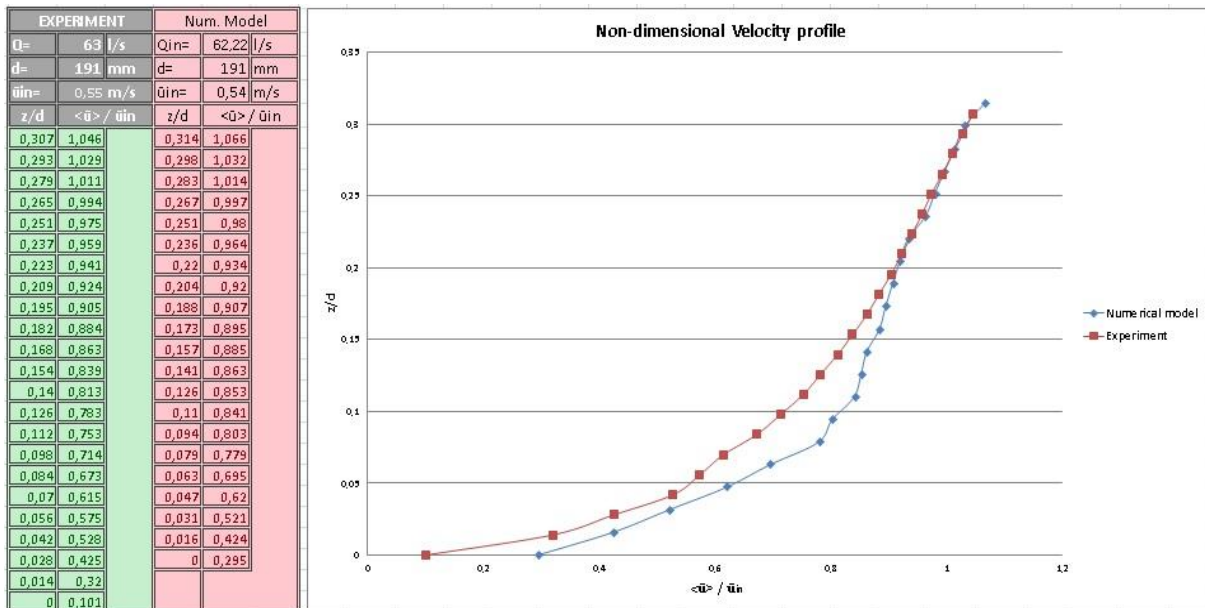


Figure 60: Non-dimensional velocity profile for 63 l/s

Looking at the pictures above, besides the usual characteristics typical of all simulations, another feature comes out here: increasing the water discharge, so the velocity, the deviation between simulation results and experimental data, below 20/25 mm, becomes more relevant. It's already possible to say that increasing the velocity as well as the turbulence characteristics, or in other words, the Reynolds number, the model starts to fail in accuracy.

6.9.5 90 l/s water discharge

Last simulation was set at 90 l/s water discharge and 207 mm water depth. It represents the highest value in term of discharge and so of velocity, considered in this study and in the experiment by Spiller et al. (2013) as well. Velocity matching in dimensional and non-dimensional plot is presented in the following pictures.

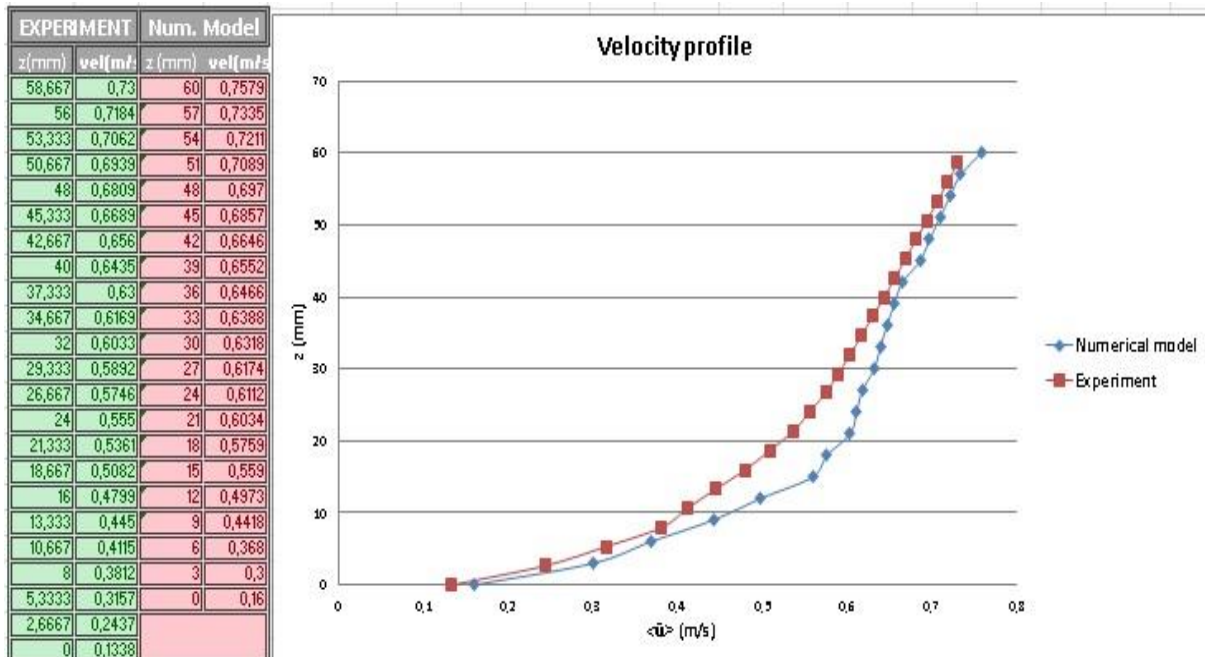


Figure 61: Dimensional velocity profile for 90 l/s

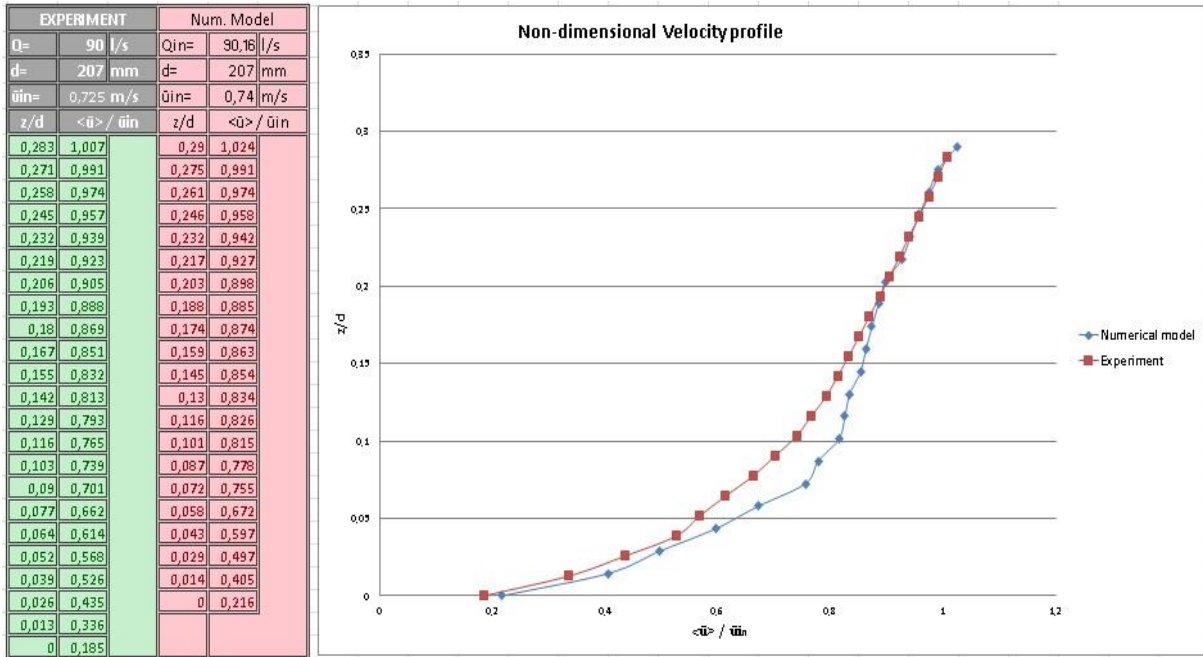


Figure 62: Non-dimensional velocity profile for 90 l/s

As already said for the previous case, increasing the velocity, the deviation below 20 mm or more becomes important. Focusing on dimensional velocity profile related to 63 l/s and 90 l/s water discharge, passing from 63 l/s to 90 l/s, the model lost in accuracy between 30-40 mm in z-direction.

7 DISCUSSION

The results achieved during this study underlines that STAR-CCM+ model is able to predict the characteristics of a free surface flow for different hydraulic conditions. Inlet values of turbulence chosen, size and quality of the computational grid are the main factors, besides turbulence model, that can affect the accuracy of the simulations.

Once the turbulence is high (e.g. $Re \approx 120.000$), the model loses in terms of accuracy as clearly seen for 63 l/s and 90 l/s water discharges relating to pressure and velocity. In this study, choosing 3 mm base size, the gravel bed loses the perfect roundness of those elements: bigger is the base size, smoother is the bottom. The effects are clearly visible until the roughness tops elevation, so that, 3 mm cell size has been the best solution, considering the total number of cells or rather the weight of the simulation.

Anyway, the velocity matching with the experimental data has been definitely satisfied and this can open a new way for further researches. As a recommendation for future works, one is to choose the simplest model which gives acceptable engineering results for the application analyzed; typically, it's always suggested to start with the k- ϵ turbulence model. In general, if wall effects are important, the hybrid wall functions could be the solution, or a low Reynolds number turbulence model, making sure to have a fine mesh resolution in the wall region. Differently, if anisotropic effects are important, then could be better to use the Reynolds Stress Models. However these assumptions, coming from theory, need to be supported by further analysis.

In summary, numerical methods seem to be most suitable ways of analyzing fluid mechanic problems which give important insights to model turbulent flow.

8 CONCLUSION

The objective of this thesis has been to look into the possibility to use the commercial CFD code STAR-CCM+ to simulate the flow over an artificial gravel bed. The data taken to compare the results with are from a physical model test conducted by Spiller et al. (2013). PIV measurements were taken in a laboratory flume. This flume has been modeled within STAR-CCM+ in order to see whether it can reproduce the general flow characteristics.

An optimized grid generation method for free surface grids, using the VOF method in STAR-CCM+ was developed during this process. A physical model setup was developed based on theory on 3D CFD modeling. Initial conditions and boundary conditions were set up based on theory and experimentation. The results from the simulation showed that, as already discussed, the model is able to predict, with high accuracy, the characteristic of a free surface flow for 6, 21, 42 l/s water discharges.

In conclusion, CFD is a very powerful tool, whose capabilities are conditioned to our understanding of phenomena and to computer power. The smaller is the degree of empiricism we wish to introduce in the models, the greatest is the computer power needed. It is a very fascinating world in which smart ideas are needed to discover newer and newer possibilities.

9 BIBLIOGRAPHY

CD-Adapco. (2011). User Guide, *Star-CCM+*. CD-Adapco

Pedersen, (2012). *3D Numerical Modelling of Hydropeaking Scenarios in Norwegian Regulated Rivers*. Norwegian University of Science and Technology.

Cucco, (2011). *Analisi numeriche del flusso intorno a microgeneratori eolici ad asse vertical nell'infrastruttura di Supercomputing S.C.o.P.E.* Università degli Studi di Napoli Federico II.

Hickin. *River Hydraulics and Channel Flow*.

Nikora, (2007). *Double-Averaging Concept for Rough-Bed Open-Channel and Overland Flows: Theoretical Background*. University of Aberdeen.

Cushman-Roisin, Gualtieri & Mihailovic. *Environmental Fluid Mechanics: Current issues and future outlook*.